

الجمهورية الجزائرية الديمقراطية الشعبية

People's Democratic Republic of Algeria

وزارة التعليم العالي والبحث العلمي

Ministry of Higher Education and Scientific Research

University MUSTAPHA Stambouli

mascara



جامعة مصطفى أسطوبولي

معسكر

Faculty of Exact Science

Department of Physics

Third Cycle Doctoral Thesis

Specialty: Physics

Option: Materials for renewable energy

Structure Stability and Optical Response of Complex Lead Perovskite: A Computational Approach to Modeling of Perovskite Solar Cells

Presented by: Merah Somia

On: 29 / 05 / 2025

In front of the jury:

<i>President</i>	<i>Mr.Y. Mouchaal</i>	<i>Prof</i>	<i>University of Mascara</i>
<i>Reviewer</i>	<i>Mrs.A. Bekhti Siad</i>	<i>Prof</i>	<i>University of Mascara</i>
<i>Reviewer</i>	<i>Mrs.F.Boukabrine</i>	<i>Prof</i>	<i>University of Sidi Bel-Abbés</i>
<i>Reviewer</i>	<i>Mrs.S.Bahlouli</i>	<i>Prof</i>	<i>University of Oran</i>
<i>Supervisor</i>	<i>Mr. O.Sahnoun</i>	<i>MCA</i>	<i>University of Mascara</i>
<i>Co-Supervisor</i>	<i>Mrs. H.Riane</i>	<i>Prof</i>	<i>University of Mascara</i>

Année Universitaire: 2024-2025

بِسْمِ اللَّهِ الرَّحْمَنِ الرَّحِيمِ

Acknowledgments

First, I thank the Lord Almighty for giving me the courage, will and patience to complete this work.

*I would like to express my sincere gratitude to **Mr. SAHNOUN Omar**, MCA at University of Mascara, for leading my researches and for the faith; he has shown in me throughout the years of my doctoral studies and for all his advices and constructive remarks. His impact has been very fruitful both on a human and scientific level. Words won't express the room he has taken in my heart so a massive thanks for him.*

*I also address my warm thanks to my co-director of thesis **Mrs. RIANE Houaria**, Professor at university of Mascara, for her constant attention to my research work, for her judicious councils and her listening which were prevailing for the good success of this work.*

*I would like to express my warmest thanks to **Mr. MOUCHAAL Younes**, Professor at the University of Mascara, for the honour he has bestowed on me by chairing the jury of this thesis.*

*I would like to express my gratitude to **Mrs. BEKHTI SIAD Amaria**, Professor at the University of Mascara, **Mrs.F.Boukabrine**, Professor at the University of Sidi Bel-Abbés , **Mrs. BAHLOULI Samia** , Professor at the University des Sciences et de la Technologie d'Oran Mohamed Boudiaf, for their approval of my work and for their honorable membership of my thesis jury.*

*I thank **Mr. YAHIAOUI Ihab**, MCA at Ecole Normal supérieure D'oran AMMOUR AHMED for to assist in calculating the Spectroscopic Limited Maximum Efficiency (SLME).*

*I thank **Mr. SAHNOUN Mohamed**, Professor at University of Mascara and director of the laboratory LPQ3M of the University of Mascara for welcoming me in his laboratory*

*I would like to sincerely thank my colleague Mr. **MOUCHER Ryad** for his valuable assistance in my research, as well as for all his advice and constructive feedback.*

*I would also like to thank **Mr. SEDDIK Taieb** Professor at the University of Mascara, for his attentiveness, expertise, constructive criticism, and valuable advice.*

*In addition, special thanks to **B. Rezzini** and **El Goutni Mohamed El Amine** for their daily support and help.*

In the hope that no one will be forgotten, I would like to thank all those who have contributed in any way to the realization of this thesis.

Dedication

This work is lovingly dedicated to

My dear parents, whose unwavering love, sacrifices, and constant encouragement have shaped who I am and given me the strength to pursue this journey;

My grandparents, whose wisdom, prayers, and values have always guided me;

My sister for her support, laughter, and belief in me, even when I doubted myself

To my brothers and family who stood by me with encouragement during the most challenging moments.

My friend, whose presence, motivation, and understanding helped carry me through difficult moments

To all of you—thank you for being my foundation, my inspiration, and my greatest source of strength.

 *Merah Somia* 

TABLE OF CONTENTS

Thanks	I
LIST OF FIGURE.....	IX
LIST OF Tables.....	VIII
Summary.....	XI
General Introduction	1

Index

Chapter I: perovskite for Solar Cells

I.1 Introduction.....	6
I.2 THE SOLAR CELLS	6
I.2.1 History	6
I.2.2 Principles of solar cell operation	7
I.2.2.1 A solar cell's characteristics	10
I.2.2.2 State-of-the art solar cells	13
I.2.3 Advantages and disadvantages of solar energy	17
I.2.3.1. Advantages	17
I.2.3.2. Disadvantages	17
I.3 The perovskite materials	18

I.3.1 Description and definition of perovskite	18
I.3.2 History of perovskites	19
I.3.3 The crystalline arrangement of perovskite materials	20
I.3.3.1 Type of perovskite structure	21
I.3.3.1.a Simple perovskite structures.....	21
I.3.3.1.b The complex perovskite structures.....	22
I.3.4 The different families of perovskite.....	22
I.3.4.1 The perovskite oxides ABO_3	22
I.3.4.2 Halogen perovskites.....	22
I.3.5 Transition from single to double perovskites	22
I.3.5.1 Simple perovskite materials containing halogens.....	22
I.3.5.2 Doubles Pérovskites.....	23
I.3.6 Criteria for the stability of the perovskite structure.....	24
I.3.6.1 Goldschmidt tolerance factor (t).....	24
I.3.6.2 Departure from ideality.....	25
I.3.6.3 The ionicity of anion-cation bonds.....	26
I.3.7 The applications of perovskites	26

Chapter II: Computational Methods

II.1 Introduction.....	33
II.2 Schrödinger's equation.....	33
II.3 Fundamental approximations	35
II.3.1 The Born-Oppenheimer approximation.....	35
II.3.2 Hartree-Fock approximation	36
II.4 Density functional theory (DFT).....	37
II.4.1 Thomas and Fermi's approach.....	37
II.4.2 Theorems of Hohenberg and Kohn	38
II.4.2.2 Second Hohenberg-Kohn theorem: variational principle.....	39
II.4.3 The Kohn and Sham equations	40
II.5 Resolution of exchange and correlation energy	41
II.5.1 The local density approximation (LDA).....	41
II.5.2 LDA+U approximation	42
II.5.3 Generalized Gradient Approximation (GGA).....	43
II.5.4 The EV-GGA approximation.....	43
II.5.5 Modified Becke and Johnson potential (mBJ).....	43
II.5.6 Hybrid functions.....	45
II.6 The linearized augmented plane wave method (FP-LAPW)	45

II.6.1 The APW method	45
II.6.2 Principle of the FP-LAPW method.....	47
II.6.3 The role of linearization energies E_l	48
II.6.4 Local orbital development	48
II.6.5 The APW + lo method.....	49
II.6.6 The LAPW+LO method	50
II.6.7 The WIEN2k code	50
II.7 Spectroscopic Limited Maximum Efficiency Model (SLME).....	53
II.8 BoltzTrap.....	54
II.9 VASP code	55
II.15.Conclusion.....	56

***Chapter III: Investigation of the structural and and
Optoelectronic Conversion Efficiency of
 $Rb_2AgSb(Cl_{1-x}Br_x)_6$ alloys***

III.1 Introduction.....	61
III.2 Calcul details	61
III.3 Structural properties.....	62
III.4 Electronic properties	65
III.4.1 Band structures	65

III.4.2 Density of states	68
III.4.3 Carrier effective mass and mobility.....	70
III.5 Optical properties	71
III.5.1 Dielectric function	71
III.5.2 Refractive index	74
III.5.3 Optical reflectivity	76
III.5.4 Absorption	76
III.6 Impact of Thickness and Temperature on Optoelectronic Performance (SLME).....	78
III.7 Thermoelectric characteristics of Rb ₂ AgSb(Cl _{1-x} Br _x) ₆ alloys.....	79
III.7.1 Introduction.....	79
III.7.2 Thermoelectric effects.....	80
III.7.2.1 Seebeck effect	80
III.7.2.2 Peltier effect	81
IV.7.2.3 Thomson effect	82
III.8 Thermoelectric energy conversion.....	82
III.8.1 Power generation	82
III.8.2 Cooling	84
III.9 Thermoelectric properties	85
III.9.1 Calcul details	85
III.9.2 Seebeck coefficient	85
III.9.3 Relaxation time.....	86
III.9.4 Electrical conductivity and electronic thermal conductivity	87

III.9.5 Optimization of merit factor ZT	89
---	----

III.10 Conclusion.....	91
------------------------	----

***ChapterIV: Theoretical Study of a new Double
Perovskite Alloys $Rb_2AgSb_{1-x}Bi_xX'$ ($X' = Cl, Br, I$)
Using VASP Analysis***

IV.1 Introduction	96
IV.2 calculation method.....	96
IV.3 RESULTS AND DISCUSSION.....	97
IV.3.1 Electronic properties.....	97
IV.3.1.a Band structures.....	93
IV.3.1.b Density of states.....	101
VI.3.2 Mechanical properties.....	107
VI.3.2.1 Elastic coefficients.....	107
General conclusion	111
Anex.....	113

LIST OF FIGURES

Figure	TITLE	PAGE
Figure I-1	Diagramme d'une jonction p-n dans des conditions d'équilibre (a) et d'illumination (b)	8
Figure I-2	the solid black line, representing the emission from an ideal black body, depicts the solar spectrum	9
Figure I.3	A schematic diagram shows a J-V curve in darkness (black dashed line) and under illumination (red solid line)	11
Figure I.4	Shockley-Queisser efficiency limit as a function of the gap considering solar radiation (AM 1,5 G)	12
Figure I.5	Record efficiencies of solar cells and photovoltaic modules from 1976 to 2022, classified by technology	14
Figure I.6	Classification of the main solar cell technologies: crystalline silicon, thin film, organic, and hybrid	15
Figure I.7	Perovskites in nature	18
Figure I.8	The ideal structure for ABX ₃ perovskite	21
Figure I.9	Three-dimensional arrangement of BO ₆ octahedra in the perovskite structure	21
Figure I.10	Structures of different perovskites: (a) ideal perovskite ABO ₃ and (b) double perovskite A ₂ BB'O ₆ .	23
Figure II.1	Transition from a problem with n electrons and N nuclei to one with n electrons.	36
Figure II.2	Illustration of the first Hohenberg-Kohn theorem	38
Figure II.3	Illustration of the second Hohenberg-Kohn theorem	40
Figure II.4	Muffin-Tin" potential	46
Figure II.5	Multiple energy windows.	49
Figure II.6	The structure of the WIEN2k program.	52
Figure III.1	Crystal structure visualization of (a) Rb ₂ AgSbCl ₆ , (b) Rb ₂ AgSb(Cl _{0.75} Br _{0.25}) ₆ alloy, (c) Rb ₂ AgSb(Cl _{0.5} Br _{0.5}) ₆ and (d) Rb ₂ AgSb(Cl _{0.25} Br _{0.75}) ₆ .	62
Figure III.2	variation of the total energy as a function of the volume of the Rb ₂ AgSb(Cl _{1-x} Br _x) ₆ alloys	64
Figure III.3	The computed Rb ₂ AgSb(Cl _{1-x} Br _x) ₆ alloy band structure.	67
Figure III.4	Total and partial density of states (DOS) of Rb ₂ AgSb(Cl _{1-x} Br _x) ₆ alloys	70
Figure III.5	The complex dielectric function's real (ϵ_1) imaginary (ϵ_2) and component spectra for Rb ₂ AgSb(Cl _{1-x} Br _x) ₆ materials.	74
Figure III.6	The calculated refractive index n (ω), extinction coefficient k (ω) for Rb ₂ AgSb(Cl _{1-x} Br _x) ₆ alloys.	76

Figure III.7	The calculated reflectivity coefficient $R(\omega)$ of $\text{Rb}_2\text{AgSb}(\text{Cl}_{1-x}\text{Br}_x)_6$ alloys	77
Figure III.8	The calculated absorption coefficient $\alpha(\omega)$ of $\text{Rb}_2\text{AgSb}(\text{Cl}_{1-x}\text{Br}_x)_6$ alloys	78
Figure III.9	Optical band gap of $\text{Rb}_2\text{AgSb}(\text{Cl}_{1-x}\text{Br}_x)_6$ alloys	78
Figure III.10	The SLME for $\text{Rb}_2\text{AgSb}(\text{Cl}_{1-x}\text{Br}_x)_6$ alloys as a function of temperature and film thickness.	79
Figure III.11	Schematic diagram of the Seebeck effect	81
Figure III.12	Diagram explaining the Peltier effect	81
Figure III.13	Schematic diagram of the Thomson effect	82
Figure III.14	Schematic diagram of a thermoelectric branch (a), thermocouple (b) and a thermoelectric module (c)	83
Figure III.15	Cooling applications based on thermoelectric modules	84
Figure III.16	Seebeck coefficient of $\text{Rb}_2\text{AgSb}(\text{Cl}_{1-x}\text{Br}_x)_6$ alloys as a function of temperature.	86
Figure III.17	The relaxation time calculated for $\text{Rb}_2\text{AgSb}(\text{Cl}_{1-x}\text{Br}_x)_6$ alloys	87
Figure III.18	Electrical conductivity as a function of temperature for $\text{Rb}_2\text{AgSb}(\text{Cl}_{1-x}\text{Br}_x)_6$ alloys.	88
Figure III.19	Electronic thermal conductivity as a function of temperature for $\text{Rb}_2\text{AgSb}(\text{Cl}_{1-x}\text{Br}_x)_6$ alloys	88
Figure III.20	Variation of power factor as a function of temperature for $\text{Rb}_2\text{AgSb}(\text{Cl}_{1-x}\text{Br}_x)_6$ alloys.	89
Figure III.21	Variation of ZT merit factor with temperature for $\text{Rb}_2\text{AgSb}(\text{Cl}_{1-x}\text{Br}_x)_6$ alloys.	90
Figure IV.1	The calculated band structure of $\text{Rb}_2\text{AgSb}_{1-x}\text{Bi}_x\text{X}'_6$ alloys.	98
Figure IV-2	Total and partial density of states (DOS) of $\text{Rb}_2\text{AgSb}_{1-x}\text{Bi}_x(\text{X}')_6$ alloys	102

LIST OF Tables

Table	TITLE	PAGE
<i>Table I.1</i>	Computational performance in the LDA approximation	42
<i>Table III.1</i>	Calculated lattice constant (a_0), volume (V), bulk modulus (B), derivative of bulk modulus (B') and formation energy (E_f) of $Rb_2AgSb(Cl_{1-x}Br_x)_6$ alloys.	65
<i>Table III.2</i>	Calculated indirect bandgap using GGA and mBJ potential for $Rb_2AgSb(Cl_{1-x}Br_x)_6$ alloys	66
<i>Table III.3</i>	the Calculated Hole and electron effective masses m_h^* , m_e^* , deformation potential constants E_{CBM} (eV) and E_{VBM} (eV), carrier mobility μ ($cm^2 V^{-1} s^{-1}$) for $Rb_2AgSb(Cl_{1-x}Br_x)_6$ alloys	71
<i>Table III.4</i>	Calculated direct bandgap and optical parameters for $Rb_2AgSb(Cl_{1-x}Br_x)_6$ alloys.	75
<i>Table III.5</i>	Calculated spectroscopic limited maximum efficiencies for $Rb_2AgSb(Cl_{1-x}Br_x)_6$ alloys	78
<i>Table IV.1</i>	Calculated indirect bandgap using HSE (Ev) for $Rb_2AgSb_{1-x}Bi_xX'_6$ alloys	94
<i>Table IV.2</i>	The calculated compressibility modulus (B) and elastic constants (C_{ij}) in GPa, along with the lattice parameter (a_0) in Å, Young's modulus (E) in GPa, shear modulus (G) in GPa, Poisson's ratio (ν), and the B/G ratio.	105

Résumé

Ce travail présente une contribution à l'étude de l'effet de la substitution du bromure sur les propriétés structurales, électroniques et optiques des matériaux de type pérovskite $\text{Rb}_2\text{AgSbCl}_6$.

Pour déterminer ces différentes propriétés, nous avons effectué des simulations en appliquant la méthode linearized augmented plan wave (FP-APW), qui est basée sur la théorie de la fonction de la densité (DFT), en utilisant l'approximation du gradient généralisé (WC-GGA) pour traiter le terme d'échange et de corrélation, où le package de cette méthode est implémenté dans le code WIEN2K.

L'énergie de la bande interdite calculée pour $\text{Rb}_2\text{AgSbCl}_6$ dans son état pur est d'environ 2,08 eV en utilisant le potentiel d'échange Tran-Blaha (TB) – Becke Johnson (mBJ) modifié, ce qui est en bon accord avec les mesures es. On a remarqué que ces valeurs de bande interdite diminuent lorsque Br est substitué dans le site Cl, respectivement pour des concentrations de 25 %, 50 % et 75 %. En outre, l'énergie du gap pour les matériaux $\text{Rb}_2\text{AgSbBr}_6$ a également été calculée et la valeur trouvée est à 1,34 eV. Cette étude montre que la substitution de Br augmente la mobilité des trous et des porteurs d'électrons des composés $\text{Rb}_2\text{AgSbCl}_6$ purs. De plus, l'analyse optique révèle que la substitution de Br améliore les propriétés optiques de $\text{Rb}_2\text{AgSbCl}_6$ en réduisant la transparence et en améliorant l'indice de réfraction et l'absorption dans la région de la lumière visible. En analysant le Spectroscopique Limited Maximum Efficience (SLME). L'électron minoritaire luminescent spécifique (SLME) de $\text{Rb}_2\text{AgSb}(\text{Cl}_{0.5}\text{Br}_{0.5})_6$ est de 9,51 %. Bien que ce pourcentage soit modeste, il peut être attribué à la bande interdite indirecte du matériau. Nous avons aussi calculé Les propriétés thermoélectriques Les propriétés électroniques révèlent que ces composés sont des semi-conducteurs de type p.

Sur la base des résultats obtenus, il est prévu que la bande interdite et les propriétés optiques et thermoélectriques de la pérovskite $\text{Rb}_2\text{gSbCl}_6$ peuvent être efficacement ajustées par la substitution de Br sur les sites Cl, ce qui fait des alliages $\text{Rb}_2\text{AgSb}(\text{Cl}_{1-x}\text{Br}_x)_6$ des candidats prometteurs pour des applications optoélectroniques et photovoltaïques. Nous étudions également les propriétés électroniques des alliages $\text{Rb}_2\text{AgSb}_{1-x}\text{Bi}_x\text{X}'_6$, où x prend des valeurs de zéro, 0,25, 0,50, 0,75, et 1, avec X' représentant Cl, Br, ou I.

Mots-clés : Propriétés électroniques ; propriétés optiques ; applications photovoltaïques ; approches de premiers principes ; Wien2k. Vasp

Summary

This work presents a contribution to the study of the effect of bromide substitution on the structural, electronic, and optical properties of $\text{Rb}_2\text{AgSbCl}_6$ perovskite materials.

To determine these different properties, we conducted simulations using the linearized augmented plane wave (FP-APW) method, which is based on density functional theory (DFT), employing the generalized gradient approximation (WC-GGA) to handle the exchange and correlation terms. The implementation of this method is carried out using the WIEN2K code.

The calculated band gap energy for pure $\text{Rb}_2\text{AgSbCl}_6$ is approximately 2.08 eV, obtained using the modified Tran-Blaha (TB)–Becke Johnson (mBJ) exchange potential, which is in good agreement with experimental measurements. It was observed that the band gap values decrease as Br substitutes Cl at different concentrations of 25%, 50%, and 75%. Additionally, the band gap energy for $\text{Rb}_2\text{AgSbBr}_6$ was calculated, yielding a value of 1.34 eV. This study demonstrates that Br substitution enhances the hole and electron carrier mobility in pure $\text{Rb}_2\text{AgSbCl}_6$ compounds. Furthermore, optical analysis reveals that Br substitution improves the optical properties of $\text{Rb}_2\text{AgSbCl}_6$ by reducing transparency while enhancing the refractive index and absorption in the visible light region. By analyzing the Spectroscopically Limited Maximum Efficiency (SLME), the specific luminescent minority electron (SLME) of $\text{Rb}_2\text{AgSb}(\text{Cl}_{0.5}\text{Br}_{0.5})_6$ was found to be 9.51%. Although this percentage is modest, it can be attributed to the indirect band gap nature of the material. Additionally, we calculated the thermoelectric properties, and the electronic properties indicate that these compounds are p-type semiconductors.

Based on the obtained results, it is expected that the band gap, optical, and thermoelectric properties of $\text{Rb}_2\text{AgSbCl}_6$ perovskite can be effectively tuned by Br substitution at Cl sites, making $\text{Rb}_2\text{AgSb}(\text{Cl}_{1-x}\text{Br}_x)_6$ alloys promising candidates for optoelectronic and photovoltaic applications. Also we study the electronic properties of $\text{Rb}_2\text{AgSb}_{1-x}\text{Bi}_x\text{X}'_6$ alloys, where x takes values of zero, 0.25, 0.50, 0.75, and 1, with X' representing Cl, Br, or I.

Keywords: Electronic properties; Optical properties; Photovoltaic applications; First-principles approaches; Wien2k, thermoelectric properties, Vasp

ملخص

يقدم هذا العمل مساهمة في دراسة تأثير استبدال البروميد على الخصائص التركيبية والإلكترونية والبصرية لمواد البيروفسكايت من النوع $Rb_2AgSbCl_6$.

لتحديد هذه الخصائص المختلفة، قمنا بإجراء محاكاة باستخدام طريقة الموجة المستوية الخطية المعززة

(FP-APW) والتي تستند إلى نظرية الكثافة الوظيفي (DFT) باستخدام تقريب التدرج المعمم (WC-GGA) لمعالجة مصطلح التبادل والارتباط، حيث يتم تنفيذ حزمة هذه الطريقة في التعليمات البرمجية WIEN2K.

تبلغ طاقة فجوة النطاق المحسوبة لـ $Rb_2AgSbCl_6$ النقي حوالي 2.59eV باستخدام Tran-Blaha - تعديل Becke Johnson mBJ إمكانية التبادل وهو ما يتوافق جيداً مع القياسات التجريبية. لوحظ أن قيم فجوة الطاقة المحظورة تنخفض عند استبدال Br في موقع Cl بنسبة 25% و 50% و 75%. بالإضافة إلى ذلك، تم حساب فجوة الطاقة لمادة $Rb_2AgSbBr_6$ ، ووجد أن قيمتها 1.34 eV. توضح هذه الدراسة أن استبدال Br يزيد من حركة الثقوب وحاملي الإلكترونات في مركب $Rb_2AgSbCl_6$ النقي. علاوة على ذلك، يكشف التحليل البصري أن استبدال Br يحسن الخصائص البصرية لـ $Rb_2AgSbCl_6$ عن طريق تقليل الشفافية وزيادة معامل الانكسار والامتصاص في نطاق الضوء المرئي. من خلال تحليل الحد الأقصى لكفاءة الامتصاص الطيفي (SLME)، تبين أن SLME لمركب $Rb_2AgSb(Cl_{0.5}Br_{0.5})_6$ يبلغ 9.51%. وعلى الرغم من أن هذه النسبة متواضعة، إلا أنها تُعزى إلى فجوة الطاقة المحظورة غير المباشرة للمادة. بالإضافة إلى ذلك، تم حساب الخصائص الكهروحرارية، حيث كشفت الخصائص الإلكترونية أن هذه المركبات هي أشباه موصلات من النوع p.

بناءً على النتائج التي تم الحصول عليها، من المتوقع أن فجوة الطاقة المحظورة والخصائص البصرية والكهروحرارية لمادة $Rb_2AgSbCl_6$ يمكن تعديلها بفعالية عن طريق استبدال Br بمواقع Cl، مما يجعل سبائك $Rb_2AgSb(Cl_{1-x}Br_x)_6$ مرشحة واعدة للتطبيقات البصرية والإلكترونية الضوئية والخلايا الشمسية. كما ندرس أيضاً الخواص الإلكترونية لـ $Rb_2AgSb_{1-x}Bi_xX'_6$ سبائك حيث تأخذ x قيمًا تساوي صفرًا و 0.25 و 0.50 و 0.75 و 1 حيث يمثل X' كلور أو بروم أو أي.

الكلمات الرئيسية: الخصائص الإلكترونية. الخصائص البصرية ؛ التطبيقات الكهروضوئية ؛ نهج المبادئ الأولى ؛

Wien2k ,Vasp

General introduction

Lead-based halide perovskites (ABX_3) have revolutionized solution-processed solar cells, outperforming both polycrystalline and thin-film silicon photovoltaic technologies. In a remarkably short period, they have achieved record power conversion efficiencies exceeding 22% [1-3]. Among these, $APbX_3$ perovskites—where A is a large organic or inorganic cation (e.g., Cs^+ , $CH_3NH_3^+$), B is Pb, and X is Cl, Br, or I—have been extensively investigated [4-5]. Despite their impressive efficiency, commercialization faces significant hurdles, particularly due to lead's toxicity, which poses serious health and environmental risks and is subject to strict regulations in many countries. Additionally, these materials exhibit instability under humidity, air exposure, and temperature variations.

To address these challenges, extensive research has focused on developing lead-free, environmentally friendly, and air-stable halide perovskites. This pursuit has become a key area in perovskite optoelectronics [6]. Strategies to replace lead have included substituting it with other group 14 elements like Sn and Ge. However, these elements are prone to oxidation from the 2+ to the 4+ state, which undermines their viability [7-8]. A promising alternative involves the use of double perovskites with the formula $A_2M^+M^{3+}X_6$, where A is an alkaline metal, M^+ is a monovalent cation, M^{3+} is a trivalent cation, and X is a halide [9]. Lead-free halide perovskites have gained significant interest for applications in solar cells, LEDs, photodetectors, and lasers due to their exceptional properties, such as high carrier mobility, strong absorption, photoluminescence, and suitable band gaps for electronic devices [10-20].

However, many double-halide perovskites have large and indirect band gaps, limiting their efficiency [21]. To overcome this limitation, researchers have explored band gap engineering through alloying at specific atomic sites. Various techniques have been developed to synthesize double-perovskite alloys with optimized properties [22-23]. This article delves into modifying the band gap of $Rb_2AgSbCl_6$ through sublattice mixing,

with a detailed theoretical analysis. Sublattice mixing involves replacing Cl with Br at varying concentrations to improve the optical properties of $\text{Rb}_2\text{AgSbCl}_6$. Previous theoretical studies suggest that band gap tuning in $\text{Rb}_2\text{AgSbCl}_6$ can enhance its optoelectronic and photocatalytic performance [24]. This study examines the structural, electronic, optical and thermoelectric properties of $\text{Rb}_2\text{AgSb}(\text{Cl}_{1-x}\text{Br}_x)_6$ alloys using the full-potential augmented plane wave plus local orbital method. Furthermore, the spectroscopic limited maximum efficiency (SLME) model is applied to assess photoresponse and photovoltaic performance, identifying stable configurations with indirect band gaps and evaluating their potential as efficient solar cell absorbers. Also in this study, we emphasize electronic properties of $\text{Rb}_2\text{AgSb}_{1-x}\text{Bi}_x\text{X}'_6$ alloys, where x varies as 0, 0.25, 0.50, 0.75, and 1, and X' represents Cl, Br, or I. These compounds exhibit highly tunable characteristics in both crystal structure and electrical behavior, making them promising candidates for a broad range of applications. By incorporating different halogens (Cl, Br, and I), we aim to explore structural and optoelectronic variations and assess the influence of each halogen on the material's performance. This research seeks to advance the development of high-performance, environmentally friendly materials by providing critical insights into the relationship between structure and properties in lead-free halide double perovskites. This thesis manuscript is arranged in four chapters:

- ❖ **In the first chapter** we will briefly present an overview of perovskite for Solar Cells.
- ❖ **The second chapter** gives an overview of the density functional density functional theory which we have used to study the properties of the chosen properties of selected materials.
- ❖ **The third chapter** presents the structural electronic optical and properties of $\text{Rb}_2\text{AgSbCl}_6$ doped with bromine.
- ❖ **The fourth chapter** will be devoted to the detailed study of thermoelectric properties of $\text{Rb}_2\text{AgSb}(\text{Cl}_{1-x}\text{Br}_x)_6$ alloys

We will end up this manuscript with a general conclusion on the different points discussed above and some perspectives.

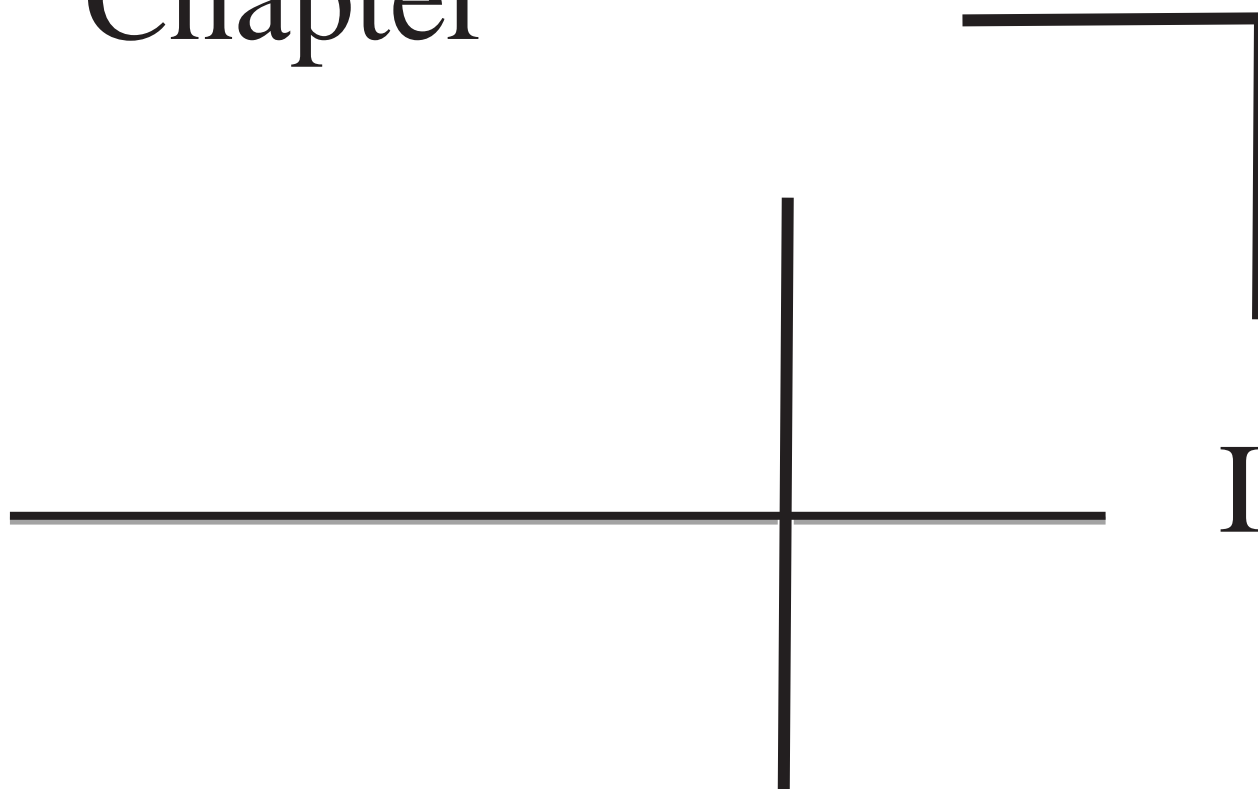
Reference

- [1] Seo, Jangwon, Jun Hong Noh, and Sang Il Seok. "Rational strategies for efficient perovskite solar cells." *Accounts of chemical research* 49.3 (2016): 562-572.
- [2] Kojima, Akihiro, et al. "Organometal halide perovskites as visible-light sensitizers for photovoltaic cells." *Journal of the american chemical society* 131.17 (2009): 6050-6051.
- [3] Jeon, N. J., Noh, J. H., Kim, Y. C., Yang, W. S., Ryu, S., & Seok, S. I. (2014). Solvent engineering for high-performance inorganic–organic hybrid perovskite solar cells. *Nature materials*, 13(9), 897-903.
- [4] Stranks, Samuel D., et al. "Electron-hole diffusion lengths exceeding 1 micrometer in an organometal trihalide perovskite absorber." *Science* 342.6156 (2013): 341-344.
- [5] Yokoyama, Takamichi, et al. "Overcoming short-circuit in lead-free CH₃NH₃SnI₃ perovskite solar cells via kinetically controlled gas–solid reaction film fabrication process." *The journal of physical chemistry letters* 7.5 (2016): 776-782.
- [6] Giustino, Feliciano, and Henry J. Snaith. "Toward lead-free perovskite solar cells." *ACS Energy Letters* 1.6 (2016): 1233-1240.
- [7] Noel, Nakita K., et al. "Lead-free organic–inorganic tin halide perovskites for photovoltaic applications." *Energy & Environmental Science* 7.9 (2014): 3061-3068.
- [8] Stoumpos, Constantinos C., et al. "Hybrid germanium iodide perovskite semiconductors: active lone pairs, structural distortions, direct and indirect energy gaps, and strong nonlinear optical properties." *Journal of the American Chemical Society* 137.21 (2015): 6804-6819.
- [9] Meng, Weiwei, et al. "Parity-forbidden transitions and their impact on the optical absorption properties of lead-free metal halide perovskites and double perovskites." *The journal of physical chemistry letters* 8.13 (2017): 2999-3007.
- [10] Deschler, Felix, et al. "High photoluminescence efficiency and optically pumped lasing in solution-processed mixed halide perovskite semiconductors." *The journal of physical chemistry letters* 5.8 (2014): 1421-1426.
- [11] Grätzel, Michael. "The light and shade of perovskite solar cells." *Nature materials* 13.9 (2014): 838-842.

- [12] Yantara, Natalia, et al. "Inorganic halide perovskites for efficient light-emitting diodes." *The journal of physical chemistry letters* 6.21 (2015): 4360-4364.
- [13] Tan, Zhi-Kuang, et al. "Bright light-emitting diodes based on organometal halide perovskite." *Nature nanotechnology* 9.9 (2014): 687-692.
- [14] Dou, Letian, et al. "Solution-processed hybrid perovskite photodetectors with high detectivity." *Nature communications* 5.1 (2014): 5404.
- [15] Bao, Chunxiong, et al. "High performance and stable all-inorganic metal halide perovskite-based photodetectors for optical communication applications." *Advanced materials* 30.38 (2018): 1803422.
- [16] Silfvast WT. *Laser Fundamentals*. Cambridge: Cambridge University Press; 2008. <https://doi.org/10.1017/CBO9780511616426>
- [17] Yettapu, Gurivi Reddy, et al. "Terahertz conductivity within colloidal CsPbBr₃ perovskite nanocrystals: remarkably high carrier mobilities and large diffusion lengths." *Nano letters* 16.8 (2016): 4838-4848.
- [18] Shi, Dong, et al. "Low trap-state density and long carrier diffusion in organolead trihalide perovskite single crystals." *Science* 347.6221 (2015): 519-522.
- [19] De Wolf, Stefaan, et al. "Organometallic halide perovskites: sharp optical absorption edge and its relation to photovoltaic performance." *The journal of physical chemistry letters* 5.6 (2014): 1035-1039.
- [20] Protesescu, Loredana, et al. "Nanocrystals of cesium lead halide perovskites (CsPbX₃, X= Cl, Br, and I): novel optoelectronic materials showing bright emission with wide color gamut." *Nano letters* 15.6 (2015): 3692-3696.
- [21] Mittal, Mona, et al. "Size of the organic cation tunes the band gap of colloidal organolead bromide perovskite nanocrystals." *The journal of physical chemistry letters* 7.16 (2016): 3270-3277.
- [22] Igbari, Femi, Zhao-Kui Wang, and Liang-Sheng Liao. "Progress of lead-free halide double perovskites." *Advanced Energy Materials* 9.12 (2019): 1803150.

- [23] Du, Ke-zhao, et al. "Bandgap engineering of lead-free double perovskite Cs₂AgBiBr₆ through trivalent metal alloying." *Angewandte Chemie International Edition* 56.28 (2017): 8158-8162.
- [24] Karmakar, Abhoy, et al. "Tailorable indirect to direct band-gap double perovskites with bright white-light emission: decoding chemical structure using solid-state NMR." *Journal of the American Chemical Society* 142.24 (2020): 10780-10793.
- [25] Asghar, Mazia, et al. "A computational insight of the lead-free double perovskites Rb₂AgSbCl₆ and Rb₂AgSbBr₆ for optoelectronic and thermoelectric applications." *International Journal of Energy Research* 46.15 (2022): 24273-24285.
- [26] Madsen, Georg KH, et al. "Efficient linearization of the augmented plane-wave method." *Physical Review B* 64.19 (2001): 195134.
- [27] Schwarz, Karlheinz, Peter Blaha, and Georg KH Madsen. "Electronic structure calculations of solids using the WIEN2k package for material sciences." *Computer physics communications* 147.1-2 (2002): 71-76.
- [28] Blaha, Peter, et al. "WIEN2k: An APW+ lo program for calculating the properties of solids." *The Journal of chemical physics* 152.7 (2020).
- [29] Wu, Zhigang, and Ronald E. Cohen. "More accurate generalized gradient approximation for solids." *Physical Review B* 73.23 (2006): 235116.
- [30] Tran, Fabien, and Peter Blaha. "Accurate band gaps of semiconductors and insulators with a semilocal exchange-correlation potential." *Physical review letters* 102.22 (2009): 226401.

Chapter



I

perovskite for Solar Cells

I.1 Introduction

In a few short years, halogenated perovskites have emerged as promising candidates for photovoltaic applications. Their typical properties enable perovskite cells to nearly match the conversion efficiencies of silicon cells, which are the most prevalent and well-established technology. This first chapter provides the background and objectives of this thesis. It begins by detailing the various properties of perovskite, followed by an overview of different deposition techniques for this material. Next, it explains the operation of photovoltaic cells, with a focus on both silicon and perovskite cells. Finally, the chapter introduces the concept of light trapping and how it is used in solar cells.

I.2 THE SOLAR CELLS

I.2.1 History

The history of solar cells dates back to 1839, when French physicist Edmond Becquerel [1] discovered the photovoltaic effect. He showed that exposure to light caused an electric current to form between two electrodes coated with silver chloride or oxidized copper and immersed in an electrolyte. He investigated the variation in intensity based on the wavelength used, marking the first study of the photoelectric effect. After Willoughby Smith discovered the photoconductivity of selenium in 1873, William Grylls Adams and Richard Evans Day demonstrated the photovoltaic effect in a selenium rod [2.3]. Around 1883, Charles Fritts created the first selenium solar cell, which had an efficiency of 1% [4]. This cell consisted of a selenium film sandwiched between a copper electrode and a semi-transparent gold electrode. To achieve higher efficiencies, D. Chapin, C. Fuller, and G. Pearson of Bell Labs introduced the first silicon-based solar cells with a P-N [5] junction in 1954, achieving 5% efficiency and paving the way for photovoltaic panels. Due to their high cost, these cells were initially used only in space research to power satellites needing long-lasting energy. Rapid advancements soon increased the efficiency to 9%. In 1958, the first solar cells were launched on the Vanguard 1 satellite [6]. This was followed by the installation of the first solar panels on the Explorer 6 satellite in 1959 [7]. Their successful use in these applications demonstrated their reliability and robustness. From the 1970s onwards, photovoltaic panels began to be developed for use on land and at sea, providing power to areas without access to an electricity grid. Since then, the cost of solar panels has steadily decreased.

A more precise understanding of the physical phenomena involved in converting light to current in silicon has led to the development of new cells with increasingly complex structures and materials. The goal is to enhance efficiency, optimize manufacturing processes, and integrate these advancements into solar panels. This has driven research into new materials such as III-V semiconductors, which are composed of elements from groups III and V of the periodic table. In 1970, Zhores Alferov's team in the USSR developed solar cells based on gallium arsenide (GaAs), demonstrating the high efficiency of this compound material [8]. A decade later, advancements in GaAs research enabled higher yields than those achieved with crystalline silicon-based cells. From the 1990s on, GaAs cells replaced silicon as the most commonly used type for space applications. Later, double- and triple-junction solar cells based on GaAs with layers of germanium and gallium-indium phosphide were developed, achieving record efficiencies of 32%. These cells powered the Mars Exploration Rover missions, Spirit and Opportunity, which explored Mars from 2004 to 2019 [9]. Other materials have also emerged, including cadmium telluride, copper indium gallium selenide, amorphous silicon thin films, and organic-inorganic hybrid perovskites. Intense research over the past decade has focused on perovskites due to their high efficiency and low manufacturing costs. The first perovskite-based cells, developed by Tsutomu Miyasaka's team, achieved conversion efficiencies of 4% [10]. Since then, research teams worldwide have made rapid progress, and by 2016, some laboratories had boosted the efficiency of perovskite-based cells to over 22%, comparable to silicon cells. This rapid advancement has made perovskite the fastest-developing solar technology in history [11].

1.2.2 Principles of solar cell operation

The photovoltaic effect is the mechanism that transforms light into electricity within a solar cell composed of semiconductor material. Although a semiconductor typically behaves as an insulator, it can act as a conductor when its valence electrons are excited into the conduction band. When a photon is absorbed photoelectrically by the material, it imparts its energy to an electron. If this energy surpasses the semiconductor's band gap—the energy difference between the valence band and the conduction band—the electron moves into the conduction band, creating a hole in the valence band. Consequently, the semiconductor transitions into a conductive state.

To enhance conductivity, specific impurities are added to the semiconductor in a precise process called doping, which can be of two types: P-type and N-type. N-type doping involves introducing electron-donor atoms to the semiconductor to increase the number of free electrons, while P-type doping involves adding electron-acceptor atoms to increase the number of holes. For instance, in a silicon crystal, each silicon atom bonds with four neighboring atoms using its four valence electrons. If a silicon atom is replaced by an atom with five valence electrons, like phosphorus, one electron remains unbonded and free to move, resulting in an N-doped semiconductor. Conversely, if an atom with three valence electrons, such as boron, is introduced, a hole is created due to the missing electron needed for bonding, resulting in a P-doped semiconductor.

Doping, therefore, produces the appearance of new electron acceptor and donor levels in the band structure of the doped material. These levels appear between the conduction band and the valence band, i.e., in the gap.

The PN junction, depicted in **figure I.1**, occurs where a P-doped region meets an N-doped region. At this junction, free electrons from the N-doped side fill the holes in the P-doped side, creating a "depletion zone" or "space charge zone" devoid of mobile charges. Additionally, an electric field is established from the N region to the P region.

A solar cell is typically a PN junction photodiode that produces current when exposed to light. The efficiency of photovoltaic conversion primarily relies on three key physical processes: the absorption of light by the material, the conversion of photon energy into electrical charge, and the collection of these charges.

Optical and electrical properties must therefore be optimized for photovoltaic conver

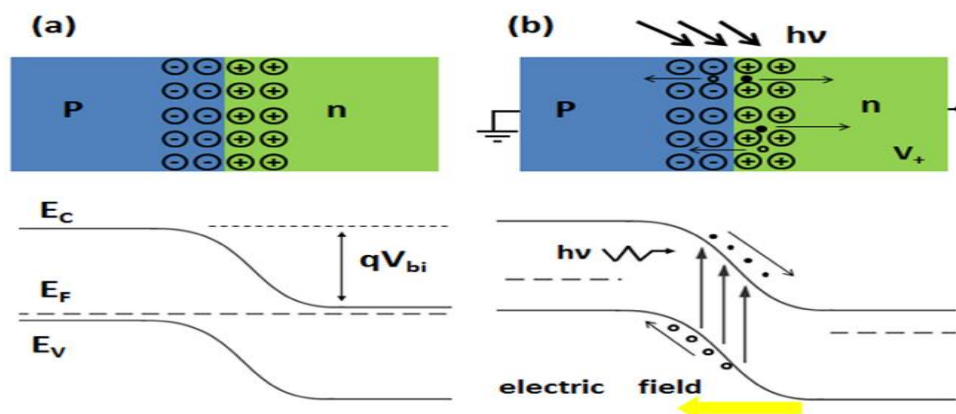


Figure I.1: Diagram of a p-n junction under equilibrium conditions (a) and under illumination (b)

Absorption must be optimized across the entire solar spectrum. As illustrated in **figure I.2**, this spectrum ranges from ultraviolet (UV) to far infrared (IR), with a peak emission around 500 nm. The maximum solar power reaching the Earth's surface is approximately 1,000 W/m² for a surface oriented perpendicular to the radiation.

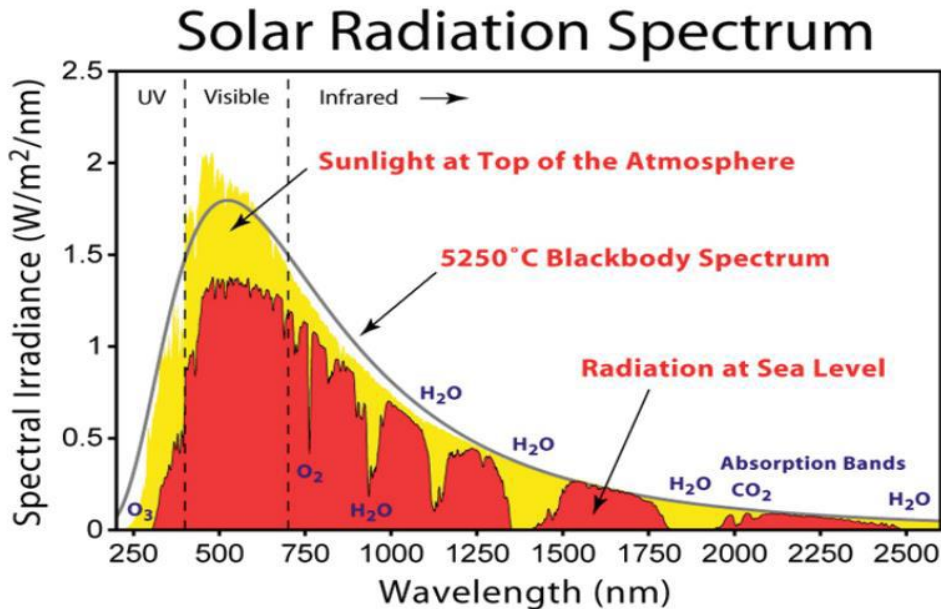


Figure I.2: the solid black line, representing the emission from an ideal black body, depicts the solar spectrum [12].

The yellow spectrum indicates the extraterrestrial sunlight spectrum (air mass (AM) = 0), while the red spectrum shows the terrestrial sunlight spectrum (air mass (AM) = 1.5).

Following photon absorption, the electron-hole pairs created, commonly referred to as "excitons," will behave differently depending on whether the interaction takes place in the N and P regions or in the space charge zone. When charges are created in the depletion zone, they are immediately separated by the prevailing electric field. Holes and electrons move to the P and N regions, respectively. This charge transport produces a current known as the "photo generation current." In the N and P regions, the charges created are not subjected to an electric field but diffuse over a length, called the diffusion length, which depends on the material's characteristics. This length corresponds to the average distance traveled by a charge carrier before recombination. It is not the same for electrons and holes and is expressed as:

$$L = \sqrt{D\tau} \quad (I.1)$$

With D the charge carrier diffusion constant and τ its lifetime.

Charges that diffuse into the space charge zone contribute to the generation of a current known as the "diffusion current." The total photonic current is the sum of the generation current and the diffusion current, directly proportional to the incident light absorbed. Metallic contacts positioned on both sides of the semiconductor enable this current to flow into an external circuit. Typically, these contacts form a grid on the front face and a solid surface on the rear face of the solar cell.

I.2.2.1 A solar cell's characteristics

Typically, a photovoltaic cell is defined by its current-voltage (I-V) curve, which is obtained under calibrated illumination equivalent to the power of sunlight. The measurement involves applying an electrical voltage between the two semiconductor electrodes and measuring the resulting current flow.

The current-voltage characteristic of a photodiode without illumination is similar to that of a conventional diode (electronic component). When the photodiode is forward-biased, an exponential increase in current is observed. When the photodiode is reverse-biased, a small reverse saturation current appears. This current is known as the black current and is significantly temperature-dependent :

$$I_D = I_s \left[\exp\left(\frac{qV}{kT}\right) - 1 \right] \quad (I.2)$$

I_D is the dark current, I_s is the inverse saturation current, q is the electron charge, V is the applied voltage, k is Boltzmann's constant, and T is the absolute temperature.

When the photodiode is illuminated, the current-voltage characteristic is shifted by the amount of photo-current. We therefore have :

$$I_{\text{total}} = I_s \left[\exp\left(\frac{qV}{kT}\right) - 1 \right] - I_p \quad (I.3)$$

With I_p , photo-current.

This equation, also referred to as the Shockley equation [13.14], is depicted in Figure 1.3, illustrating the characteristic curve both in the presence and absence of illumination. The current is expressed as current density, which is the ratio of current to the active cell surface area. This curve is essential for determining key solar cell parameters, including

the short-circuit current density (J_{sc}), open-circuit voltage (V_{oc}), and maximum power output (P_{max}).

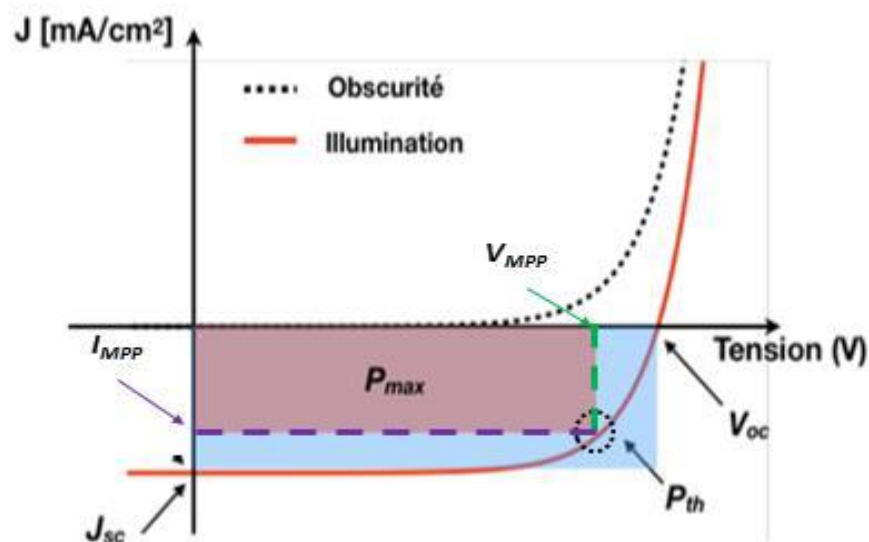


Figure I.3: A schematic diagram shows a J-V curve in darkness (black dashed line) and under illumination (red solid line).

The red rectangle indicates the cell's maximum output power, " P_{max} ," while the blue rectangle represents the maximum power of an ideal cell, " P_{th} ." The fill factor (FF) is calculated by comparing the areas of these two rectangles. The current generated by the cell under illumination at zero voltage is " J_{sc} ," and the voltage at zero power density is the open-circuit voltage, " V_{oc} " [15].

The open-circuit current (J_{sc}) is the highest current a solar cell can produce and occurs when the voltage is zero. Its value increases with the intensity of incident light and is influenced by carrier mobility, temperature, illuminated surface area, and the wavelength of the incident radiation [16, 17]. The open-circuit voltage (V_{oc}) is the voltage at which the current flow is zero. The product of V_{oc} and J_{sc} gives the maximum power, P_{ideal} , for an "ideal" cell. Under real-life conditions, the actual maximum power, P_{real} , is derived from the power versus voltage (V) curve. The peak of this curve determines the actual maximum voltages, V_m and J_m .

The ratio of P_{real} to P_{ideal} power quantifies the efficiency of converting absorbed light into electrical power. This value, known as the fill factor (FF), ranges from 0 to 1. A higher fill factor means greater efficiency (**Figure 1.3**).

Efficiency, denoted as " η ," is the primary parameter of a photovoltaic cell. It represents the ratio of the maximum power output, P_{real} , to the incident power, P_{inc} . This metric is commonly used to compare different photovoltaic cells.

Despite the high absorption efficiency of visible photons, the theoretical maximum efficiency of a single-junction PN cell is limited. Shockley and Queisser calculated this limit to be around 33% [18]. The main power losses result from the mismatch between the energy of incident photons (ranging from 0.5 to 2.9 eV in the solar spectrum) and the semiconductor gap. Photons with energy lower than the gap are not absorbed and are lost, while photons with higher energy release excess energy as heat instead of electricity, increasing the cell's temperature and reducing efficiency. Additionally, other factors related to material quality, such as electron/hole pair recombination, also decrease efficiency.

Shockley and Queisser's model can be used to determine the maximum possible efficiency of a cell based on the semiconductor gap when exposed to 1.5 G solar radiation under air mass conditions. This efficiency limit is illustrated in Figure 1.4, which also displays the efficiencies achieved with the most common single-junction semiconductors.

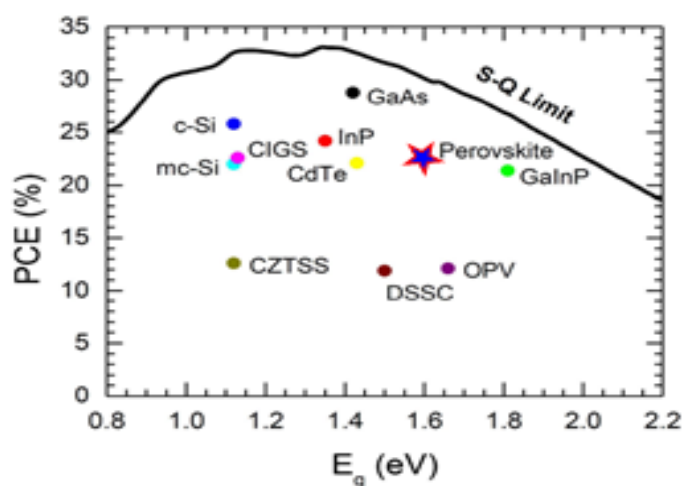


Figure 1.4: Shockley-Queisser efficiency limit as a function of the gap considering solar radiation (AM 1,5 G) [19,20]

Researchers are exploring various cell concepts and architectures, including multi-junction solar cells, to overcome this limit. These cells use different materials with varying electron gap values, each selected to absorb light at a specific energy within the solar spectrum. This approach significantly enhances the overall current produced

I.2.2.2 State-of-the art solar cells

Numerous technologies are based on the photovoltaic effect, many of which are still in the research and development stages. The National Renewable Energy Laboratory (NREL) updates a graph biannually, illustrating the progression of record efficiencies for most photovoltaic technologies from 1976 to the present (see *Figure 1.5*). These efficiencies are measured using a standardized international protocol by independent laboratories [21]. The graph uses different colors to represent various technology families: crystalline silicon cells, single-junction gallium arsenide cells, multi-junction cells, thin-film technologies, and emerging technologies. Each of the 28 sub-categories is marked with distinctive colored symbols, with the latest world record for each technology highlighted along the right-hand edge, showing the efficiency and corresponding symbol.

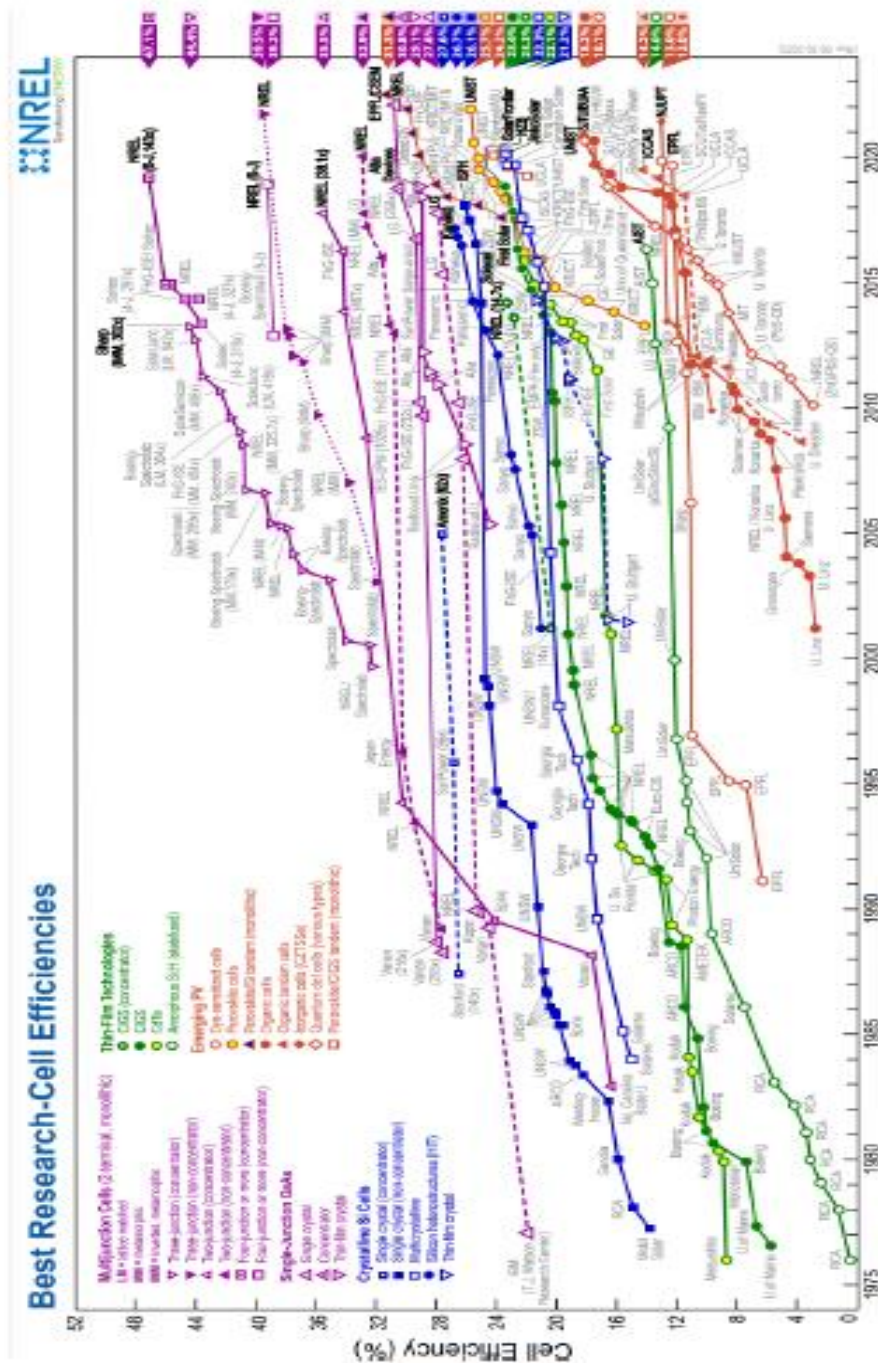


Figure I.5: Record efficiencies of solar cells and photovoltaic modules from 1976 to 2022, classified by technology [22].

The graph in **Figure I.5** illustrates perfectly both the great diversity of photovoltaic technology and the constant progress made, year after year, in efficiency performance.

To maintain clarity, we can categorize these technologies into four primary groups: crystalline silicon cells, thin-film cells, organic photovoltaic cells, and hybrid cells.

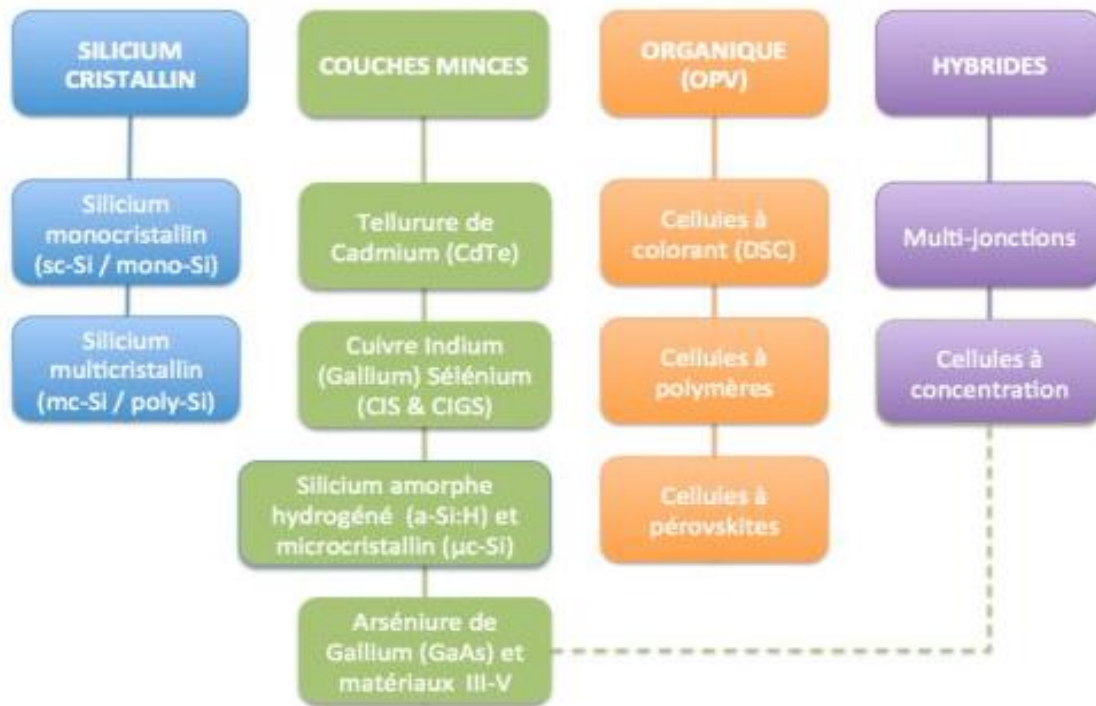


Figure I.6: Classification of the main solar cell technologies: crystalline silicon, thin film, organic, and hybrid [23].

Crystalline silicon cells, utilizing doped silicon as the active element, are the oldest and most prevalent solar technology, comprising over 80% of the market for solar panel materials. Their popularity is due to their durability, high yield performance, and long lifespan of several decades. This mature technology has seen significant investment in silicon processing, cell production, and module assembly. Crystalline silicon cells are divided into two types: monocrystalline and polycrystalline. Monocrystalline silicon cells offer very high efficiency (20%) but come with relatively high production costs [24].

The Czochralski process, a delicate and energy-intensive method of crystallogenesis, is used to produce single crystals [25.26]. While this technique is well-known and utilized in the microelectronics industry, the single crystals formed as rods restrict the size of a solar cell to that of a silicon wafer. In contrast, polycrystalline silicon solar cells are easier and less expensive to manufacture.

Polycrystalline silicon is created by remelting purified silicon blocks and cooling them in a rectangular ingot mold. While their efficiency ($\eta \sim 11\text{--}15\%$) is lower than that of monocrystalline silicon, they are less sensitive to ambient temperature. This makes polycrystalline cells particularly suitable for regions with abundant sunlight [27].

Thin-film solar cells feature a thin semiconductor layer, only a few microns thick, applied to a substrate such as glass (solid), plastic (flexible), or metal (flexible). The most commonly used semiconductor materials include hydrogenated amorphous silicon (a-Si), cadmium tellurium (CdTe), copper indium gallium (di) selenide (CIGS), and copper zinc tin sulfide (CZTS). Unlike crystalline silicon cells, which are 200 to 300 μm thick, thin-film cells are lighter, often more flexible, and easier to manufacture, making them less expensive. However, they have lower efficiency, and their performance degrades quickly over time. Despite this, thin-film cells have a much faster energy payback time (the time it takes for a solar cell to generate the amount of energy used to produce it) compared to crystalline silicon cells [28].

The main thin-film solar cell technologies developed are described below:

- ✚ **Hydrogenated amorphous silicon:** is utilized in p-i-n junction cells. This configuration has reached efficiencies near 10% for commercial cells and 21.5% in laboratory settings [29]. However, these solar cells' efficiency is significantly impacted by light, which creates dangling bonds that serve as charge carrier traps, resulting in a performance decline of 10% to 20% within the first few months of use.
- ✚ **Cadmium telluride solar cells :** have efficiencies of approximately 12.5% for commercial versions, with an experimental cell from First Solar achieving 18.7% efficiency. While tellurium is a rare element and cadmium is highly toxic, these cells are less sensitive to changes in ambient temperature compared to crystalline cells, losing only 3% of their power per 10 °C increase, compared to 5% for crystalline cells. Additionally, cadmium telluride cells offer excellent long-term stability [30, 31].
- ✚ **Copper indium gallium (di)selenide (CIGS):** CIGS cells are made of copper, gallium, indium, and selenium. They feature a 1 to 2.5 μm -thick p-doped layer coated with an n-type material, such as cadmium sulfide (CdS), which is only 40 to 70 nm thick. The highest efficiency achieved is 20.4% for a low-cost, rigid-thin structure and 19% for a flexible structure. These cells have very low thermal sensitivity, even lower than CdTe cells. Additionally, they do not contain toxic elements, thus minimizing environmental and health impacts.

- ✚ **Copper, zinc, and tin sulfide:** CZTS cells consist of copper, zinc, tin, sulfur, and selenium, with the formula $\text{Cu}_2\text{ZnSnS}_4$. Their optical properties are similar to those of CIGS cells, but they use abundant, non-toxic elements, unlike tellurium or indium. Additionally, these compounds are much cheaper. However, their experimental efficiency is only 11.1%, about half that of CIGS cells.
- ✚ **Gallium arsenide (GaAs):** It is a reference system for thin-film solar cells. They show very high laboratory efficiencies on single-junction devices (30%). They have the advantage of being lightweight, flexible, and having good thermal resistance, and they continue to produce electricity under poor weather conditions (rain, clouds, etc.). They are mainly used for space applications. However, the production of GaAs-based solar cells remains costly and requires a well-controlled packaging process.

To reduce manufacturing costs and improve energy efficiency, extensive research has centered on organic photovoltaic cells [32, 33]. These cells consist of organic molecules distributed across the active layer. The technology offers advantages such as simple and low-energy manufacturing processes (like screen printing, centrifugal coating, or inkjet methods) using abundant and inexpensive materials. They can be deposited on flexible substrates in various colors. Moreover, they require relatively small quantities of materials, typically with film thicknesses around a hundred nanometers.

I.2.3 Advantages and disadvantages of solar energy

I.2.3.1 Advantages

- ✓ High reliability is ensured by most photovoltaic module manufacturers, who offer warranties that typically extend up to 25 years.
- ✓ The modular nature of photovoltaic panels allows for easy adaptation to applications ranging from milliwatts to megawatts in power ratings.
- ✓ Low operational and maintenance expenses.
- ✓ This technology has a beneficial environmental impact.

I.2.3.2 Disadvantages

- ✓ The manufacturing cost of specific photovoltaic systems remains elevated due to initial investment requirements.

- ✓ Solar installations require substantial land area for operation.
- ✓ Limited competition exists between solar generators and diesel or natural gas generators.
- ✓ The efficiency remains relatively modest as of now (28% is currently available).
- ✓ The critical factor is energy storage, which necessitates batteries and affects the installation costs.

I.3 The perovskite materials

I.3.1 Description and definition of perovskite

The term "perovskite" originally described a cubic, grayish mineral made of calcium titanate oxide (CaTiO_3). This mineral was discovered in 1839 by A.B. Kemmerer during an expedition in the Ural Mountains, Russia. Concurrently, mineralogist Gustave Rose examined the mineral and named it perovskite in honor of Lev Alexeievitch Perovski [34]. Since then, various materials with a crystalline structure similar to CaTiO_3 have been discovered and studied for their physical properties, including ferroelectricity [35], ferroelasticity [36], and ferromagnetism [37].



Figure I.7: Perovskites in nature

Several years after the discovery of CaTiO_3 , Christian Moller showed that this perovskite oxide crystallizes in an orthorhombic structure at room temperature with $a = 5.367 \text{ \AA}$, $b = 7.644 \text{ \AA}$, and $c = 5.444 \text{ \AA}$ in a Pcmn [38] space group. The crystalline structure is described as TiO_6 octahedra linked by their vertices in the three directions of space. The

interstices between the TiO_6 octahedra contain Ca^{2+} cations. The name "perovskite" therefore refers to materials with a crystalline structure similar to CaTiO_3 , generally formulated by the chemical structure ABX_3 , where A and B are mainly cations and X is an anion. For several decades, perovskite oxides (with $\text{X} = \text{O}_2$) have been widely studied. The chemical versatility of this material allows its formula to be modified by substituting the oxide with chalcogens like $\text{X} = \text{S}^{2-}$, Se^{2-} , and Te^{2-} , or halogens like $\text{X} = \text{Cl}^-$, Br^- , and I^- . Numerous anion and cation combinations can form a perovskite. However, specific conditions are necessary for perovskite formation: chemical neutrality among elements A, B, and X, strong octahedral stability, and adherence to the Goldschmidt tolerance factor [39].

1.3.2 History of perovskites

The family of perovskite oxides has seen remarkable growth since the 1940s, beginning with the discovery of BaTiO_3 's ferroelectric properties in 1946 [40]. Over the decades from the 1940s to the 2000s, numerous perovskite oxide compounds have been identified. Examples include BaTiO_3 and $\text{Pb}_3\text{MgNb}_2\text{O}_3$, which are used in capacitors; PbZrTiO_3 for piezoelectric materials and/or superconductors; and $\text{Ba}_2\text{Cu}_3\text{O}_3$. Additionally, during this period, the first two-dimensional perovskite, with the general formula $\text{Bi}_2\text{A}_{n-1}\text{BnO}_{3n+3}$, was developed [41]. It possesses ferroelectric properties and high ionic conductivity. While perovskite oxides were extensively researched during this period, a different type of perovskite was synthesized in 1884: the 2D halogenated hybrid perovskite $(\text{CH}_3\text{NH}_3)_2\text{CuCl}_4$. This structure is termed "hybrid" because the cation A is an organic molecule and "halogenated" because the anion X is a halogen (I^- , Br^- , Cl^-). A few years later, the first lead-based halogenated 3D perovskites, such as CsPbX_3 , were synthesized. It was only much later that the crystallographic structure and optoelectronic properties of these compounds were documented [42-43]. In 1958, Weber replaced the monovalent cation Cs^+ with an organic molecule, resulting in the first three-dimensional halogenated hybrid perovskite, $\text{CH}_3\text{NH}_3\text{PbI}_3$. Subsequent research focused on 3D halogenated hybrid perovskites with the chemical formula $(\text{CH}_3\text{NH}_3)\text{PbX}_3$, where X represents the halogens I^- , Br^- , and Cl^- [44]. The 2D halogenated hybrid perovskite $(\text{C}_n\text{H}_{2n+1}\text{NH}_3)_2\text{MnCl}_4$ has shown luminescent properties, which allowed us to create the first LED with an efficiency of 0.11% [45]. Halogenated perovskites, due to their remarkable optoelectronic properties, have been highly popular since the 1990s, making

them strong contenders in various fields such as diodes and photovoltaics. The first solar cell made from 3D halogenated perovskite $(\text{CH}_3\text{NH}_3)\text{PbI}_3$, also known as MAPI, achieved an efficiency of 3.8% and is regarded as a benchmark for this type of material. Since then, efforts to improve the efficiency of perovskite-based solar cells have continued, with a record efficiency now reaching 25.5% [46]. MAPI's optoelectronic properties allow it to absorb the entire solar spectrum, from visible light to near infrared. However, it is unstable with temperature fluctuations and humidity. Alternatives like $\text{CH}_3\text{NH}_3\text{PbBr}_3$, FAPbBr_3 , and CsPbBr_3 perovskites offer better stability in atmospheric conditions but have reduced spectral absorption, leading to lower external yields in solar cells. The use of lead in halogenated perovskites is controversial due to toxicity and environmental concerns. To address this, perovskites with other metal cations such as Sn^+ , Sb^+ , Ti^+ , Ge^+ , or Cu^+ have been synthesized. The highest external efficiency achieved so far is 11.22% with a FASnI_3 -based solar cell [47].

This thesis will study perovskites with high yields, specifically lead-free halide-based multi-cation and mixed halogen systems.

1.3.3 The crystalline arrangement of perovskite materials

Depending on the choice of origin, the structure can be described in two ways. In the first method (*Figure 1.7*), A is at the origin (position 1a: 0, 0, 0), B is at the center of the cube (position 1b: $\frac{1}{2}$, $\frac{1}{2}$, $\frac{1}{2}$), and the X atoms are in the middle of each edge (position 3d: 0, 0, $\frac{1}{2}$). In the second method, shifting the origin by the vector $(\frac{1}{2}, \frac{1}{2}, \frac{1}{2})$ places A at position 1b ($\frac{1}{2}, \frac{1}{2}, \frac{1}{2}$), B at position 1a (0, 0, 0), and the X atoms in the middle of each face (position 3c: 0, $\frac{1}{2}$, $\frac{1}{2}$). This arrangement is known as a face-centered cubic type stack (ABCABC). These compounds have the general formula ABX_3 , where A is a large cation (such as Sr, Ba, Pb, or Bi), B is a smaller cation (such as Ti, Zr, Fe, or Sc), and X is typically a halide ion [48]. In its classical form, described as a stack of polyhedra, the X anions and B cations create regular BX_6 octahedra connected at their vertices along the [100] directions of the cube. The larger A cations are positioned at the center of the large octahedral cavities formed by 8 BX_6 octahedra. This is the structure of the compound SrTiO_3 at room temperature, for example [49]. For over four decades, ABO_3 perovskite oxides have attracted significant interest due to the ease of altering the cations A and B in their structure. Changing these elements can modify the material's properties, allowing for a wide range of physical characteristics (such as semi-metallicity, semi-conductivity,

ionic conductivity, metal conductivity, and superconductivity) depending on the chemical and electronic nature of the A and B atoms [50].

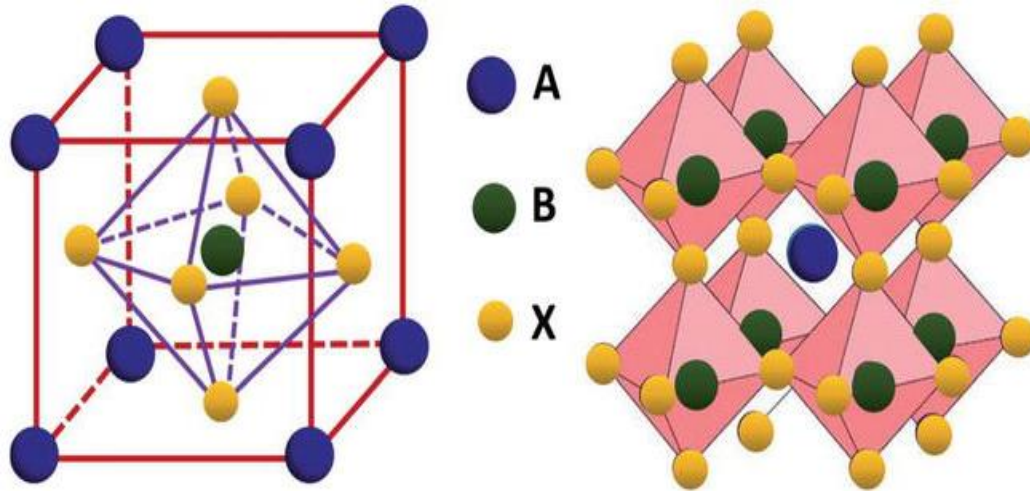


Figure 1.8: The ideal structure for ABX_3 perovskite [51].

The crystal lattice of an ideal perovskite structure is a centrosymmetric simple cubic, forming a compact three-dimensional stack that almost entirely prevents the formation of interstitial compositions. Consequently, it is often described as a network of BO_6 octahedra connected at their vertices, as illustrated in *Figure 1.8* [52].

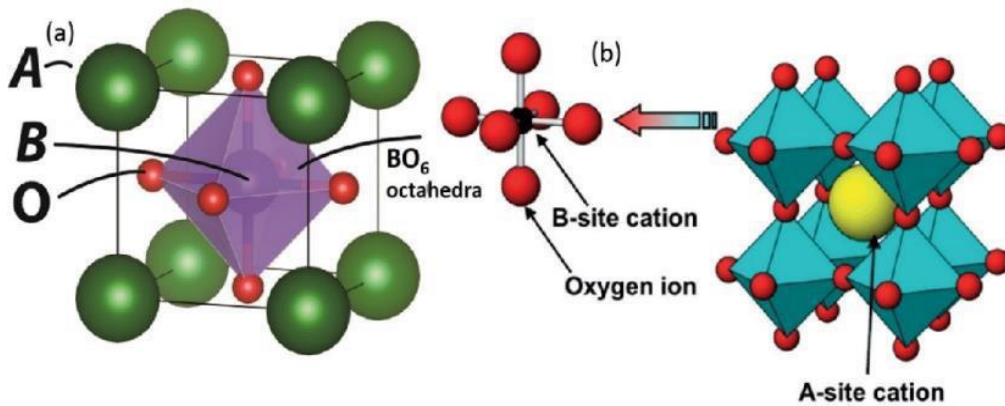


Figure 1.9: Three-dimensional arrangement of BO_6 octahedra in the perovskite structure.

I.3.3.1 Type of perovskite structure

I.3.3.1.a Simple perovskite structures

Generally, the fundamental crystal lattice of an ABO_3 perovskite is cubic. It consists of octahedra formed by six oxygen anions, with alkaline earth cations located at the corners

of the cube (12-coordination) and B transition cations at the center (octahedral coordination). In ABO_3 structures, the A and B sites are occupied by a single type of atom; examples include $SrTiO_3$, $BaTaO_3$, and $PbTiO_3$ [53].

I.3.3.1.b The complex perovskite structures

These are perovskites where either the A or B site is occupied by two types of atoms. The distribution of these atoms can be random or ordered, as seen in compounds used for making capacitors. These structures follow the ABO_3 format, with either the A or B sites occupied by two types of atoms. For example, $K_{0.5}Bi_{0.5}TiO_3$ and $Na_{0.5}Bi_{0.5}TiO_3$ [54].

I.3.4 The different families of perovskite

I.3.4.1 The perovskite oxides ABO_3

Complex oxides with a perovskite structure have garnered significant interest and have been extensively studied for over 50 years. The chemical formula of perovskite is ABO_3 , consisting of a divalent cation A, a metal cation B, and oxygen as an anion [55].

I.3.4.2 Halogen perovskites

Halogenated perovskites have been extensively studied since 2012. When the cation A in the ABX_3 perovskite is an organic cation, the material is known as a hybrid perovskite. In this structure, X is a halide (Cl^- , Br^- , or I^-), and B is a divalent ionic metal such as Pb^{2+} or Sn^{2+} , as well as Cu^{2+} , Co^{2+} , Fe^{2+} , Mn^{2+} , Cr^{2+} , Ge^{2+} , Eu^{2+} , Cd^{2+} , or Yb^{2+} . These halogenated perovskites can also be entirely inorganic when the cation A is an alkali metal like cesium (Cs^+) [56].

I.3.5 Transition from single to double perovskites

I.3.5.1 Simple perovskite materials containing halogens

Simple perovskite halides are a category of materials characterized by a perovskite-type crystal structure, which features a cube-shaped arrangement with a metal ion at the center surrounded by halide ions. These compounds have the formula ABX_3 , where A represents an alkali cation, B denotes a metal cation, and X denotes a halide anion.

These materials are increasingly investigated for their potential as photovoltaic materials due to their optimal band gap for efficient conversion of solar energy into electricity. Moreover, they can be produced from solutions, enabling cost-effective, large-scale manufacturing. However, challenges such as long-term stability and toxicity need to be addressed before they can be widely adopted for commercial photovoltaic applications.

I.3.5.2 Doubles Pérovskites

Ordered double perovskite oxides were first proposed by WARD and LONGO in 1960. They consist of two alternating simple perovskites (ABO_3) and ($A'B'O_3$) along the three crystallographic directions. They are designated by a general formula ($AA'BB'O_6$) where A and A' can be alkaline earth metals or lanthanides, and B and B' are transition metals. This structure was first proposed by Longo and Ward in 1961 [57]. It is derived from the perovskite ABO_3 when half of the octahedral BO_6 is replaced by other suitable octahedral $B'O_6$ cations, where the A cation is typically a large cation with a low oxidation state and B is a smaller cation, either a transition metal or a lanthanide. In the case of the ABO_3 perovskites studied, depending on the type of A and B cations involved, the cubic symmetry of the prototype perovskite structure can be lowered. In the ideal structure, the ions are tangent to each other. The BO_6 octahedra are then perfectly aligned, forming an undistorted three-dimensional lattice of cubic symmetry. The stability of this ideal structure depends on the respective ionic radii of the cations and anions, as well as the difference in electronegativity between the cations and anions.

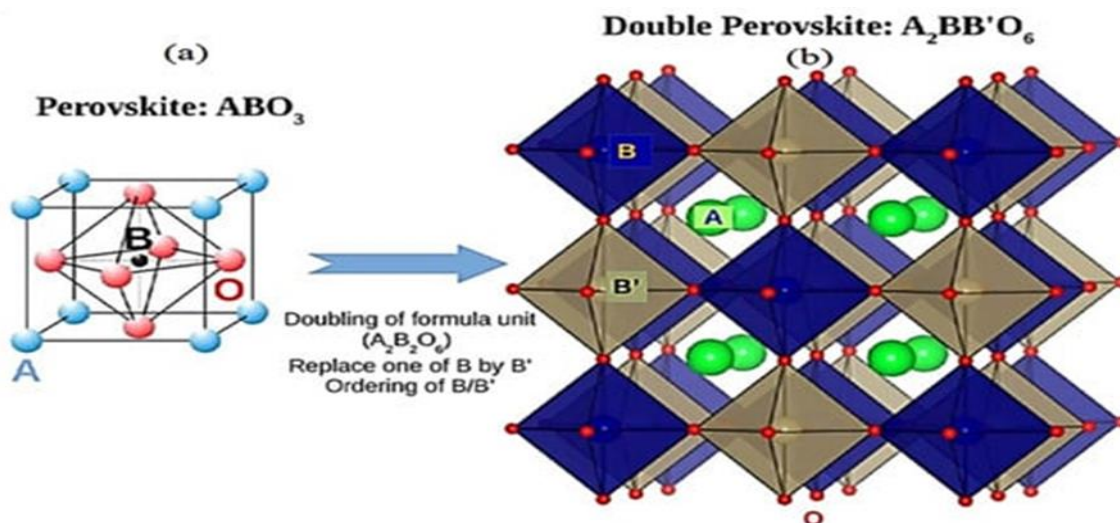


Figure I.10: Structures of different perovskites: (a) ideal perovskite ABO_3 and (b) double perovskite $A_2BB'O_6$.

I.3.6 Criteria for the stability of the perovskite structure

The stability of the perovskite structure is influenced by several factors, such as the size of the cations and anions, the pressure and temperature conditions, and the bonding forces between atoms. Nonetheless, there are general criteria that can help assess the stability of the perovskite structure:

- The stability of the perovskite structure increases when cation A is larger than cation B. This is due to the polarization effect, which enhances the electrostatic interaction between ions of differing sizes.
- The radius ratio between cations A and B is crucial for the stability of the perovskite structure. The critical radius ratio is 0.414; if the ratio falls below this value, the perovskite structure becomes unstable.
- Coordination geometry: The perovskite structure features an octahedral coordination, where both the A and B cations are each surrounded by six anions. Any disturbance in this coordination geometry can impact the stability of the structure.
- Crystal symmetry: The perovskite structure typically has cubic symmetry. Any disruption to this symmetry can negatively affect the stability of the structure.

I.3.6.1 Goldschmidt tolerance factor (t)

The introduction of a quantitative tolerance factor allows for the classification of various perovskite structures based on the ionic radii of the A, B, and X ions (denoted as r_A , r_B , and r_X , respectively). This factor considers each ion as a hard sphere, determining whether they are in contact when the ideal perovskite structure is present :

$$t = \frac{r_A + r_X}{\sqrt{2}(r_B + r_X)} \quad (I.4)$$

Then we can write:

$$a = 2r_O + 2r_A \quad (I.5)$$

On the other hand, along the diagonal of a face from the ionic radii of atoms A and O (origin at A):

$$a\sqrt{2} = (2r_O + r_A) \quad (I.6)$$

In the ideal case, it is therefore possible to write :

$$r_O + r_A = \sqrt{2} r_O + r_B \quad (1.7)$$

Or :

$$\frac{r_O + r_A}{\sqrt{2} r_O + r_B} = 1 \quad (1.8)$$

Where r_A , r_B and r_O are respectively the ionic radii A (in 12-coordination), B (in 6-coordination) and O, given by Shannon and Prewitt [58-59]. Generally, the radii of the A, B and O ions do not correspond to the ideal dimensions of the prototype structure and a tolerance factor t , called the Goldschmidt factor [60], has been added as follows :

$$t = \frac{r_O + r_A}{\sqrt{2} r_O + r_B} \quad (1.9)$$

This geometrical factor indicates how much the perovskite deviates from its ideal structure, suggesting a possible deformation. However, it only serves as an indicator and does not guarantee whether the perovskite will actually form. To determine that, experimental investigations are necessary, as other factors like kinetics and thermodynamics can also have an impact.

1.3.6.2 Departure from ideality

For an ideal structure, the Goldschmidt factor t is equal to one; for instance, $t = 1.00$ for SrTiO_3 . Experimentally, the perovskite structure is considered stable when $0.88 \leq t \leq 1.05$. This range permits variations in the compositions, especially concerning the cations used. However, this factor is merely a geometric indicator and does not guarantee that a compound with a tolerance factor within this range will adopt a perovskite structure. This is particularly evident in the case of bismuth perovskites: compounds like BiGaO_3 , BiAlO_3 , or BiScO_3 can only be synthesized under pressure, despite having a tolerance factor within the perovskite formation range [61-63]. This can be explained by the assumption that ions are ideal spheres with radii equal to their ionic radii when calculating the Goldschmidt factor. However, for bismuth (III), the presence of a non-bonding ns^2 electron pair invalidates this assumption. When $t < 1$, the B cation fits into the octahedral cavity, while the A cation is smaller than this cavity. This situation can cause the octahedra to rotate, minimizing the A-O distances and allowing the A cation to move out of the center of its cavity. This occurs in BiFeO_3 , where both A and B cations are displaced due to

octahedral rotation. The resulting structures can be either polar or non-polar, which is not ideal for ferroelectricity. For instance, in SrTiO₃, the symmetry of the structure decreases at low temperatures, becoming quadratic below -168 °C with octahedral rotation, resulting in a non-ferroelectric compound [64]. The associated deformation is then purely ferroelastic and not ferroelectric.

I.3.6.3 The ionicity of anion-cation bonds

The difference in electronegativity between the ions significantly influences the stability of the perovskite structure. The ionic nature of this structure can be assessed by the average electronegativity difference, as measured on the Pauling scale.

$$\delta\chi = \frac{\chi_{A-O} + \chi_{B-O}}{2} \quad (\text{I.10})$$

Where: χ_{A-O} and χ_{B-O} represent the differences in electronegativity between A and O, on the one hand, and B and O [65].

I.3.7 The applications of perovskites

In recent years, halide perovskites have become vital materials for various optoelectronic applications. In contrast, oxide perovskites have a much longer history and are crucial in numerous technological applications. Perovskite-based applications are increasingly being adopted in industry, featuring innovative projects such as superconducting materials used in Japan's magnetic levitation trains and electrical cables for urban distribution networks. Healthcare employs perovskite fluorine to measure doses during radiotherapy and to produce X-ray imaging plates. Perovskites are also utilized in sensors, magnetoresistance, transistors, solar cells, and high-voltage capacitors [66-69].

Reference

- [1] Loncle, A. (2022). Nano-imageries synchrotron (Fluorescence X, diffraction X et photoluminescence) appliquées à l'étude du lien entre structure/propriété à l'échelle nanométrique dans les pérovskites hybrides pour le photovoltaïque [Doctoral dissertation, Université Paris-Saclay].
- [2] Smith, W. (1873). Effect of light on selenium during the passage of an electric current. *Nature*, 7(173), 303. <https://doi.org/10.1038/007303a0>.
- [3] Adams, W. G. (1876). On the action of light on tellurium and selenium. *Proceedings of the Royal Society of London*, 24, 163–164.
- [4] Fritts, C. E. (1883). On a new form of selenium cell, and some electrical discoveries made by its use. *American Journal of Science*, 3, 465–472.
- [5] Chapin, D. M., Fuller, C. S., & Pearson, G. L. (1954). A new silicon p-n junction photocell for converting solar radiation into electrical power. *Journal of Applied Physics*, 25(5), 676. <https://doi.org/10.1063/1.1721711>.
- [6] Easton, R. L., & Votaw, M. J. (1959). Vanguard I IGY satellite (1958 beta). *Review of Scientific Instruments*, 30(2), 70–75.
- [7] Judge, D. L., & Coleman, P. J. (1962). Observations of low-frequency hydromagnetic waves in the distant geomagnetic field: Explorer 6. *Journal of Geophysical Research*, 67(13), 5071–5090.
- [8] Alferov, Z. I., Andreev, V. M., Gastev, S. V., Grigoryev, V. M., & Portnoi, E. L. (1971). Solar-energy converters based on pn $\text{Al}_x\text{Ga}_{1-x}\text{As}$ -GaAs heterojunctions. *Soviet Physics – Semiconductors*, 4(12), 2037–2040.
- [9] Leger, P. C., Matijevic, J. R., Maimone, M., & Biesiadecki, J. J. (2005). Mars exploration rover surface operations: Driving Spirit at Gusev Crater. In 2005 IEEE International Conference on Systems, Man and Cybernetics (Vol. 2, pp. 1815–1822). IEEE. <https://doi.org/10.1109/ICSMC.2005.1571395>.

- [10] Kojima, A., Teshima, K., Shirai, Y., & Miyasaka, T. (2009). Organometal halide perovskites as visible-light sensitizers for photovoltaic cells. *Journal of the American Chemical Society*, 131(17), 6050–6051. <https://doi.org/10.1021/ja809598r>
- [11] Li, X., Bi, D., Yi, C., Décoppet, J. D., Luo, J., Zakeeruddin, S. M., & Grätzel, M. (2017). All inorganic halide perovskites nanosystem: Synthesis, structural features, optical properties and optoelectronic applications. *Small*, 13(9), 1603996. <https://doi.org/10.1002/sml.201603996>
- [12] Luque, A., & Hegedus, S. (Eds.). (2011). *Handbook of photovoltaic science and engineering* (2nd ed.). John Wiley & Sons.
- [13] Goucher, F. S., Pearson, G. L., Sparks, M., Teal, G. K., & Shockley, W. (1951). Theory and experiment for a germanium p–n junction. *Physical Review*, 81, 637. <https://doi.org/10.1103/PhysRev.81.637>
- [14] Wenham, S. R., Green, M. A., Watt, M. E., Corkish, R., & Sproul, A. (2013). *Applied photovoltaics* (3rd ed.). Routledge.
- [15] Albert, P. (2020). Développement de cellules multijonctions submillimétriques pour le photovoltaïque à concentration (micro-CPV) et évaluation de leur robustesse [Doctoral dissertation, Université de Bordeaux & Université de Sherbrooke].
- [16] Navarro, J. M. (2008). Cellules photovoltaïques organiques transparentes dans le visible [Doctoral dissertation, Université Toulouse III - Paul Sabatier].
- [17] Ponpon, J.-P. (2007). Détecteurs à semi-conducteurs : Principes et matériaux pour la détection et l'imagerie des rayonnements nucléaires. Éditions Ellipses.
- [18] Shockley, W., & Queisser, H. (2018). Detailed balance limit of efficiency of p–n junction solar cells. In *Renewable energy* (Vol. 2, pp. 35–54). Routledge. (Originally published 1961)
- [19] Thompson, J. R. (2019). Unconventional approaches to structured semiconductors [Doctoral dissertation, California Institute of Technology].
- [20] Park, N.-G., & Segawa, H. (2018). Research direction toward theoretical efficiency in perovskite solar cells. *ACS Photonics*, 5(8), 2970–2977. <https://doi.org/10.1021/acsp Photonics.8b00489>

- [21] Bliss, M., Emery, K., Jones, A., & Kurtz, S. (2019). Interlaboratory comparison of short-circuit current versus irradiance linearity measurements of photovoltaic devices. *Solar Energy*, 182, 256–263. <https://doi.org/10.1016/j.solener.2019.02.054>
- [22] Atomode, D., Johnson, L., O'Connor, R., & Myers, T. (n.d.). Incentivizing rooftop solar energy in Laramie, WY. Unpublished manuscript.
- [23] Photovoltaïque.info. (n.d.). Technologies de cellules solaires photovoltaïques. <https://www.photovoltaïque.info/fr/realiser-une-installation/choix-du-materiel/caracteristiques-des-panneaux-photo-voltaïques/technologies-de-cellules-solaires-photovoltaïques/#tab-content>
- [24] Louwen, A., van Sark, W. G. J. H. M., Faaij, A. P. C., & de Vries, B. J. M. (2016). Re-assessment of net energy production and greenhouse gas emissions avoidance after 40 years of photovoltaics development. *Nature Communications*, 7, Article 13728. <https://doi.org/10.1038/ncomms13728>
- [25] Czochralski, J. (1918). Ein neues Verfahren zur Messung der Kristallisationsgeschwindigkeit der Metalle. *Zeitschrift für Physikalische Chemie*, 92(1), 219–221.
- [26] CultureSciences-Chimie. (n.d.). Les procédés de cristallogénèse, piliers méconnus de la technologie moderne. <https://culturesciences.chimie.ens.fr/thematiques/chimie-des-materiaux/solides-cristal-lins/les-procedes-de-cristallogenese-piliers>
- [27] Futura. (n.d.). Plus minces, les cellules photovoltaïques de deuxième génération. <https://www.futura-sciences.com/planete/dossiers/developpement-durable-cellules-photovoltaïques-coeur-panneaux-solaires-1688/page/8/>
- [28] Bhandari, K. P., Collier, J. M., Ellingson, R. J., & Apul, D. S. (2015). Energy payback time (EPBT) and energy return on energy invested (EROI) of solar photovoltaic systems: A systematic review and meta-analysis. *Renewable and Sustainable Energy Reviews*, 47, 133–141. <https://doi.org/10.1016/j.rser.2015.02.057>
- [29] Taguchi, M., Yano, A., Tohoda, S., Matsuyama, K., Nakamura, Y., Nishiwaki, T., Fujita, K., & Maruyama, E. (2005). Obtaining a higher Voc in HIT cells. *Progress in Photovoltaics: Research and Applications*, 13(6), 481–488. <https://doi.org/10.1002/ppp.612>

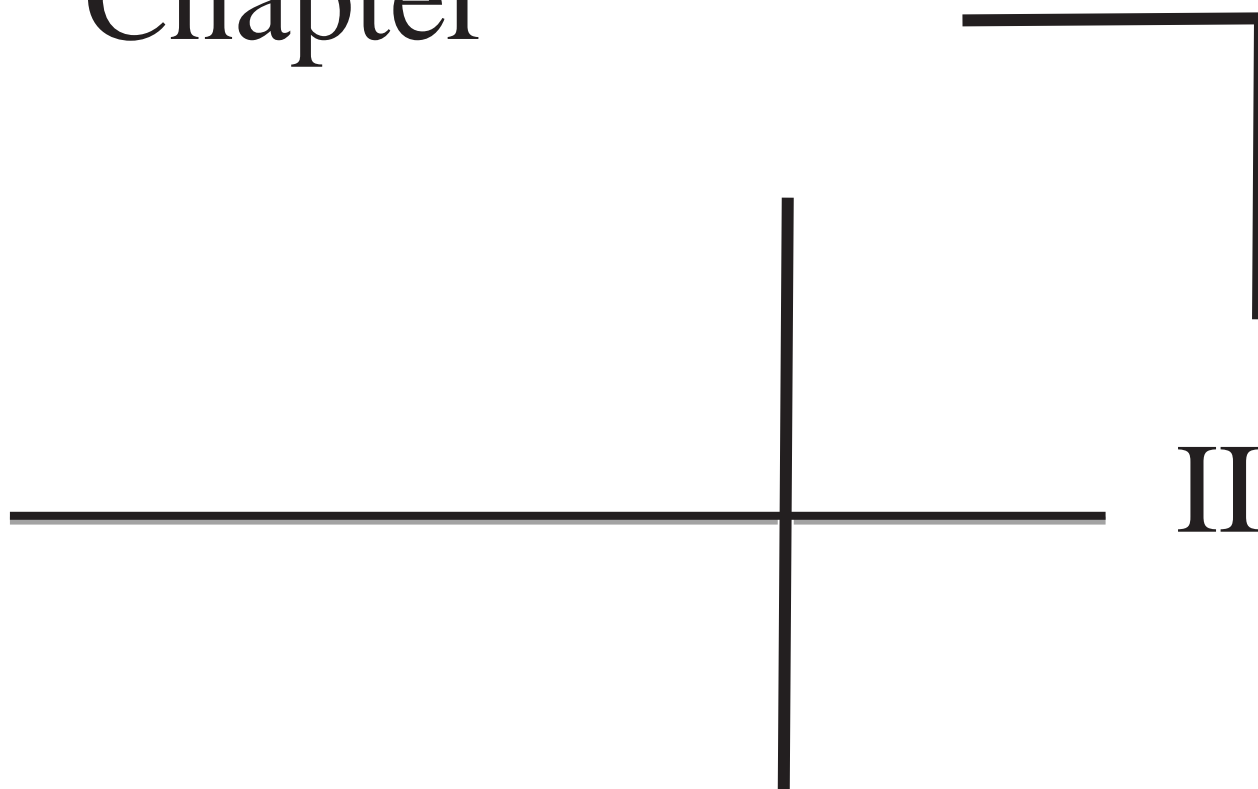
- [30] Google Search. (n.d.). Thin film CdTe photovoltaics and the U.S. energy transition in 2020. <https://www.google.com/search?q=Thin+Film+CdTe+Photovoltaics+and+the+U.S.+Energy+Transition+in+2020>.
- [31] Photovoltaïque.info. (n.d.). Technologies de cellules solaires photovoltaïques. <https://www.photovoltaïque.info/fr/realiser-une-installation/choix-du-materiel/caracteristiques-des-panneaux-photovoltaïques/technologies-de-cellules-solaires-photovoltaïques/#tab-content>
- [32] Destruel, P., & Seguy, I. (2007). Les cellules photovoltaïques organiques. *Reflète de la Physique*, 6, 16–18. <https://doi.org/10.1051/refdp:2007006>
- [33] Froger, V. (2012). Couches minces de chalcogénures de zinc déposées par spray-CVD assisté par rayonnement infrarouge pour des applications photovoltaïques (Doctoral dissertation, École nationale supérieure d'arts et métiers – ENSAM).
- [34] Rose, G. (1839). *De novis quibusdam fossilibus quae in montibus Uraliis inveniuntur*. Typis A.G. Schadii.
- [35] Cohen, R. E., & Krakauer, H. (1992). Electronic structure studies of the differences in ferroelectric behavior of BaTiO₃ and PbTiO₃. *Ferroelectrics*, 136(1), 65–83. <https://doi.org/10.1080/00150199208231305>.
- [36] Lemanov, V. V. (2002). Improper ferroelastic SrTiO₃ and what we know today about its properties. *Ferroelectrics*, 265(1), 1–21. <https://doi.org/10.1080/00150190208224194>
- [37] Itoh, M., Tsuchiya, Y., Imai, M., & Yamaguchi, Y. (1999). Orbital ordering and local magnetic properties of Mott-Hubbard insulators YTiO₃ and LaTiO₃: NMR study. *Journal of the Physical Society of Japan*, 68(8), 2783–2789. <https://doi.org/10.1143/JPSJ.68.2783>
- [38] Sasaki, S., Takéuchi, Y., & Kihara, K. (1987). Orthorhombic perovskite CaTiO₃ and CdTiO₃: Structure and space group. *Acta Crystallographica Section C: Crystal Structure Communications*, 43(9), 1668–1674. <https://doi.org/10.1107/S0108270187097481>
- [39] Goldschmidt, V. M. (1926). Die Gesetze der Krystallochemie. *Naturwissenschaften*, 14, 477–485. <https://doi.org/10.1007/BF01507527>

- [40] Wainer, E. (1946). High titania dielectrics. Transactions of the Electrochemical Society, 89(1), 331–339.
- [41] Aurivillius, B. (1950). Mixed bismuth oxides with layer lattices III. Structure of $\text{BaBi}_4\text{Ti}_4\text{O}_{15}$. Arkiv Kemi, 2, 519–527.
- [42] Wells, H. L. (1893). Über die Cäsium- und Kaliumbleihalogenide. Zeitschrift für Anorganische Chemie, 3, 195–210.
- [43] Møller, C. K. (1958). Crystal structure and photoconductivity of caesium plumbahalides. Nature, 182(4647), 1436. <https://doi.org/10.1038/1821436a0>
- [44] Weber, D. (1978). $\text{CH}_3\text{NH}_3\text{PbX}_3$, ein Pb(II)-System mit kubischer Perowskitstruktur. Zeitschrift für Naturforschung B, 33(12), 1443–1445. <https://doi.org/10.1515/znb-1978-1220>
- [45] Chondroudis, K., & Mitzi, D. B. (1999). Electroluminescence from an organic–inorganic perovskite incorporating a quaterthiophene dye within lead halide perovskite layers. Chemistry of Materials, 11(11), 3028–3030. <https://doi.org/10.1021/cm990511x>
- [46] Wu, T., Wang, J., Li, Y., Chen, H., ... & Zhang, X. (2021). The main progress of perovskite solar cells in 2020–2021. Nano-Micro Letters, 13(1), Article 204. <https://doi.org/10.1007/s40820-021-00702-5>
- [47] Liu, X., Yang, Y., Chen, B., Li, F., ... & Wang, J. (2020). Templated growth of FASnI_3 crystals for efficient tin perovskite solar cells. Energy & Environmental Science, 13(9), 2896–2902. <https://doi.org/10.1039/D0EE00621D>
- [48] Müller, O., & Roy, R. (1974). The major ternary structural families. Springer-Verlag.
- [49] Cocco, A., & Massazza, F. (1963). Microscopic study of the system SrO-TiO_2 . Annali di Chimica, 53, 191–205.
- [50] Chouiah, A. (2019). Étude ab initio des propriétés structurales, optoélectroniques, thermodynamiques et magnétiques des pérovskites [Doctoral dissertation, Université de Mostaganem].
- [51] Aslam, M., Mahmood, T., & Naeem, A. (2021). Organic-inorganic perovskites: A low-cost, efficient photovoltaic material (Vol. 11). IntechOpen. <https://doi.org/10.5772/intechopen.95626>

- [52] Roukos, R. (2015). Transitions de phases dans des oxydes complexes de structure pérovskite : Cas du système $(1-x) \text{Na}_{0.5}\text{Bi}_{0.5}\text{TiO}_3 - x\text{CaTiO}_3$ [Doctoral dissertation, Université de Bourgogne].
- [53] Kennour, S. (2011). Synthèse par technique sol-gel et caractérisation de compositions diélectriques de formulation $(1-x) \text{Na}_{0.5}\text{Bi}_{0.5}\text{TiO}_3 - x\text{BaTiO}_3$ [Doctoral dissertation, Université Mouloud Mammeri de Tizi-Ouzou].
- [54] Mitchell, R. H. (2002). Perovskites: Modern and ancient. Almaz Press.
- [55] Galasso, F. S. (1990). Perovskites and high-Tc superconductors. Gordon & Breach Science Publishers.
- [56] Ben Haj Salah, M. (2019). Pérovskites hybrides bromoplombate luminescentes [Doctoral dissertation, Université d'Angers ; Université de Sfax].
- [57] Sarma, D. D. (2001). A new class of magnetic materials: $\text{Sr}_2\text{FeMoO}_6$ and related compounds. *Current Opinion in Solid State and Materials Science*, 5(4), 261–268. [https://doi.org/10.1016/S1359-0286\(01\)00024-9](https://doi.org/10.1016/S1359-0286(01)00024-9)
- [58] Shannon, R. D., & Prewitt, C. T. (1969). Effective ionic radii in oxides and fluorides. *Acta Crystallographica Section B: Structural Crystallography and Crystal Chemistry*, 25(5), 925–946. <https://doi.org/10.1107/S0567740869003220>
- [59] Shannon, R. D., & Prewitt, C. T. (1970). Revised values of effective ionic radii. *Acta Crystallographica Section B: Structural Crystallography and Crystal Chemistry*, 26(7), 1046–1048. <https://doi.org/10.1107/S0567740870003576>
- [60] Beskow, G. (1924). VM Goldschmidt: Geochemische Verteilungsgesetze der Elemente. *Geologiska Föreningen i Stockholm Förhandlingar*, 46(6–7), 738–743. <https://doi.org/10.1080/11035892409451294>
- [61] Inaguma, Y., Yoshida, M., Katsumata, T., & Itoh, M. (2004). High-pressure synthesis and ferroelectric properties in perovskite-type $\text{BiScO}_3\text{-PbTiO}_3$ solid solution. *Journal of Applied Physics*, 95(1), 231–235. <https://doi.org/10.1063/1.1634359>
- [62] Belik, A. A., et al. (2006). BiScO_3 : Centrosymmetric BiMnO_3 -type oxide. *Journal of the American Chemical Society*, 128(3), 706–707. <https://doi.org/10.1021/ja0567272>

- [63] Belik, A. A., et al. (2006). High-pressure synthesis, crystal structures, and properties of perovskite-like BiAlO_3 and pyroxene-like BiGaO_3 . *Chemistry of Materials*, 18(1), 133–139. <https://doi.org/10.1021/cm051778d>
- [64] Kiat, J. M., & Roisnel, T. (1996). Rietveld analysis of strontium titanate in the Müller state. *Journal of Physics: Condensed Matter*, 8(19), 3471–3476. <https://doi.org/10.1088/0953-8984/8/19/002>
- [65] Sternberg, U., Pietrowski, F., & Priess, W. (1990). The influence of structure and coordination on the ^{31}P chemical shift in phosphates. *Zeitschrift für Physikalische Chemie*, 168(1), 115–128. https://doi.org/10.1524/zpch.1990.168.Part_1.115
- [66] Wang, K., Wang, Y., Yang, X., Li, L., & Wang, Z. (2018). Dark-field sensors based on organometallic halide perovskite microlasers. *Advanced Materials*, 30(32), 1801481. <https://doi.org/10.1002/adma.201801481>
- [67] Raveau, B., Maignan, A., Martin, C., & Hervieu, M. (1998). Colossal magnetoresistance manganite perovskites: Relations between crystal chemistry and properties. *Chemistry of Materials*, 10(10), 2641–2652. <https://doi.org/10.1021/cm9802804>
- [68] Kobayashi, K.-I., Kimura, T., Sawada, H., Terakura, K., & Tokura, Y. (1998). Room-temperature magnetoresistance in an oxide material with an ordered double-perovskite structure. *Nature*, 395(6703), 677–680. <https://doi.org/10.1038/27167>
- [69] Stranks, S. D., & Snaith, H. J. (2015). Metal-halide perovskites for photovoltaic and light-emitting devices. *Nature Nanotechnology*, 10(5), 391–402. <https://doi.org/10.1038/nnano.2015.90>

Chapter



II

Computational Methods

II.1 Introduction

The physical and chemical properties of matter in its atomic, liquid and solid aspects and their understanding can be described by the behavior of its constituents "electron and nucleus" and their interactions. The fundamental theoretical problem in solid state physics is to understand the inner organization of these particles which gives specific properties to the material. The calculation of its properties in the ground state of an N-electron system in a crystal is very difficult, as each particle interacts with all other particles. . The Schrödinger equation (1926) [1] becomes mathematically unsolvable. To overcome this difficult situation it was necessary to seek formalisms other than the traditional wave function to better describe the properties of a system.

In recent years, scientists have developed methods based on theoretical concepts known as the ab-initio methods, which attempt to predict the properties of materials by solving the quantum mechanical equations without using adjustable variables .Among the ab-initio methods, the density functional theory (DFT) [2]. DFT is a mean field method. It therefore proposes to replace the system of N interacting electrons by a fictitious system composed of N independent electrons, interacting with an external potential that was originally developed by Pierre Hohenberg and Walter Kohn in 1964 [3].further, this theory got improved by Kohn and Lu Sham in 1965 [4]. They treated the N-body problem with the single-particle Schrödinger-type equations called the Kohn-Sham equations. Since then, DFT has been very successful in quantum calculations of the electronic structure of matter (atoms, molecules, solids) in both condensed matter physics and quantum chemistry.

II.2 Schrödinger's equation

Solids are made up of an association of elementary particles: nuclei and electrons. The fundamental theoretical problem of solid state physics is to understand the intimate organization of these particles at the origin of their properties [5]. But in this case, classical mechanics proves to be insufficient and it is necessary to call upon quantum mechanics, the basis of which is the resolution of the Schrödinger equation established by Erwin Schrödinger in 1925 and which is written in the following form [6]:

$$\hat{H}_{tot}\Psi(\vec{r}, \vec{R}) = E_{tot}\Psi(\vec{r}, \vec{R}) \quad (\text{II.1})$$

Where:

E_{tot} Denotes the total energy of the system described by $\Psi(\vec{r}, \vec{R})$

$\Psi(\vec{r}, \vec{R})$ Is a function of all electronic and nuclear coordinates, which is time independent.

$\vec{r} = r_1, r_2, \dots, r_n$ Represents the entire set of coordinates of the electrons while $\vec{R} = R_1, R_2, \dots, R_N$ represents the full set of coordinates of the cores.

\hat{H}_{tot} Represents the Hamiltonian operator of the total energy of a many-body system. Its form is expressed as follows:

$$\hat{H} = \hat{T}_e + \hat{T}_N + \hat{V}_{ee} + \hat{V}_{NN} + \hat{V}_{Ne} \quad (\text{II.2})$$

Where \hat{T} and \hat{V} are the operators for kinetic and potential energy, respectively.

The general problem can be expressed as an equation of movement of all particles within the crystal. The exact Hamiltonian of the crystal (non-relativistic) results from the presence of electrostatic interaction forces (repulsion or attraction) depending on the charge of the particles (nucleus, electron) [6].

$$\hat{T} = \hat{T}_e + \hat{T}_N \quad (\text{II.3})$$

$$\hat{V} = \hat{V}_{ee} + \hat{V}_{NN} + \hat{V}_{Ne} \quad (\text{II.4})$$

\hat{H} is a non-relativistic differential operator including all forms of energy [6]:

The electron kinetic energy operator $\hat{T}_e(\vec{r})$:

$$\hat{T}_e(\vec{r}) = -\frac{\hbar^2}{2m} \sum_i^n \nabla_i^2$$

The kinetic energy operator of nuclei $\hat{T}_N(\vec{R})$:

$$\hat{T}_N(\vec{R}) = -\frac{\hbar^2}{2M} \sum_I^N \nabla_I^2$$

Potential energy operator of the coulombic interaction of repulsion between electron and electron $\hat{V}_{ee}(\vec{r})$:

$$\hat{V}_{ee}(\vec{r}) = \frac{e^2}{4\pi\epsilon_0} \sum_{i=1}^n \sum_{j>i}^n \frac{1}{|\vec{r}_i - \vec{r}_j|}$$

Operator of the potential energy of coulombic interaction of attraction between nucleus and electron $\hat{V}_{eN}(\vec{r}, \vec{R})$:

$$\hat{V}_{eN}(\vec{r}, \vec{R}) = -\frac{e^2}{4\pi\epsilon_0} \sum_{i=1}^n \sum_{I=1}^N \frac{Z_I}{|\vec{r}_i - \vec{R}_I|}$$

Operator of the potential energy of the coulombic repulsion interaction between nucleus and nucleus $\hat{V}_{NN}(\vec{R})$:

$$\hat{V}_{NN}(\vec{R}) = \frac{e^2}{4\pi\epsilon_0} \sum_{I=1}^N \sum_{J>I}^N \frac{Z_I Z_J}{|\vec{R}_I - \vec{R}_J|}$$

Thus, the global Hamiltonian becomes:

$$\hat{\mathbf{H}}_T = -\frac{\hbar^2}{2} \sum_i \frac{\nabla^2 \vec{R}_i}{M_n} - \frac{\hbar^2}{2} \sum_i \frac{\nabla^2 \vec{r}_i}{m_e} - \frac{1}{4\pi\epsilon_0} \sum_{i,j} \frac{e^2 Z_i}{|\vec{R}_i - \vec{r}_j|} + \frac{1}{8\pi\epsilon_0} \sum_{i \neq j} \frac{e^2}{|\vec{r}_i - \vec{r}_j|} + \frac{1}{8\pi\epsilon_0} \sum_{i \neq j} \frac{e^2 Z_i Z_j}{|\vec{R}_i - \vec{R}_j|} \quad (\text{II.5})$$

The calculation of the ground state energy of the system is analytically very difficult for most systems. Nevertheless, current mathematical knowledge does not yet allow the solution of equation. Knowing that with three interacting bodies it is impossible to solve this equation exactly, therefore numerous approximations have been developed to overcome this obstacle.

II.3 Fundamental approximations

II.3.1 The Born-Oppenheimer approximation

It consists in separating the movement of the electrons from that of the nuclei [7]. Considering the large difference in mass between electrons and nuclei, the latter can be considered as fixed compared to electrons. So the electrons move quite a bit faster than the atomic nuclei. According to Born and Oppenheimer [8], electrons are always in their ground state, regardless of the position of the atomic nuclei. This approximation simplifies the Schrödinger equation, the kinetic energy terms of the nuclei and the nucleus-nucleus interactions, independent of the electrons, cancel each other out. The problem to be solved now is therefore a system of Ne electrons interacting in an external potential generated by the nuclei. The interaction term between the nuclei is only involved in the calculation of the total energy of the system, but not in the calculation of the electronic wave functions.

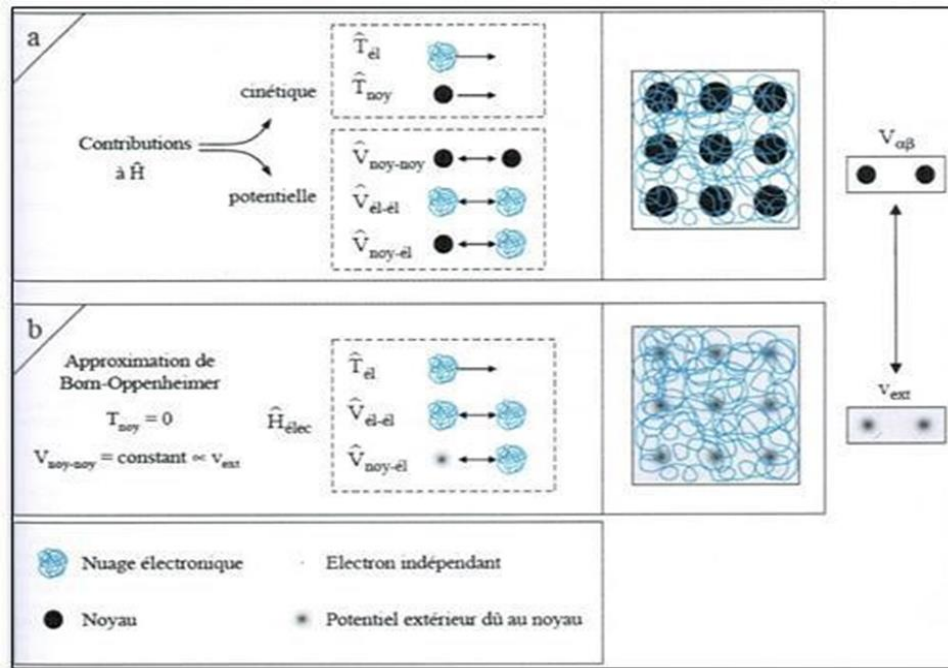


Figure II.1: Transition from a problem with n electrons and N nuclei to one with n electrons.

The Hamiltonian can thus be defined as:

$$\hat{H}_{tot} = \hat{T}_e + \hat{V}_{ee} + \hat{V}_{eN} \quad (\text{II.6})$$

Or:

$$\hat{H}_T = -\frac{\hbar^2}{2} \sum_i \frac{\nabla^2 \vec{r}_i}{m_e} - \frac{1}{4\pi\epsilon_0} \sum_{i,j} \frac{e^2 Z_i}{|\vec{R}_i - \vec{r}_j|} + \frac{1}{8\pi\epsilon_0} \sum_{i \neq j} \frac{e^2}{|\vec{r}_i - \vec{r}_j|} \quad (\text{II.7})$$

The Born-Oppenheimer approximation is called adiabatic [2] because it separates the electronic problem from the lattice vibration problem.

Despite this reduction, the Schrödinger equation remains difficult to solve. The new total wave function of the system depends on the coordinates of all the electrons and cannot be decoupled therefore the problem cannot be solved especially using current computer resources. Therefore, further approximations are necessary.

II.3.2 Hartree-Fock approximation

In 1930 Fock [9] showed that Hartree [10] solutions infringe the Pauli Exclusion Principle as they are not antisymmetric with respect to the exchange of two random electrons. The anti-metrisation of the electronic wave function is written, for example, as follows:

$$\Phi(\vec{r}_1, \vec{r}_2, \dots, \vec{r}_i, \vec{r}_{i+1}, \dots, \vec{r}_j, \vec{r}_{N_e}) = -\Phi(\vec{r}_1, \vec{r}_2, \dots, \vec{r}_i, \vec{r}_{i+1}, \dots, \vec{r}_j, \vec{r}_{N_e}) \quad (\text{II.8})$$

Such a description obeys the Pauli Exclusion Principle, stating that two electrons of the same quantum number cannot simultaneously occupy the same quantum state. However, in the

Hartree formulation of the wave function, this is not the case, as the electron i occupies precisely the state i .

Hartree and Fock generalized this concept by showing that Pauli's principle is respected if we write the wave function [11] as a: *<Slater's determinant>* [12]

$$\Phi(\vec{r}_1\vec{\sigma}_1, \vec{r}_2\vec{\sigma}_2, \dots, \vec{r}_{N_e}\vec{\sigma}_{N_e}) = \frac{1}{\sqrt{N_e!}} \begin{vmatrix} \Phi_1(\vec{r}_1\vec{\sigma}_1) & \Phi_1(\vec{r}_2\vec{\sigma}_2) & \dots & \Phi_1(\vec{r}_{N_e}\vec{\sigma}_{N_e}) \\ \Phi_2(\vec{r}_1\vec{\sigma}_1) & \Phi_2(\vec{r}_2\vec{\sigma}_2) & \dots & \Phi_2(\vec{r}_{N_e}\vec{\sigma}_{N_e}) \\ \dots & \dots & \dots & \dots \\ \Phi_{N_e}(\vec{r}_1\vec{\sigma}_1) & \Phi_{N_e}(\vec{r}_2\vec{\sigma}_2) & \dots & \Phi_{N_e}(\vec{r}_{N_e}\vec{\sigma}_{N_e}) \end{vmatrix} \quad (\text{II.9})$$

Where $\vec{\sigma}$ is the spin.

The function Φ given by equation leads to the Hartree-Fock equations for a one-particle system:

$$\left(-\frac{1}{2}\Delta_i + V_{ext}(\vec{r}) + \sum_{j=1}^{N_e} \int d^3\vec{r}' \frac{|\Phi_j(\vec{r}')|^2}{|\vec{r}-\vec{r}'|} \right) \Phi_i(\vec{r}) - \sum_{j=1}^{N_e} \delta_{\sigma_i\sigma_j} \int d^3\vec{r}' \frac{\Phi_j^*(\vec{r}')\Phi_i(\vec{r}')}{|\vec{r}-\vec{r}'|} \Phi_i(\vec{r}) = \epsilon_i \Phi_i(\vec{r})$$

(II.10)

These Hartree-Fock equations are difficult to solve when the system under study has a large number of electrons.

Electron-electron interactions produce additional energy terms in addition to those of the Hartree approximation which are called Wigner correlation energy terms.

II.4 Density functional theory (DFT)

Density functional theory constitutes another alternative to the formulation of the N-body problem. Its origin dates back to the pioneering works of Thomas [13] and Fermi [14]. They postulated that the electronic properties of an interacting electron system can be described in terms of an electronic density function. However, it was not until 1964 that Hohenberg and Kohn [15] provided the first truly rigorous formulation of density functional theory.

II.4.1 Thomas and Fermi's approach

In the model of Thomas [13] and Fermi [14], a system with a non-uniform but slowly varying electron density is subdivided into small regions in phase space. In each cell, the electrons behave identically, evolving into an effective potential V_{eff} given by the following equation:

$$\mathbf{V}_x(\vec{r}) = \mathbf{V}_{ext}(\vec{r}) + \int d\vec{r}' \frac{\rho(\vec{r}')}{|\vec{r}-\vec{r}'|} \quad (\text{II.11})$$

The Thomas and Fermi model is a primitive theory of the density functional because the contributions to the total electronic energy are expressed solely as a function of the electronic density:

$$\mathbf{E}_{TF}[\rho(\vec{r})] = \frac{3}{5} (3\pi^2)^{3/2} \int d\vec{r} \rho^{5/2}(\vec{r}) + \int d\vec{r} V_{ext}(\vec{r})\rho(\vec{r}) + \frac{1}{2} \iint d\vec{r} d\vec{r}' \frac{\rho(\vec{r})\rho(\vec{r}')}{|\vec{r}-\vec{r}'|} \quad (\text{II.12})$$

The first term represents the kinetic energy of a system of electrons without density interaction $\rho(\vec{r})$; the second term describes the energy of an electric density in an external electrostatic potential V_{ext} . Finally, the third term corresponds to the energy of coulombic electron-electron interaction.

The Thomas-Fermi model introduces an incorrect function for kinetic energy. Moreover, this model, in its original version, does not account for exchange and correlation effects. However, it has the merit of bringing forth an original idea, which in 1964 gave rise to the current density functional theory.

II.4.2 Theorems of Hohenberg and Kohn

II.4.2.1 First theorem of Hohenberg and Kohn: proof that $E=E(\rho)$

For a system with N electrons, the external potential $V_{\text{ext}}(\mathbf{r})$ completely determines the Hamiltonian H_{elec} . This means that if we know the number of electrons N in the system as well as the external potential $V_{\text{ext}}(\mathbf{r})$, we can uniquely determine the Hamiltonian and thus access the energy and the wavefunction of the ground state. Therefore, the external potential perfectly reflects the various characteristics of a compound. Hence, there are two ways to consider an atomic system:

- ❖ Through the nuclei via the external potential.
- ❖ Through its electron cloud via electron density.

One seems to be the image of the other, so a close relationship between these two quantities becomes very clear.

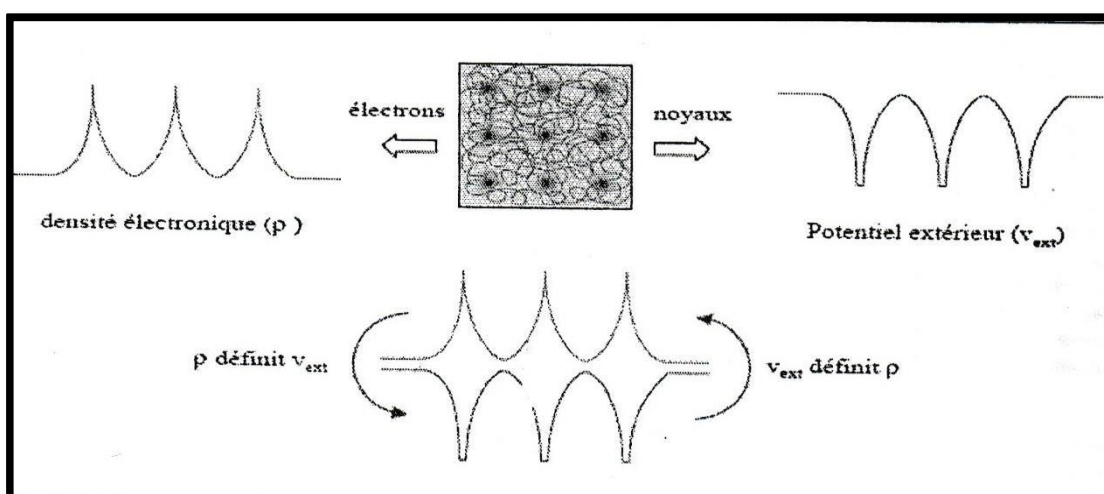


Figure II.2: Illustration of the first Hohenberg-Kohn theorem

The first Hohenberg-Kohn theorem provides a theoretical justification for the idea that a given electron density corresponds to a unique external potential. The potential $V_{\text{ext}}(\mathbf{r})$ is indeed determined, up to a constant, by the electron density $\rho(\mathbf{r})$. The electron density $\rho(\mathbf{r})$ also uniquely determines the wave function and all the electronic properties of the system. Therefore, the total energy of the system is a function of the density $\rho(\mathbf{r})$.

$$E = E[\rho(\mathbf{r})] \quad (\text{II.13})$$

By separating the dependent parts of the system (N) from those that are not, we obtain:

$$E[\rho(\mathbf{r})] = T_{\text{el}}[\rho(\mathbf{r})] + V_{\text{el-el}}[\rho(\mathbf{r})] + T_{\text{noy-el}}[\rho(\mathbf{r})] = F_{\text{HK}}[\rho(\mathbf{r})] + \int \rho(\mathbf{r})V_{\text{ext}}(\mathbf{r})d\mathbf{r} \quad (\text{II.14})$$

$$\text{or :} \quad F_{\text{HK}}[\rho(\mathbf{r})] = T_{\text{el}}[\rho(\mathbf{r})] + V_{\text{el-el}}[\rho(\mathbf{r})] \quad (\text{II.15})$$

The system's independent terms are then grouped together in a so-called Hohenberg-Kohn functional.

II.4.2.2 Second Hohenberg-Kohn theorem: variational principle

The ground state density is, in principle, sufficient to obtain all the interesting properties of an electronic system. But how can we be sure that a given density is one of the sought-after ground states? Hohenberg and Kohn answer this question through their second theorem, stated as follows:

For an external potential V_{ext} , the energy $E[\rho_{\text{test}}]$, associated with any trial density that satisfies the necessary boundary conditions:

$$\rho_{\text{test}} \geq 0 \quad (\text{II.16})$$

$$\int \rho_{\text{test}}(\mathbf{r})d\mathbf{r} = N(\mathbf{r}) \quad (\text{II.17})$$

The energy $E[\rho_{\text{test}}]$ is greater than or equal to the energy associated with the ground state electron density $E[\rho_{\text{fond}}]$.

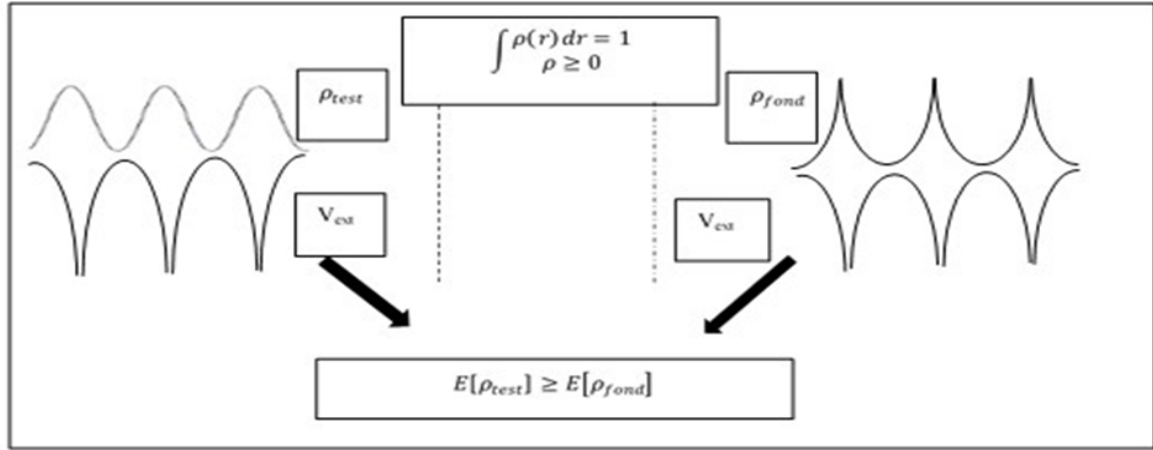


Figure II.3: Illustration of the second Hohenberg-Kohn theorem

This theorem is nothing other than the variational principle expressed for functional energies of a density, $E[\rho]$ and not of a wave function $E[\Psi]$. Now, according to the first theorem, a test density defines its own Hamiltonian and likewise its own test wave function. Hence, we can have a correspondence between the variational principle in its wave function version and in its electron density version such as:

$$\langle \Psi_{test} | \hat{H} | \Psi_{test} \rangle = E[\rho_{test}] \geq E[\rho_{fond}] = \langle \Psi_{fond} | \hat{H} | \Psi_{fond} \rangle \quad (\text{II.18})$$

II.4.3 The Kohn and Sham equations

Kohn and Sham [KS] [8] wrote the exact ground state energy of an interacting system in an external potential V_{ext} as a functional depending only on the electron density $\rho(\vec{r})$.

$$E[\rho(\mathbf{r})] = T_S[\rho(\mathbf{r})] + \int d^3\mathbf{r} V_{ext} \rho(\mathbf{r}) + \int d^3\mathbf{r} d^3\mathbf{r}' \frac{\rho(\mathbf{r})\rho(\mathbf{r}')}{|\mathbf{r}-\mathbf{r}'|} + E_{XC}[\rho(\mathbf{r})] \quad (\text{II.19})$$

In this case Kohn and Sham propose to solve the following system of self-consistent equations which allows to find the density $\rho(\vec{r})$, that minimizes the energy of the system

$$\begin{cases} H_{ks} \Phi_i(\mathbf{r}) = \left[-\frac{1}{2} \Delta_i + V_{eff}(\mathbf{r}) \right] \Phi_i(\mathbf{r}) = \epsilon_i^{ks} \Phi_i(\mathbf{r}) \\ \rho(\mathbf{r}) = \sum_{i=1}^{N_e} f_i |\Phi_i(\mathbf{r})|^2 \end{cases} \quad (\text{II.20})$$

ϵ_i^{ks} and $\Phi_i(\vec{r})$ being respectively the eigenvalues and the mono-electronic (so-called Kohn-Sham) eigenwave functions from which we determine the electron density.

$\rho(\vec{r}), V_{eff}$ is the effective potential in which the particles move:

$$V_{\text{eff}}(\mathbf{r}) = V_{\text{ext}}(\mathbf{r}) + V_{\text{H}}(\mathbf{r}) + V_{\text{xc}}(\mathbf{r}) \quad (\text{II.21})$$

Where we put:
$$V_{\text{H}}(\mathbf{r}) = \int d^3\mathbf{r}' \frac{\rho(\mathbf{r}')}{|\mathbf{r}-\mathbf{r}'|} \quad \text{et} \quad V_{\text{xc}}(\mathbf{r}) = \frac{\delta E_{\text{xc}}[\rho(\mathbf{r})]}{\delta \rho(\mathbf{r})} \quad (\text{II.22})$$

By replacing the kinetic energy and electron density in equation (II.19) with those found by solving the system (II.19) we find the total energy of the ground state of the system:

$$E[\rho] = \sum_{i=1}^{Ne} \varepsilon_i - \int d^3\mathbf{r} d^3\mathbf{r}' \frac{\rho(\mathbf{r})\rho(\mathbf{r}')}{|\mathbf{r}-\mathbf{r}'|} - \int d^3\mathbf{r} V_{\text{xc}}(\mathbf{r})\rho(\mathbf{r}) + E_{\text{xc}}[\rho] \quad (\text{II.23})$$

We note that the Kohn-Sham transformations are exact transformations. The problem of N_e interacting electrons is replaced by N_e independent electrons interacting with the total electron density, which simplifies the calculations considerably.

In the Kohn-Sham formulation, all the energy terms, and their associated potentials, can be evaluated, except the exchange-correlation term, which is problematic. This term $E_{\text{xc}}[\rho]$ is not known exactly even though it appears as a corrective term. In any case, various approximations have to be used, which we will discuss next.

II.5 Resolution of exchange and correlation energy

Gradually, the unknown part in the functional $E[\rho]$ was reduced to a universal functional F_{HK} and finally to an exchange and correlation energy $E_{\text{xc}}[\rho]$. It is therefore necessary to approximate the expression of this exchange and correlation functional $E_{\text{xc}}[\rho]$, so that it offers as accurate a description of the system as possible. The exchange part accounts for the coulombic energy gain due to compliance with Pauli's principle, while the correlation corresponds to the right balance between coulombic energy gain and kinetic energy cost when two electrons of different spin states are separated.

II.5.1 The local density approximation (LDA)

To approximate the density functional $E_{\text{xc}}[\rho(\mathbf{r})]$, Kohn and Sham proposed as early as 1965 the local density approximation (LDA) [16], which treats an inhomogeneous system as locally homogeneous, with exchange and correlation energy known exactly:

$$E[\rho(\mathbf{r})] = \int \rho(\mathbf{r}) \varepsilon[\rho(\mathbf{r})] d^3\mathbf{r} \quad (\text{II.24})$$

Where $\varepsilon[\rho(\mathbf{r})]$ is the exchange and correlation energy per particle of a uniform electronic gas of density ρ that is known to be in the form:

$$V_{\text{xc}}(\mathbf{r}) = \frac{\delta E_{\text{xc}}[\rho(\mathbf{r})]}{\delta \rho(\mathbf{r})} = \varepsilon[\rho(\mathbf{r})] + \rho(\mathbf{r}) \frac{\delta \varepsilon_{\text{xc}}[\rho(\mathbf{r})]}{\delta \rho(\mathbf{r})} \quad (\text{II.25})$$

In the case of magnetic materials, the electron spin provides an additional degree of freedom and the LDA must then be extended to the Spin Density Approximation [16]. and the LDA must then

be extended to the Local Spin Density Approximation (LSDA) where the exchange and correlation energy E_{XC} becomes a functional of the two high and low spin densities:

$$E_{XC}[\rho \downarrow \cdot \rho \uparrow] = \int \rho(\mathbf{r}) \varepsilon[\rho \downarrow \cdot \rho \uparrow] d^3\mathbf{r} \quad (\text{II.26})$$

The most commonly used forms for energy and exchange potential in LDA are those of Kohn-Sham and Wigner [17], Von Barth-Hedin [16], Gunnarson-Lundqvist [18], Vosko et al. [19] and Perdew and Wang [20].

Table. I.1: Computational performance in the LDA approximation [11].

Quantity	LDA error
Bond length	~1%
Vibration frequency	Some %
Elastic constant	Some %
Cohesive energy	~15%
Energy barrier	~20%

II.5.2 LDA+U approximation

By its construction, it is clear that LDA correctly handles correlation effects for systems with almost homogeneous electron density, such as alkali metals. This is not the case for compounds such as Mott insulators, transition metal oxides, and rare earth oxides, for which the LDA is inadequate. LDA does not take into account correlation effects in partially filled 3d (transition metal) and 4f (rare earth) layers. In these systems, a modification of the LDA is necessary. This is achieved by adding the Hubbard-type coulombic interaction to the LDA functionals. This term is added to the exchange-correlation potential of the electrons in the incomplete d and f layers. The Hubbard model is one of the most widespread models in the physics of strongly correlated electrons. It probably provides the simplest quantum description that includes both the movement of electrons and their mutual interactions on the lattice. Despite this structural simplicity, exact results are known only under very particular conditions, for example, in one

dimension [21]. Since its introduction by Hubbard to the present day, this term represents a robust model for the research of new many-body methods. Therefore, we need to explain the connection between the electronic problem in a realistic solid and the Hubbard model.

This Hubbard parameter [22, 23] is added to the Kohn-Sham Hamiltonian:

$$\mathbf{E}_U = \frac{U}{2} \sum_{i \neq j} \mathbf{n}_i \mathbf{n}_j \quad (\text{II.27})$$

\mathbf{E}_U : added to the DFT exchange and correlation E_{xc} term.

\mathbf{n}_i : The number of orbital occupancies $i = \{m_i, \sigma\}$ in state l .

Originally known as LDA+U, this method was developed to account for the insulating properties of Mott insulators.

II.5.3 Generalized Gradient Approximation (GGA)

In several cases the (LDA) [24] gave reliable results, but in others it was less accurate with the experimental results. Most of the corrections that have been introduced to the LDA are based on the idea of taking into account local variations in density. For this reason the gradient of the electron density has been introduced leading to the generalized gradient approximation GGA [20], in which the exchange and correlation energy is a function of the electron density and its gradient: [25]

$$E_{XC}^{GGA} = \int \mathbf{n}(\mathbf{r}) \varepsilon_{XC}[\mathbf{n}, |\nabla \mathbf{n}|, \dots] d^3r \equiv \int \mathbf{n}(\mathbf{r}) \varepsilon_X^{hom}(\mathbf{n}) F_{XC}[\mathbf{n}, |\nabla \mathbf{n}|, \dots] d^3r \quad (\text{II.28})$$

Where ε_X^{hom} is the exchange energy of a non-polarized system of density $\mathbf{n}(\mathbf{r})$. There are many forms of F_{XC} , the most commonly used are those introduced by Becke [26], Perdew and Wang [20] and Perdew, Burke and Ernzerhof [27].

II.5.4 The EV-GGA approximation

The major shortcoming in both approximations (GGA and LDA) is the estimation of the energy gap value, which is essentially due to the correlation term being considered too simple. To correct this shortcoming, Engel and Vosko [28] have shown that the GGA cannot improve on the second-order expansion of the generalized gradient due, most of the time, to the cancellation of local errors, hence the correction brought to the correlation term by mixing the second-order generalized gradient with the exact Hartree-Fock correlation term. But unfortunately, it remains poor if one is interested in calculations of the fundamental energy as a function of the structural parameters [29].

II.5.5 Modified Becke and Johnson potential (mBJ)

A new version of the exchange potential, first proposed by Becke and Johnson [30], was published by Tran and Blaha [31]. This is the mBJ "modified Becke Johnson Potential" (also

known as the TB potential: Tran-Blaha) which has been implemented in the latest versions of the ab initio Wien2k code. Tran and Blaha [32] tested the exchange potential proposed by Becke and Johnson (BJ) [33] which was designed to reproduce the shape of the exact exchange potential called the "optimised effective potential (OEP)". They noted that using the BJ potential combined with the GGA correlation potential always gives underestimated gap energies. In order to improve these results, Tran and Blaha [31] introduced a simple modification of the original BJ potential and obtained good agreement with other more expensive approaches (due to their high self-consistency) such as hybrid functional and the GW method [33-35]. The modified BJ potential (mBJ) proposed by Tran and Blaha [31] has the following form:

$$v_{x,\sigma}^{mBJ}(\mathbf{r}) = cv_{x,\sigma}^{BR}(\mathbf{r}) + (3c - 2) \frac{1}{\pi} \sqrt{\frac{5}{12}} \sqrt{\frac{2t_{\sigma}(\mathbf{r})}{\rho_{\sigma}(\mathbf{r})}} \quad (\text{II.29})$$

$\rho_{\sigma}(\mathbf{r}) = \sum_{i=1}^{n_{\sigma}} |\psi_{i,\sigma}(\mathbf{r})|^2$ is the density of electrons.

$t_{\sigma}(\mathbf{r}) = \frac{1}{2} \sum_{i=1}^{n_{\sigma}} \nabla \psi_{i,\sigma}^*(\mathbf{r}) \nabla \psi_{i,\sigma}(\mathbf{r})$ is the density of the kinetic energy.

$$v_{x,\sigma}^{mBJ}(\mathbf{r}) = -\frac{1}{b_{\sigma}(\mathbf{r})} \left(1 - e^{-x_{\sigma}(\mathbf{r})} - \frac{1}{2} x_{\sigma}(\mathbf{r}) e^{x_{\sigma}(\mathbf{r})} \right) \quad (\text{II.30})$$

$v_{x,\sigma}^{mBJ}$ is the Becke-Roussel (BR) potential [36] which has been proposed to model the coulombic potential created by the exchange hole.

The term x_{σ} was determined from $\rho_{\sigma}(\mathbf{r})$, $\nabla \rho_{\sigma}(\mathbf{r})$, $\nabla^2 \rho_{\sigma}(\mathbf{r})$ et \mathbf{r} ; while the term \mathbf{r} was calculated using the following relationship:

$$b_{\sigma}(\mathbf{r}) = \left[\frac{x_{\sigma}^3 e^{-x_{\sigma}}}{8\pi\rho_{\sigma}} \right]^{\frac{1}{3}} \quad (\text{II.31})$$

In equation (II.31), c has been chosen to depend linearly on the square root of the mean of $\frac{\nabla \rho_{\sigma}(\mathbf{r})}{\rho_{\sigma}(\mathbf{r})}$

$$c = \alpha + \beta \left(\frac{1}{V_{cell}} \int_{cell} \frac{|\nabla \rho(\mathbf{r}')|}{\rho(\mathbf{r}')} d^3 \mathbf{r}' \right)^{\frac{1}{2}} \quad (\text{II.32})$$

α and β are adjustable parameters ($\alpha = -0.012$ (dimensionless) and ($\beta = 1.023 \text{ bohr}^{-1/2}$) and V_{cell} is the volume of the unit mesh. For $c=1$, we have the reproduction of the original Beck and Johnson potential.

$$v_{x,\sigma}^{BJ}(\mathbf{r}) = v_{x,\sigma}^{BR}(\mathbf{r}) + \frac{1}{\pi} \sqrt{\frac{5}{12}} \sqrt{\frac{2t_{\sigma}(\mathbf{r})}{\rho_{\sigma}(\mathbf{r})}} \quad (\text{II.33})$$

By varying c for a given material, it was found that for many solids the gap energy increases monotonically with respect to c [31]. Specifically, for solids with small gaps c_{opt} (the value of c that leads to perfect agreement with the experiment) ranges from 1.1 to 1.3 while for solids with larger gaps, c_{opt} is larger (its value varies from 1.4 to 1.7) [32].

II.5.6 Hybrid functions

Nous présentons dans ce paragraphe un autre type de fonctionnelles, les fonctionnelles hybrides, qui connaissent déjà un succès remarquable. Leur recette, suggéré initialement par Becke [37], réside dans la prise en compte, dans E_{XC} , d'une fraction d'échange exact Hartree-Fock. La contribution d'échange s'avère en effet nettement plus importante en valeur absolue que celle des effets de corrélation : puisque l'on connaît l'expression exacte de l'énergie d'échange, il est tentant de l'utiliser pour la partie échange de $E_{\text{XC}}[n]$ à la place d'une fonctionnelle approchée dépendant explicitement de la densité. La justification théorique de ce point provient de la relation dite de connections adiabatique : introduisant un paramètre $\lambda \in [0; 1]$ and defining the intensity of the interaction between the electron and itself, it is possible to write the exchange-correlation energy as :

$$E_{\text{XC}}[n] = \int_0^1 U_{\text{ncl}}^\lambda d\lambda \quad (\text{II.34})$$

Where the integrand U_{ncl}^λ represents the set of non-classical contributions to the total energy. Note that U_{ncl}^λ corresponds to a potential energy only, with the kinetic part of the exchange-correlation energy coming from the integration over λ .

II.6 The linearized augmented plane wave method (FP-LAPW)

There are several methods for calculating the properties of solids, and what they have in common is the self-consistent solution of the Kohn and Sham equation. This is the origin of several numerical methods. The Full Potential Linearized Augmented Plane Wave (FP-LAPW) method, which saves several orders of magnitude in computation time, will be presented in the following paragraphs.

II.6.1 The APW method

Slater [38] proposed the augmented plane wave functions (APW) as a basis for solving the one-electron Schrödinger equation, which corresponds to the DFT-based equation of Kohn and Sham. The APW method is based on the Muffin-Tin (MT) approximation to describe the crystal potential. According to this approximation the unit cell is divided into two types of regions: spheres called "Muffin-Tin" (I) which do not overlap and are centered on each atom α of radius R_α and interstitial regions (II) (the empty space). As a consequence, the wave functions of the

crystal are developed in different bases depending on the region considered: radial solutions multiplied by spherical harmonics in the MT spheres and plane waves in the interstitial region.

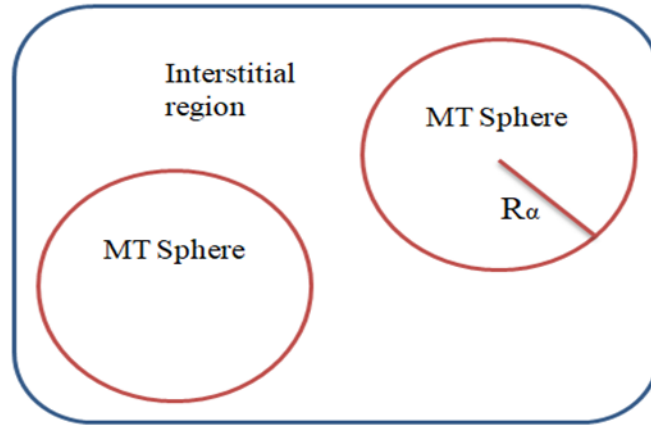


Figure II.4: Muffin-Tin" potential

Thus the wave function is of the form:

$$\varphi(\mathbf{r}) = \begin{cases} \sum_{lm} A_{lm} U_l(\mathbf{r}) Y_{lm}(\mathbf{r}) & \mathbf{r} \in \text{I} \\ \frac{1}{\Omega^2} \sum_{\mathbf{G}} C_{\mathbf{G}} e^{i(\mathbf{G}+\mathbf{K})\mathbf{r}} & \mathbf{r} \in \text{II} \end{cases} \quad (\text{II.35})$$

Where A_{lm} and $C_{\mathbf{G}}$ are the expansion coefficients, Ω is the volume of the unit cell. $U_l(\mathbf{r})$ is the radial solution of the Schrödinger equation which is written as :

$$\left(-\frac{\partial^2}{\partial r^2} + \frac{l(l+1)}{r^2} + V(r) - E_l \right) r U_l(r) = 0 \quad (\text{II.36})$$

Where E_l is the linearization energy and $V(\mathbf{r})$ the spherical component of the potential in the sphere.

The radial functions defined by equation are automatically orthogonal to any state of the same Hamiltonian that vanishes at the boundary of the sphere as the following equation shows:

$$(E_2 - E_1) r U_1 U_2 = U_2 \frac{d^2 r U_1}{dr^2} - U_1 \frac{d^2 r U_2}{dr^2} \quad (\text{II.37})$$

Where U_1 and U_2 are radial solutions for the energies E_1 and E_2 . The overlap being constructed by using equation and integrating it by parts.

Slater justifies the particular choice of these functions by noting that plane waves are solutions of the Schrödinger equation when the potential is constant. As for the radial functions, they are solutions in the case of a spherical potential, when E_l is an eigenvalue.

This approximation is very good for materials with a face-centered cubic structure, and less and less satisfying as the material's symmetry decreases.

However, to ensure continuity at the sphere boundaries in the APW method, the A_{lm} have been defined in terms of the C_G coefficients of the existing plane waves in the interstitial regions. These coefficients are thus expressed by the following expression:

$$A_{lm} = \frac{4\pi i^l}{\Omega^{1/2} U_l(R_\alpha)} \sum_G C_G j_l(|K + g|R_\alpha) Y_{lm}^*(K + G) \quad (\text{II.38})$$

R_α is the radius of the sphere, and the origin is taken as the centre of the sphere.

Thus the A_{lm} are determined by the plane wave coefficients C_G and the energy parameters E_l , as these are variational in the APW method. The individual functions which are represented by the index G and which consist of plane waves in the interstitial plane waves in the interstitial region and radial functions in the spheres are called augmented plane waves (APW).

The APW method, thus constructed, presents some difficulties related to the function $U_l(R_\alpha)$ which appears in the denominator of the equation. Indeed, depending on the value of the parameter E_l , the value of $U_l(R)$ can become nil at the surface of the MT sphere, leading to a separation of the radial functions from the plane wave functions. In order to overcome this problem, several modifications to the APW method have been made, including those proposed by Andersen [39].

II.6.2 Principle of the FP-LAPW method

In this method, the basic functions inside the sphere are linear combinations of the radial functions $U_l(\mathbf{r})Y_{lm}(\mathbf{r})$ and their derivatives $\dot{U}_l(\mathbf{r})Y_{lm}(\mathbf{r})$ with respect to energy.

The functions $U_l(\mathbf{r})$ are defined as in the APW method, and the function $\dot{U}_l(\mathbf{r})Y_{lm}(\mathbf{r})$ must satisfy the following condition [39]:

$$\left\{ -\frac{d^2}{dr^2} + \frac{l(l+1)}{r^2} + V(r) - E_l \right\} r \dot{U}_l(r) = r U_l(r) \quad (\text{II.39})$$

The wave function is written as follows:

$$\Phi(\mathbf{r}) = \begin{cases} \sum_{lm} [A_{lm} U_l(\mathbf{r}) B_{lm} \dot{U}_l(\mathbf{r})] Y_{lm} & \mathbf{r} < \mathbf{r}_0 \\ \frac{1}{\sqrt{\Omega}} \sum_G C_G e^{i(\mathbf{k}+\mathbf{G})\mathbf{r}} & \mathbf{r} > \mathbf{r}_0 \end{cases} \quad (\text{II.40})$$

Where A_{lm} : are coefficients corresponding to the function $U_l(\mathbf{r})$.

B_{lm} : are coefficients corresponding to the function $\dot{U}_l(\mathbf{r})$.

The FP-LAPW functions are plane waves only in the interstitial zones, as in the APW method.

Radial functions can be developed in the vicinity of E_l as follows [40]:

$$U_l(\mathbf{E}, \mathbf{r}) = U_l(E_l, \mathbf{r}) + (\mathbf{E} - E_l) \dot{U}_l(E_l, \mathbf{r}) + \mathbf{O}((\mathbf{E} - E_l)^2) \quad (\text{II.41})$$

With : $\mathbf{O}((\mathbf{E} - E_l)^2)$ denotes the squared error committed.

The FP-LAPW method induces an error on the wave functions of the order of $\mathbf{O}((\mathbf{E} - \mathbf{E}_l)^2)$ and another on the band energy of the order of $\mathbf{O}((\mathbf{E} - \mathbf{E}_l)^4)$ [41]. We can obtain all the valence bands in a large energy region with a single \mathbf{E}_l . In the event that this is not possible, we divide the energy window into two parts.

II.6.3 The role of linearization energies \mathbf{E}_l

We have already mentioned above that the errors in the wave function (charge density) are of the order of $\mathbf{O}((\mathbf{E} - \mathbf{E}_l)^2)$ and in the energy bands of the order of $\mathbf{O}((\mathbf{E} - \mathbf{E}_l)^4)$, which indicates that a parameter should be chosen near the center of the band where a good result is desired. The choice of the parameter \mathbf{E}_l can be optimized by calculating the total energy of the system for several values of \mathbf{E}_l and selecting the one that gives the lowest energy. Unfortunately, while these strategies work well in many cases, they fail miserably in several others.

The reason for this failure is described by the presence and extent of the core state (only known as the semi-core state) in several elements in particular: alkali metals, rare earths, recently transition metals, and actinides. As mentioned, the augmented functions $\mathbf{U}_l(\mathbf{r})\mathbf{Y}_{lm}(\mathbf{r})$ and $\dot{\mathbf{U}}_l(\mathbf{r})\mathbf{Y}_{lm}(\mathbf{r})$ are orthogonal for each core state; this condition is never exactly satisfied except in the case where the core states do not have the same l .

The effects of this inaccurate orthogonality to the core states in the FPLAPW method are sensitive to the choices of l . The most critical case, where there is an overlap between the (FP-LAPW) bases and the core states, which introduces false core states into the energy spectrum, is known as ghost bands. The latter are easily identified, have a very small dispersion, are highly localized in the sphere, and have an l character of the core state. To eliminate ghost bands from the spectrum, we can set the the energy parameter \mathbf{E}_l equal to the energy of the core state

II.6.4 Local orbital development

The purpose of the FP-LAPW method is to obtain precise band energies near the linearization energies \mathbf{E}_l [41]. In most materials, it is sufficient to choose these energies near the center of the bands. However, this is not always possible, and there are materials for which selecting a single value of \mathbf{E}_l is not enough to calculate all the band energies. This is the case for materials with 4f orbitals [42-43] and transition metals [44-45]. This is the fundamental problem of the semi-core state, which is intermediate between the valence state and the core state. To remedy this situation, the following approach is used:

- ✓ Or the use of multiple energy windows (Figure (II.5)).
- ✓ Or to use local orbital development.

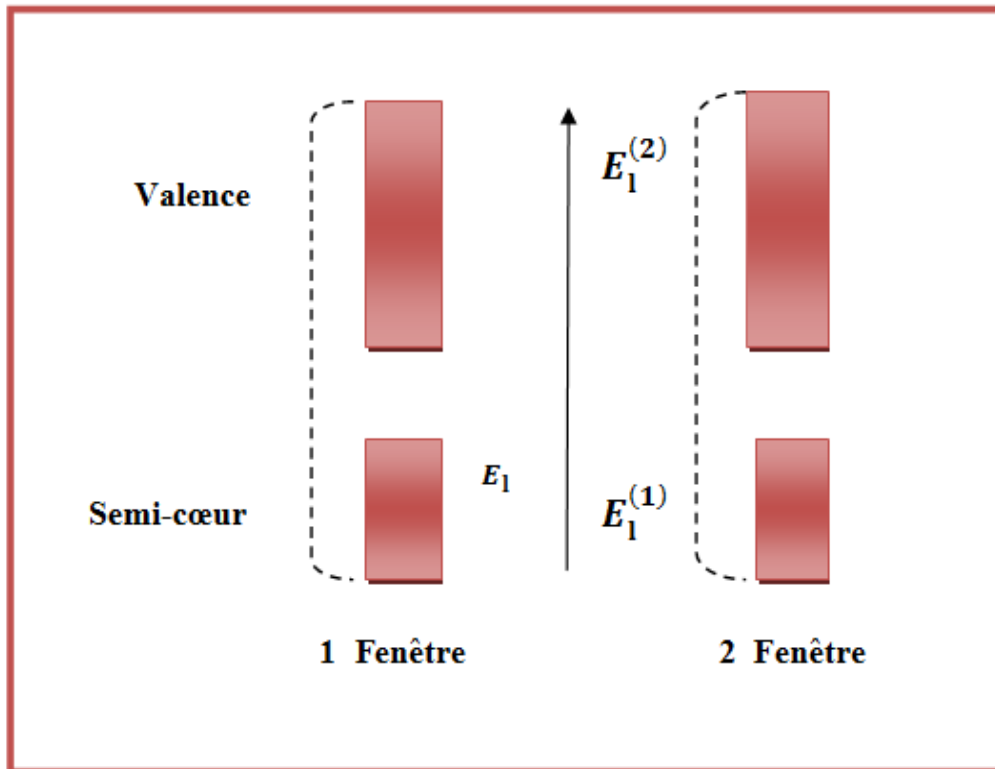


Figure II.5: Multiple energy windows.

II.6.5 The APW + lo method

The issue with the APW method was the energy dependency of the set of basic functions. This dependency could be eliminated in the LAPW+LO method but at the cost of a larger base size, where both APW and LAPW+LO methods acquire an important limitation.

Sjösted, Nordström and Singh [46] have improved on this by developing a basis that combines the advantages of the APW method with those of the LAPW+LO method. This method is called "APW+lo", it corresponds to an energy independent basis (as was in the LAPW+LO method), In addition, it requires only one plane wave cut-off energy, where this cut-off energy is very slightly higher than that required in the APW method.

It consists in using a standard APW basis but considering $U_l(\mathbf{R})$ for a fixed energy E_l in order to keep the advantage brought by the linearization of the problem at eigenvalues. Since an energy base is fixed, this method does not provide a satisfactory description of the eigenfunctions, local orbitals are also added to provide variational flexibility in the radial basis functions.

An "APW+lo" base is defined by the combination of the following two types of wave functions wave functions:

- APW plane waves with a set of fixed E_l energies [47]:

$$\varphi(\mathbf{r}) = \begin{cases} \frac{1}{\Omega^{1/2}} \sum_G C_G e^{i(\mathbf{R}+\mathbf{G})\cdot\mathbf{r}} & r > R_\alpha \\ \sum_{lm} A_{lm} U_l^\alpha(\mathbf{r}, E_l) Y_{lm}(\mathbf{r}) & r < R_\alpha \end{cases} \quad (\text{II.42})$$

- Local orbitals different from those of the LAPW+LO method, are defined by [47]:

$$\varphi(\mathbf{r}) = \begin{cases} 0 & r > R_\alpha \\ [A_{lm} U_l(\mathbf{r}, E_l) + B_{lm} \dot{U}_l(\mathbf{r}, E_l)] Y_{lm}(\mathbf{r}) & r < R_\alpha \end{cases} \quad (\text{II.43})$$

In a calculation, a mixed LAPW and APW+lo basis can be used for different atoms and even for different values of the and even for different values of the l . In general, orbitals that converge more slowly with the plane wave number (such as the 3d states of the transition elements), or atoms with a small sphere size are described by the APW+lo basis and the rest by the LAPW basis [47].

II.6.6 The LAPW+LO method

The FP-LAPW method generally gives accurate band energies in the vicinity of the linearization energies, and in most materials, it is sufficient to choose these energies in the neighborhood of the center of the bands. In order to improve the linearization and make it possible to treat valence and semicore states in a single energy window, so-called local orbitals (LO) are added to the LAPW database and consist of a linear combination of two radial functions corresponding to two different energies and the derivative with respect to energy of one of these two functions. In [48], we define a local orbital (LO) as follows:

$$\varphi(\mathbf{r}) = \begin{cases} 0 & r > R_\alpha \\ [A_{lm} U_l(\mathbf{r}, E_l) + B_{lm} \dot{U}_l(\mathbf{r}, E_l) + C_{lm}(\mathbf{r}, E_l) +] Y_m^l(\mathbf{r}), & r < R_\alpha \end{cases} \quad (\text{II.44})$$

Where the coefficients C_{lm} are of the same nature as the coefficients A_{lm} and B_{lm} defined previously.

A local orbital is defined for a given atom for each l and m . It is called local because it is null everywhere except in the muffin-tin sphere to which it refers. These local orbitals are then added to the LAPW basis. Thus the addition of local orbitals increases the size of the LAPW basis.

II.6.7 The WIEN2k code

The FP-LAPW method was implemented in the WIEN2k code, a set of programs developed by Blaha, Schwarz and their colleagues [49]. This code has successfully dealt with high temperature superconducting systems [50], minerals, transition metal surfaces [51], non-ferromagnetic oxides [52], molecules as well as the electric field gradient. The calculation procedure involves three steps:

The initialization

It consists of constructing the spatial configuration (geometry), the starting densities, the number of special points required for integration in the Brillouin irreducible zone, etc. All these operations are performed by a series of auxiliary programs that generate:

NN: It is a program that gives the distances between the nearest neighbours, and helps to determine the atomic radius of the sphere.

LSTART: A program that generates the atomic densities and determines the different orbitals are processed in the band structure calculation.

SYMMETRY: it generates the symmetry operations of the space group and determines the point group of individual atomic sites.

KGEN: it generates a number of k points in the Brillouin zone.

DSTART: it generates a starting density for the self-consistent cycle (the SCF cycle) by the superposition of the atomic densities generated in LSTART.

Self-Consistent Calculation

In this step, the energies and electron density of the ground state are calculated according to a convergence criterion (energy, charge density, strength). The sub-programs used are:

LAPW0: Generates the potential from the density.

LAPW1: Calculation of valence bands, eigen values and eigenvectors.

LAPW2: it calculates the valence densities for the eigenvectors.

LCORE: it calculates states and core densities.

MIXER: it mixes the input and output densities

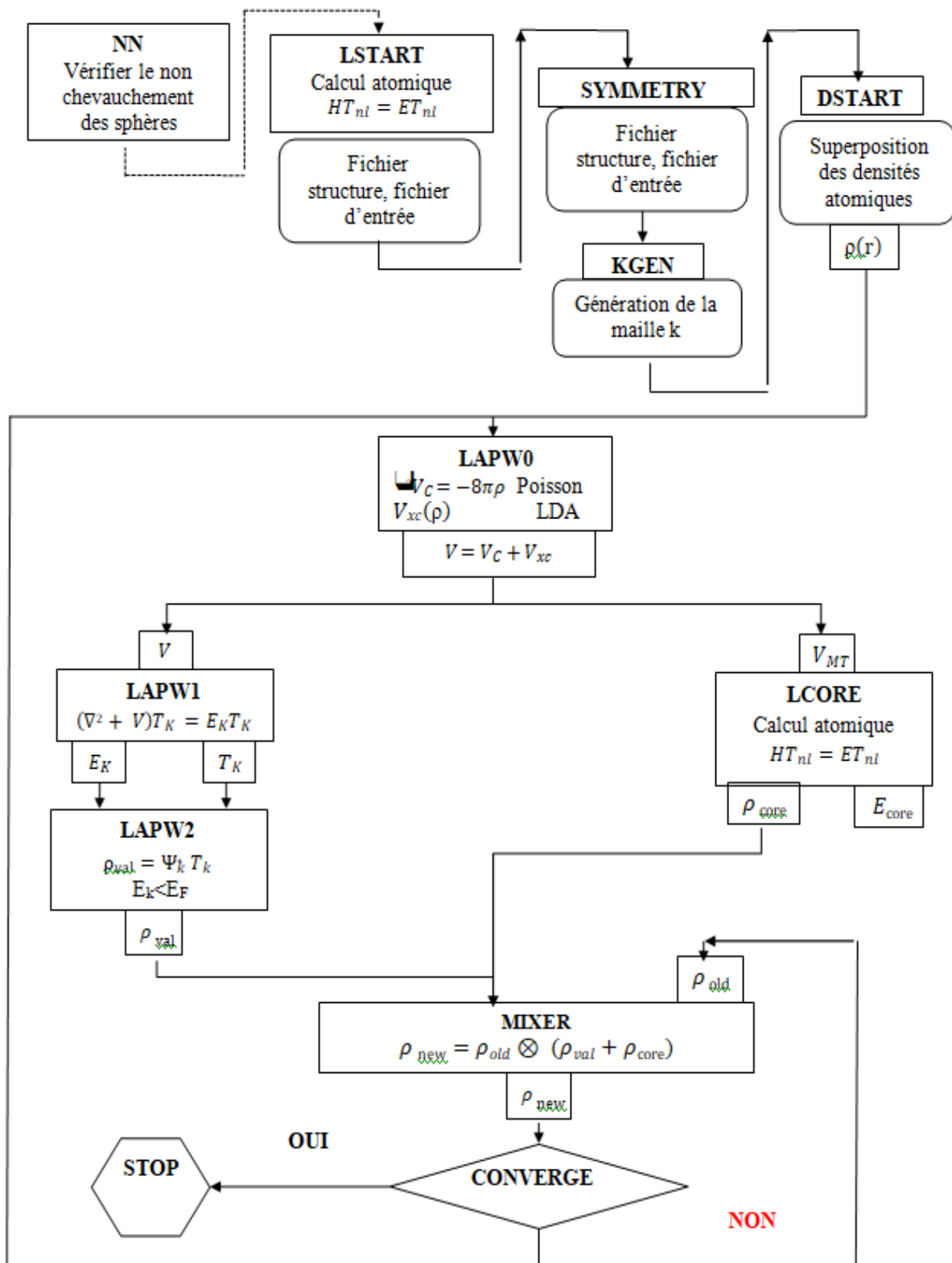


Figure II.6: The structure of the WIEN2k program.

II.7 Spectroscopic Limited Maximum Efficiency Model (SLME)

The Shockley-Queisser limit [53] is a useful tool for determining the maximum efficiency of a solar cell with a single p-n junction. By calculating the percentage of power converted to electrical energy. It provides a correlation between a material's bandgap and its maximum efficiency. Yu and Zunger [54] have recently expanded on the work of Shockley and Queisser by employing the Spectroscopic Limited Maximum Efficiency (SLME) and integrating the absorption spectrum, the absorber layer thickness and accounts for different types of optical transitions near the absorption threshold in the efficiency estimation. A variety of solar absorber materials, including perovskites [55-56], chalcogenides [57-58], and other materials [59-60], have been effectively treated with the SLME model. The highest solar cell efficiency, according to theory, is defined as the ratio of the total incident solar energy density (**P_{in}**) to the maximum output power density (**P_{max}**). By numerically optimizing the product of voltage (**V**) and current density (**J**), P_{max} is found [61].

$$\eta = \frac{P_{\max}}{P_{\text{in}}} \quad (\text{II.45})$$

The link between current density (**J**) and voltage (**V**) can be stated using the following equation,

supposing that the solar cell operating at temperature **T** functions as an ideal diode and is exposed to the photon flux I_{sun}

$$J = J_{\text{sc}} - J_0(e^{eV/KT} - 1) \quad (\text{II.46})$$

This equation uses the following notations: **e** = elementary charge, **V** = potential across the absorber layer, and **k** = Boltzmann's constant. The first term is the short-circuit current density, or **J_{sc}**, which can be written as follows:

$$J_{\text{sc}} = e \int_0^{\infty} a(E) I_{\text{sun}}(E) dE \quad (\text{II.47})$$

Here, I_{sun} stands for the AM1.5G solar spectrum [62], and **a(E)** indicates the photon absorptivity. The thickness (**L**) of the material and the absorption coefficient (**α**)

$$\alpha(E) = \frac{4\pi E}{hc} \sqrt{\frac{|\epsilon(E)| - \epsilon_1(E)}{2}} \quad (\text{II.47})$$

And

$$a(E) = 1 - e^{-2\alpha(E)L} \quad (\text{II.48})$$

The reverse saturation current (J_0), which represents the total electron-hole recombination current (comprising radiative and nonradiative components) at equilibrium in the dark, is the factor in the second term of equation (II.46).

$$J_0 = J_0^r + J_0^{nr} = \frac{J_0^r}{f_r} \quad (\text{II.49})$$

The fraction of the radiative recombination current is represented by f_r in this context. To approximate f_r for the SLME, use

$$f_r = e^{E_g - E_g^{da}/KT} \quad (\text{II.50})$$

In this case, E_g stands for the fundamental band gap and E_g^{da} is the direct allowed band gap of the material.

According to the detailed balance principle, identical rates of absorption and emission across cell surfaces are necessary for the equilibrium condition in the absence of light. Consequently, the rate at which black-body photons from the surrounding thermal environment are absorbed through the front surface can be used to calculate J_0^r .

$$J_0^r = e\pi \int_0^\infty \alpha(E) I_{bb}(E, T) dE \quad (\text{II.51})$$

where the black-body spectrum at temperature T is indicated by I_{bb} . The photon flux is used to express the black-body spectrum I_{bb} and the solar spectrum I_{sun} . To optimize the power density, can be reformulated as

$$\eta = \frac{P_{max}}{P_{in}} = \frac{\max\{(J_{sc} - J_0(e^{eV/KT} - 1))V\}_V}{\int_0^\infty EI_{sun}(E) dE} \quad (\text{II.52})$$

II.8 BoltzTrap

The BoltzTrap program calculates electron transport coefficients, which describe the movement of electrons in a material [63]. This program utilizes Boltzmann's semi-classical transport theory and applies the relaxation time approximation to simplify transport coefficient calculations.

To run BoltzTraP, the following input files are required:

- ❖ A file containing the electronic band structure data in energy and band format along high-symmetry lines in the Brillouin zone.

- ❖ Fermi energy value.
- ❖ Parameters for numerical integration, including the number of k-points and the energy cut-off.
- ❖ Optional files to define the temperature range and doping concentration. The output files will include calculated transport properties like electrical conductivity, Seebeck coefficient, and thermal conductivity.

II.9 VASP code

The VASP (Vienna ab initio Simulation Package) calculation code [64]. This is a code for DFT calculations based on the periodic approach, where the system is modeled as an infinitely replicated supercell. This method is well-suited for studying surfaces by simulating infinite systems. The VASP code solves the Kohn-Sham equations using a plane wave basis. In our work, electron exchange and correlation effects were treated using the generalized gradient approximation (GGA) with the Perdew-Burke-Ernzerhof (PBE) functional and PAW-type pseudopotentials.

II.9.1 Files used by VASP

INCAR file is the central input file of VASP. It determines 'what to do and how to do it', and contains a relatively large number of parameters. Most of these parameters have convenient defaults, and a user unaware of their meaning should not change any of the default values. Because of the complexity of the INCAR file, we have devoted a section on its own to the INCAR file.

POTCAR file contains the pseudopotential for each atomic species used in the calculation. If the number of species is larger than one simply concatenates the POTCAR files of the species.

KPOINTS file contains the k-point coordinates and weights or the mesh size for creating the k-point grid.

POSCAR file contains the lattice geometry and the ionic positions, optionally also starting velocities and predictor-corrector coordinates for a MD-run.

II.10 Conclusion

In this chapter, we explore the various approximations used for different electronic states in solids. Density Functional Theory (DFT) is highlighted as an alternative quantum mechanical approach to the Hartree-Fock method. The main advantage of DFT is its ability to model large relative systems with high accuracy, surpassing other methods that require significant numerical effort to account for electronic correlations. DFT incorporates electronic correlation within its formalism. Since the 1980s, improvements in algorithms for solving the Kohn-Sham equations self-consistently, using wave functions as a basis, have greatly enhanced the efficiency of this method. However, the correlation exchange term remains undetermined and is handled through various approximations such as the Local Density Approximation (LDA), the Generalized Gradient Approximation (GGA), and TB-mBJ. Numerical methods are employed to solve the Kohn-Sham equations, including the Linearly Augmented Plane Wave (LAPW) method, an adaptation of the Slater APW method. The LAPW method utilizes plane waves in the interstitial region, augmented in the spheres, to achieve precise band energies near the linearization energies E_l . It has been further refined into methods like LAPW+LO and APW+lo, offering improved solutions. Finally, to develop a solar cell absorber with optimal efficiency, scientists calculate the Spectroscopic Limited Maximum Efficiency (SLME), which theoretically defines a solar cell's maximum efficiency as the ratio of the total incident solar energy.

Reference

- [1] Schrödinger, E. (1926). An undulatory theory of the mechanics of atoms and molecules. *Physical Review*, 28(6), 1049–1070. <https://doi.org/10.1103/PhysRev.28.1049>
- [2] Parr, R. G. (1982). Density functional theory. In *Electron Distributions and the Chemical Bond* (pp. 95–100). Springer US.
- [3] Hohenberg, P., & Kohn, W. (1964). Inhomogeneous electron gas. *Physical Review*, 136(3B), B864–B871. <https://doi.org/10.1103/PhysRev.136.B864>
- [4] Baerends, E. J. (2001). Perspective on “Self-consistent equations including exchange and correlation effects” Kohn W., Sham L. J. (1965). *Theoretical Chemistry Accounts*, 106, 265–269. <https://doi.org/10.1007/s002140100215>
- [5] Seddik, T. (2013). Étude ab initio des propriétés électroniques de matériaux [Doctoral dissertation, Université de Sidi Bel Abbès].
- [6] Schrödinger, E. (1926). Quantisierung als Eigenwertproblem. *Annalen der Physik*, 385(13), 437–490.
- [7] Kohn, W. (1999). Nobel lecture: Electronic structure of matter—Wave functions and density functionals. *Reviews of Modern Physics*, 71(5), 1253–1266. <https://doi.org/10.1103/RevModPhys.71.1253>
- [8] Born, M., & Oppenheimer, J. R. (1927). Zur Quantentheorie der Molekeln. *Annalen der Physik*, 389, 457–484.
- [9] Fock, V. (1930). Näherungsmethode zur Lösung des quantenmechanischen Mehrkörperproblems. *Zeitschrift für Physik*, 61, 126–148; 62, 795–802.
- [10] Hartree, D. R. (1928). The wave mechanics of an atom with a non-Coulomb central field. Part I. Theory and methods. *Mathematical Proceedings of the Cambridge Philosophical Society*, 24(1), 89–110.
- [11] Blase, X. (2000). DFT — Les fondements. *École SéMat*.
- [12] Cottenier, S. (2002). Density Functional Theory and the family of (L)APW-methods: A step-by-step introduction (Version 4.0, p. 41). Instituut voor Kern- en Stralingsfysica, KU Leuven.
- [13] Thomas, L. H. (1930). A transformation of a formula of Sommerfeld. *Mathematical Proceedings of the Cambridge Philosophical Society*, 26(2), 211–214.
- [14] Fermi, E. (1928). Eine statistische Methode zur Bestimmung einiger Eigenschaften des Atoms und ihre Anwendung auf die Theorie des periodischen Systems der Elemente. *Zeitschrift für Physik*, 48(1), 73–79.

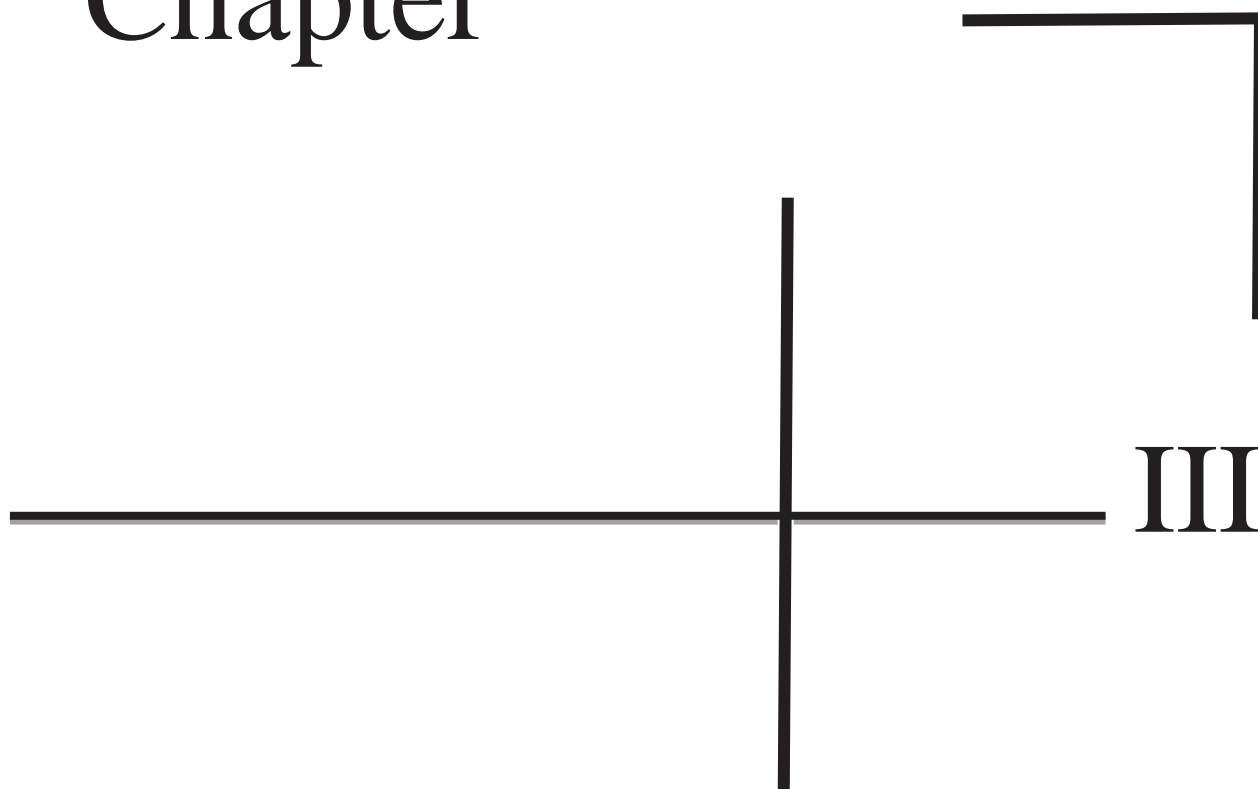
- [15] Hohenberg, P., & Kohn, W. (1964). Inhomogeneous electron gas. *Physical Review*, 136(3B), B864–B871. <https://doi.org/10.1103/PhysRev.136.B864>
- [16] Von Barth, U., & Hedin, L. (1972). A local exchange-correlation potential for the spin-polarized case. I. *Journal of Physics C: Solid State Physics*, 5(13), 1629–1642.
- [17] Lundqvist, S., & March, N. H. (1983). In N. H. March & S. Lundqvist (Eds.), *Theory of the inhomogeneous electron gas* (Vol. 38, pp. 135–221). Plenum Press.
- [18] Gunnarsson, O., & Lundqvist, B. I. (1976). Exchange and correlation in atoms, molecules, and solids by the spin-density-functional formalism. *Physical Review B*, 13(10), 4274–4298. <https://doi.org/10.1103/PhysRevB.13.4274>
- [19] Vosko, S. H., Wilk, L., & Nusair, M. (1980). Accurate spin-dependent electron liquid correlation energies for local spin density calculations: A critical analysis. *Canadian Journal of Physics*, 58(8), 1200–1211. <https://doi.org/10.1139/p80-159>
- [20] Perdew, J. P., & Wang, Y. (1992). Accurate and simple analytic representation of the electron-gas correlation energy. *Physical Review B*, 45(23), 13244–13249. <https://doi.org/10.1103/PhysRevB.45.13244>
- [21] Lieb, E. H., & Wu, F. Y. (1968). Absence of Mott transition in an exact solution of the short-range, one-band model in one dimension. *Physical Review Letters*, 20(25), 1445–1448. <https://doi.org/10.1103/PhysRevLett.20.1445>
- [22] Singh, D. J., & Nordström, L. (2006). *Planewaves, pseudopotentials and the LAPW method* (2nd ed.). Springer.
- [23] Antonov, V., Harmon, B. N., & Yaresko, A. N. (2004). *Electronic structure and magneto-optical properties of solids*. Kluwer Academic Publishers.
- [24] Sham, L. J., & Kohn, W. (1966). One-particle properties of an inhomogeneous interacting electron gas. *Physical Review*, 145(2), 561–567. <https://doi.org/10.1103/PhysRev.145.561>
- [25] Perdew, J. P., & Burke, K. (1996). Comparison shopping for a gradient-corrected density functional. *International Journal of Quantum Chemistry*, 57(3), 309–319. [https://doi.org/10.1002/\(SICI\)1097-461X\(1996\)57:3<309::AID-QUA6>3.0.CO;2-Q](https://doi.org/10.1002/(SICI)1097-461X(1996)57:3<309::AID-QUA6>3.0.CO;2-Q)
- [26] Becke, A. D. (1988). Density-functional exchange-energy approximation with correct asymptotic behavior. *Physical Review A*, 38(6), 3098–3100. <https://doi.org/10.1103/PhysRevA.38.3098>

- [27] Perdew, J. P., Burke, K., & Ernzerhof, M. (1996). Generalized gradient approximation made simple. *Physical Review Letters*, 77(18), 3865–3868. <https://doi.org/10.1103/PhysRevLett.77.3865>
- [28] Engel, E., & Vosko, S. H. (1993). Exact exchange-only potentials and the virial relation as microscopic criteria for generalized gradient approximations. *Physical Review B*, 47(20), 1316.
- [29] Perdew, J. P. (1985). Density functional theory and the band gap problem. *International Journal of Quantum Chemistry*, 28(S19), 497–523.
- [30] Johnson, E. R., & Becke, A. D. (2006). A post-Hartree-Fock model of intermolecular interactions: Inclusion of higher-order corrections. *The Journal of Chemical Physics*, 124(17), 174104.
- [31] Tran, F., & Blaha, P. (2009). Accurate band gaps of semiconductors and insulators with a semilocal exchange-correlation potential. *Physical Review Letters*, 102(22), 226401.
- [32] Tran, F., Blaha, P., Schwarz, K., Novák, P., & Eschrig, H. (2007). Performance on molecules, surfaces, and solids of the Wu-Cohen GGA exchange-correlation energy functional. *Physical Review B*, 75(11), 115131.
- [33] Henderson, T. M., Paier, J., & Scuseria, G. E. (2011). Accurate treatment of solids with the HSE screened hybrid. *Physica Status Solidi (b)*, 248(4), 767–774.
- [34] Faleev, S. V., van Schilfgaarde, M., & Kotani, T. (2004). Quasiparticle self-consistent GW theory. *Physical Review Letters*, 93(12), 126406.
- [35] Aulbur, W. G., Jönsson, L., & Wilkins, J. W. (2000). Quasiparticle calculations in solids. *Solid State Physics*, 54, 1–218.
- [36] Becke, A. D., & Roussel, M. R. (1989). Exchange holes in inhomogeneous systems: A coordinate-space model. *Physical Review A*, 39(8), 3761.
- [37] Becke, A. D. (1993). A new mixing of Hartree-Fock and local density-functional theories. *The Journal of Chemical Physics*, 98(2), 1372–1377.
- [38] Slater, J. C. (1951). A simplification of the Hartree-Fock method. *Physical Review*, 81(3), 385. [39] Andersen, O. K. (1975). Linear methods in band theory. *Physical Review B*, 12(8), 3060.
- [40] Cottenier, S. (2002). *Density Functional Theory and the Family of (L)APW-Methods: A Step-by-Step Introduction*. ISBN 90807215.
- [41] Loucks, T. L. (1967). Electronic structure of zirconium. *Physical Review*, 159(3), 544.

- [42] Singh, D. J. (1991). Adequacy of the local-spin-density approximation for Gd. *Physical Review B*, 44(14), 7451.
- [43] Goedecker, S., & Maschke, K. (1990). Alternative approach to separable first-principles pseudopotentials. *Physical Review B*, 42(14), 8858.
- [44] Singh, D., & Krakauer, H. (1991). H-point phonon in molybdenum: Superlinearized augmented-plane-wave calculations. *Physical Review B*, 43(2), 1441.
- [45] Singh, D. J., Schwarz, K., & Blaha, P. (1992). Electric-field gradients in $\text{YBa}_2\text{Cu}_3\text{O}_7$: Discrepancy between experimental and local-density-approximation charge distributions. *Physical Review B*, 46(9), 5849.
- [46] Sjöstedt, E., Nordström, L., & Singh, D. J. (2000). An alternative way of linearizing the augmented plane-wave method. *Solid State Communications*, 114(1), 15–20.
- [47] Blaha, P., Schwarz, K., Madsen, G. K. H., Kvasnicka, D., & Luitz, J. (2001). WIEN2k: An augmented plane wave + local orbitals program for calculating crystal properties. Vienna University of Technology.
- [48] Singh, J. D. (1994). Ground-state and optical properties of materials. *Physical Review A*, 3100, 1–5.
- [49] Singh, J. D. (1994). Ground-state and optical properties of materials. *Physical Review A*, 3100, 1–5.
- [50] Schwarz, K., Ambrosch-Draxl, C., & Blaha, P. (1990). Charge distribution and electric-field gradients in $\text{YBa}_2\text{Cu}_3\text{O}_{7-x}$. *Physical Review B*, 42(4), 2051.
- [51] Kohler, B., Kresse, G., Hafner, J., & Schmid, M. (1995). Frustrated H-induced instability of Mo(110). *Physical Review Letters*, 74(8), 1387.
- [52] Wang, X. G., Weiss, W., Shaikhutdinov, S., Ritter, M., Petersen, M., Wagner, F., Schlögl, R., & Scheffler, M. (1998). Theoretical and experimental studies of the interaction of hydrogen with molybdenum surfaces. *Physical Review Letters*, 81(5), 1038.
- [53] Kang, L., Lin, Z., Lin, H., Xie, Z., Wu, K., Li, Z., & Wu, X. (2013). First principles selection and design of mid-IR nonlinear optical halide crystals. *Journal of Materials Chemistry C*, 1(44), 7363–7370.
- [54] Yu, L., & Zunger, A. (2012). Identification of potential photovoltaic absorbers based on first-principles spectroscopic screening of materials. *Physical Review Letters*, 108(6), 068701.
- [55] Chen, C., Wu, Y., Jiang, A., & Wu, B. (2012). *Nonlinear optical borate crystals: Principles and applications*. John Wiley & Sons.

- [56] Yin, W.-J., Shi, T., & Yan, Y. (2014). Unique properties of halide perovskites as possible origins of the superior solar cell performance. *Advanced Materials*, 26(27), 4653–4658.
- [57] Yin, W.-J., Shi, T., Yan, Y., & Wei, S.-H. (2015). Halide perovskite materials for solar cells: A theoretical review. *Journal of Materials Chemistry A*, 3(17), 8926–8942.
- [58] Sarmadian, N., Saniz, R., Partoens, B., & Lamoen, D. (2016). First-principles study of the optoelectronic properties and photovoltaic absorber layer efficiency of Cu-based chalcogenides. *Journal of Applied Physics*, 120(8), 085104.
- [59] Lee, I.-H., Lee, K., Kim, S.-W., & Chang, K. J. (2014). Computational search for direct band gap silicon crystals. *Physical Review B*, 90(11), 115209.
- [60] Huang, X., Lin, Y., Mecholsky, N. A., & Pantelides, S. T. (2015). Hexagonal rare-earth manganites as promising photovoltaics and light polarizers. *Physical Review B*, 92(12), 125201.
- [61] Choudhary, K., Garrity, K. F., Reid, A. C. E., & Tavazza, F. (2019). Accelerated discovery of efficient solar cell materials using quantum and machine-learning methods. *Chemistry of Materials*, 31(15), 5900–5908
- [62] Collins, D. G., Wells, M. B., & Sekera, Z. (1972). Backward Monte Carlo calculations of the polarization characteristics of the radiation emerging from spherical-shell atmospheres. *Applied Optics*, 11(11), 2684–2696.
- [63] Madsen, G. K. H., & Singh, D. J. (2006). BoltzTraP: A code for calculating band-structure dependent quantities. *Computer Physics Communications*, 175(1), 67–71.
- [64] Kresse, G., & Joubert, D. (1999). From ultrasoft pseudopotentials to the projector augmented-wave method. *Physical Review B*, 59(3), 1758.

Chapter



**Thermoelectric and
Optoelectronic Efficiency
of $\text{Rb}_2\text{AgSb}(\text{Cl}_{1-x}\text{Br}_x)_6$
Alloys**

III.1 Introduction

Materials from the perovskite family show great potential for solar cell applications because of their excellent optical properties and the relatively low cost of their production methods [1]. These physical properties enable a wide range of applications in daily life, including light-emitting diodes (LEDs), nonlinear optics (NLO), and other optoelectronic devices [2-7]. In this section, we primarily focused on examining how substituting Cl with Br and Sb with Bi affects the structural, electronic, and optical properties of the compound $\text{Rb}_2\text{AgSbCl}_6$. For all calculations, we employed the FP-APW method as implemented in the Wien2k code within the framework of density functional theory (DFT). We chose numerical simulation because it plays a crucial role in determining the properties of our materials, helping to reduce the costs associated with expensive experiments, model phenomena that are challenging or impossible to observe experimentally, and minimize the risks associated with dangerous or otherwise inaccessible laboratory experiments. Theoretically, previous studies have shown that tailoring the band gap value in $\text{Rb}_2\text{AgSbCl}_6$ results in intriguing optoelectronic and photocatalytic characteristics [8]. Therefore, the primary objective is to enhance the optical and electronic properties of the $\text{Rb}_2\text{AgSb}(\text{Cl}_{1-x}\text{Br}_x)_6$ and $\text{Rb}_2\text{AgSb}_{1-x}\text{Bi}_x\text{Cl}_6$ alloys by employing a band convergence strategy. This is achieved by substituting bromine (Br) for chlorine (Cl) and bismuth (Bi) for antimony (Sb) in the compound $\text{Rb}_2\text{AgSbCl}_6$.

III.2 Calcul details

All calculations are done using the FP-APW+lo method [9-10], implemented in the WIEN2k code [11]. In this technique, the system space is divided into two regions the interstitial one and the muffin-tin spheres with muffin-tin radius (RMT) are chosen in a manner that the MT spheres do not overlap. 2.5, 2.5, 2.5, and 2.21 bohr was done for Rb, Ag, Sb, and Cl, respectively, with the following electronic configuration Rb: $[\text{Kr}] 5s^1$ Ag: $[\text{Kr}] 4d^{10}5s^1$, Sb: $[\text{Kr}] 4d^{10} 5s^2 5p^3$, Cl $[\text{Ne}] 3s^2 3p^5$. The electronic wave functions are expanded up to lmax equal to 4 and 10 outside and inside the MT sphere, respectively. Besides, the expansion of the wave functions and charge density were cut off by the RMTKmax = 7.5 and Gmax = 12 parameters. The exchange-correlation potential is treated by the generalized gradient approximation performed by Wu and Cohen (GGA-WC) [12]. However, since the GGA approximation yields an underestimated band gap value, the

Tran-Blaha modified Becke-Johnson (mBJ) exchange potential is employed [13-14]. Further, the $\text{Rb}_2\text{AgSb}(\text{Cl}_{1-x}\text{Br}_x)_6$ and $\text{Rb}_2\text{AgSb}_{1-x}\text{Bi}_x\text{Cl}_6$ alloys are represented using $1 \times 1 \times 1$ periodic supercells, with each supercell containing 40 atoms in the primitive unit. To explore various Arrangements, chlorine atoms are substituted with bromine atoms and antimony atoms substituted with bismuth atoms, resulting in the creation of $\text{Rb}_2\text{AgSb}(\text{Cl}_{1-x}\text{Br}_x)_6$ and $\text{Rb}_2\text{AgSb}_{1-x}\text{Bi}_x\text{Cl}_6$ alloys respectively with x values ranging from 0.25 to 0.75. Then, the spectroscopic limited maximum efficiency (SLME) model was used to evaluate the photovoltaic efficiency.

III.3 Structural properties

We introduced the use of lead-free double perovskite $\text{Rb}_2\text{AgSbCl}_6$, part of the elpasolite- K_2NaAlF_6 group. This material features alternating SbCl_6 and AgCl_6 octahedra arranged in a cubic crystalline structure similar to rock salt, forming a face-centered cubic (FCC) configuration. The space group symmetry of this structure is $\text{Fm}\bar{3}\text{m}$ (no. 225) [15] (see fig. III.1).

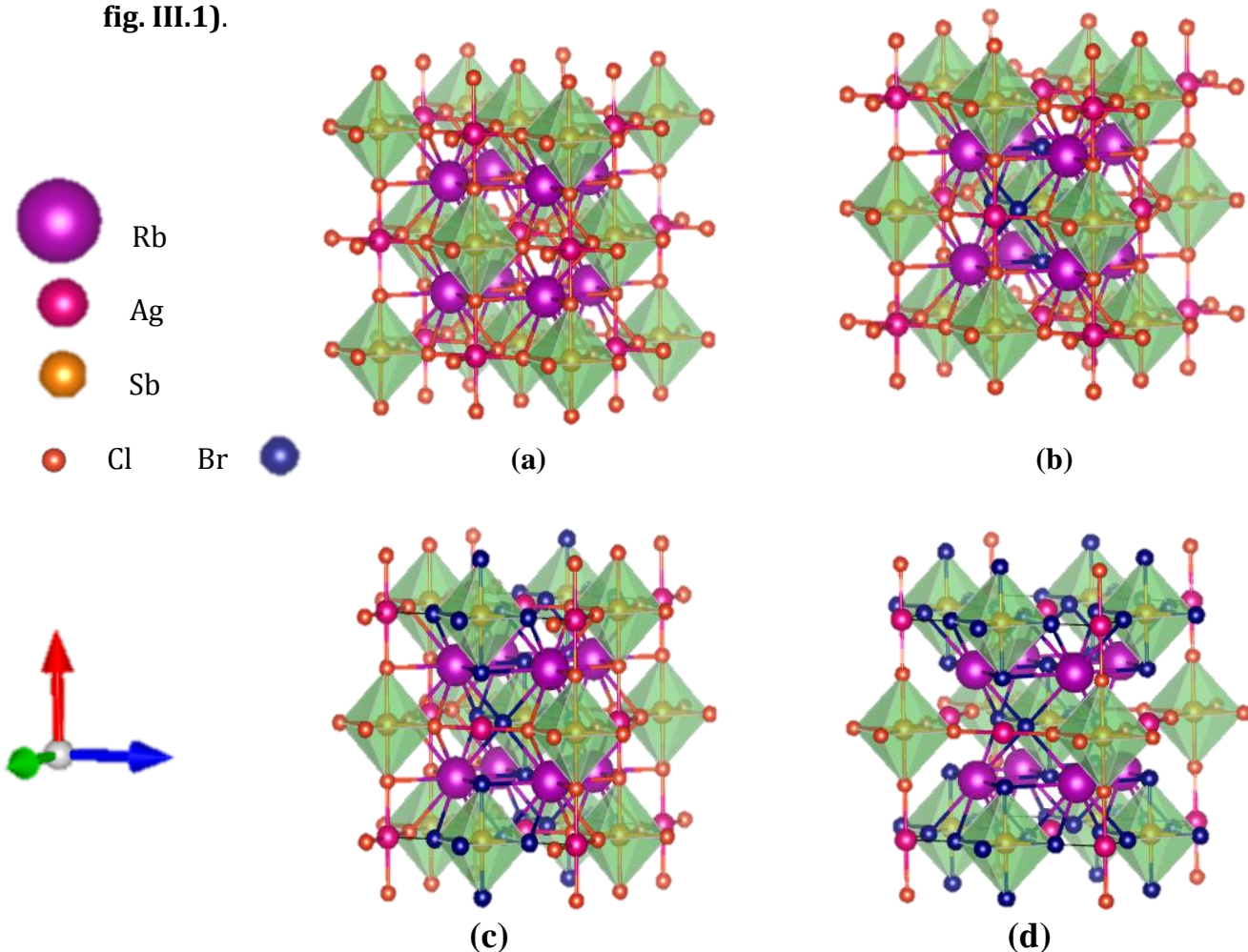


Figure III.1: Crystal structure visualizations of (a) $\text{Rb}_2\text{AgSbCl}_6$, (b) the $\text{Rb}_2\text{AgSb}(\text{Cl}_{0.75}\text{Br}_{0.25})_6$ alloy, (c) $\text{Rb}_2\text{AgSb}(\text{Cl}_{0.5}\text{Br}_{0.5})_6$, and (d) $\text{Rb}_2\text{AgSb}(\text{Cl}_{0.25}\text{Br}_{0.75})_6$.

In this structure, Rb atoms are positioned at 8c with coordinates (0.25, 0.25, 0.25), Sb atoms occupy the 4a position at (0, 0, 0), Ag atoms are located at 4b with coordinates (0.5, 0.5, 0.5), and Cl atoms are found at (0.2504, 0, 0). In order to determine the properties of static equilibrium such as the network parameter a bulk modulus B and its first pressure derivative B' are determined through the Murnaghan equation [16] given by:

$$E(V) = E_0 + \frac{B'}{B'(B'-1)} \left[\gamma \left(\frac{V_0}{V} \right)^{B'} - V_0 \right] + \frac{B}{B'} (V - V_0) \quad (\text{III.1})$$

The parameters, E_0 , V_0 , B' , and B are defined by:

E_0 : The total energy of a given crystal structure's ground state.

V_0 : Equilibrium volume.

B' : The derivative of the modulus of rigidity with respect to the equilibrium pressure.

B: The compression modulus, which measures the rigidity of the crystal

Curve fitting of energy versus volume. The results of the estimated structural properties (a, B and B') of $\text{Rb}_2\text{AgSb}(\text{Cl}_{1-x}\text{Br}_x)_6$ alloys are reported in **Table III.1 & fig.III.2**, demonstrating a strong agreement between the obtained values and theoretical expectations [8]. It is clear that the lattice constants a goes up in the unit cell of $\text{Rb}_2\text{AgSbCl}_6$ as chlorine atoms are gradually replaced with bromine atoms. Conversely, in the $\text{Rb}_2\text{AgSb}(\text{Cl}_{1-x}\text{Br}_x)_6$ alloy, the volume coefficient increases as bromine concentration rises, due to the larger atomic spacing. Additionally, there is a significant increase in the compositional energy E_f . Importantly, the negative value of E_f indicates the thermodynamic stability of all the alloys, the formation energy E_f is predicted as below:

$$E_f(\text{Rb}_2\text{AgSb}(\text{Cl}_{1-x}\text{Br}_x)_6) = \frac{1}{N} (E_T(\text{Rb}_2\text{AgSb}(\text{Cl}_{1-x}\text{Br}_x)_6) - [2E_{\text{Rb}} + E_{\text{Ag}} + E_{\text{Sb}} + 6(1-x)E_{\text{Cl}} + 6xE_{\text{Br}}]) \quad (\text{III.2})$$

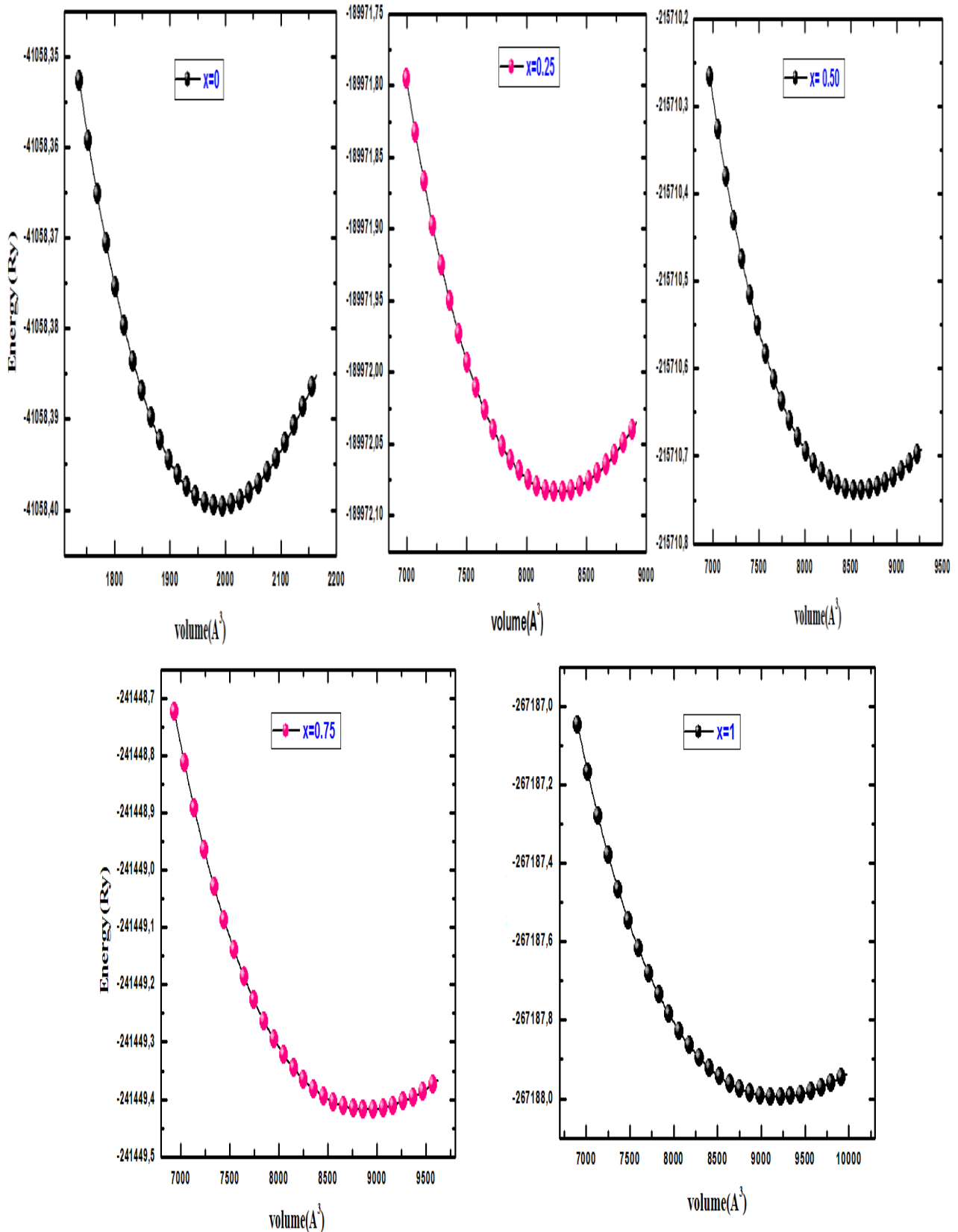


Figure III.2: variation of the total energy as a function of the volume of the $\text{Rb}_2\text{AgSb}(\text{Cl}_{1-x}\text{Br}_x)_6$ alloys

$\text{Rb}_2\text{AgSb}(\text{Cl}_{1-x}\text{Br}_x)_6$		$a(\text{\AA})$	$V(\text{\AA}^3)$	$B(\text{GPa})$	B'	$E_f(\text{eV})$
x = 0	This work	10.56	1177.58	32.74	4.99	-2.8406
	Othercalc.	10.71 [8]	/	30.16 [8]	4.87 [8]	/
x=0.25	This work	10.70	1224.50	31.86	4.55	-2.7194
x=0.5	This work	10.84	1272.51	30.01	4.72	-2.6130
x=0.75	This work	10.96	1318.07	29.16	4.53	-2.5144
X= 1	This work	11.08	1359.97	28.82	4.38	-2.3813
	Othercalc.	11.26 [8]	/	23.65 [8]	5.50 [8]	/

Table III.1 : Calculated lattice constant (a_0), volume (V), bulk modulus (B), derivative of bulk modulus (B') and formation energy (E_f) of $\text{Rb}_2\text{AgSb}(\text{Cl}_{1-x}\text{Br}_x)_6$ alloys.

III.4 Electronic properties

III.4.1 Band structures

According to the wave vector, the energy bands represent the potential energies that an electron can have. To simplify, only the directions with the highest symmetries in the first Brillouin zone are considered. Understanding the band structure is crucial for the development of optical devices. The critical point of the band structure refers to the energy value that separates the maximum of the valence band from the minimum of the conduction band, known as the energy gap. We computed the band structure of $\text{Rb}_2\text{AgSbCl}_6$ and $\text{Rb}_2\text{AgSb}(\text{Cl}_{1-x}\text{Br}_x)_6$ alloys along the high symmetry lines within the first Brillouin zone. **Fig.III.3** clearly shows that in $\text{Rb}_2\text{AgSbCl}_6$, the minimum of the conduction band (CB) and the maximum of the valence band (VB) are not aligned at the same symmetry point ($R-\Gamma$), identifying it as an indirect band gap semiconductor with an estimated GGA+WC value of 1.081 volts. The measured band gap value is notably lower than the theoretical estimate due to the inherent limitations of GGA approximations (as shown in Table 2). Therefore, a different approach, WC-GGA + TB-mBJ, is employed to assess the band structure, yielding a band gap value of 2.08 volts, which aligns more closely with theoretical predictions [8]. Moreover, Figure 2 depicts the band structure of $\text{Rb}_2\text{AgSb}(\text{Cl}_{1-x}\text{Br}_x)_6$ alloys using the WC-GGA + TB-mBJ approximation. It is observed

that substituting a Cl atom with a Br atom leads to a transformation in the minimum conduction band (CB) of the band structure pattern near the Fermi level, resulting in lowered energy levels. Consistent with semiconductor properties, this transformation gradually reduces the band gap value with increasing concentration ($x = 0.25, 0.5, 0.75, 1$). The results are summarized in Table 2.

$\text{Rb}_2\text{AgSb}(\text{Cl}_{1-x}\text{Br}_x)_6$		GGA (eV)	TB-mBj (eV)
$x = 0$	This work	1.081	2.081
	Other calc.	1.05 [8]	2.19 [8]
$x = 0.25$	This work	0.985	1.86
$x = 0.5$	This work	0.798	1.59
$x = 0.75$	This work	0.765	1.438
$x = 1$	This work	0.731	1.344
	Other calc.	0.65 [8]	1.56 [8]

Table III.2: Calculated indirect bandgap using GGA and mBJ potential for $\text{Rb}_2\text{AgSb}(\text{Cl}_{1-x}\text{Br}_x)_6$ alloys.

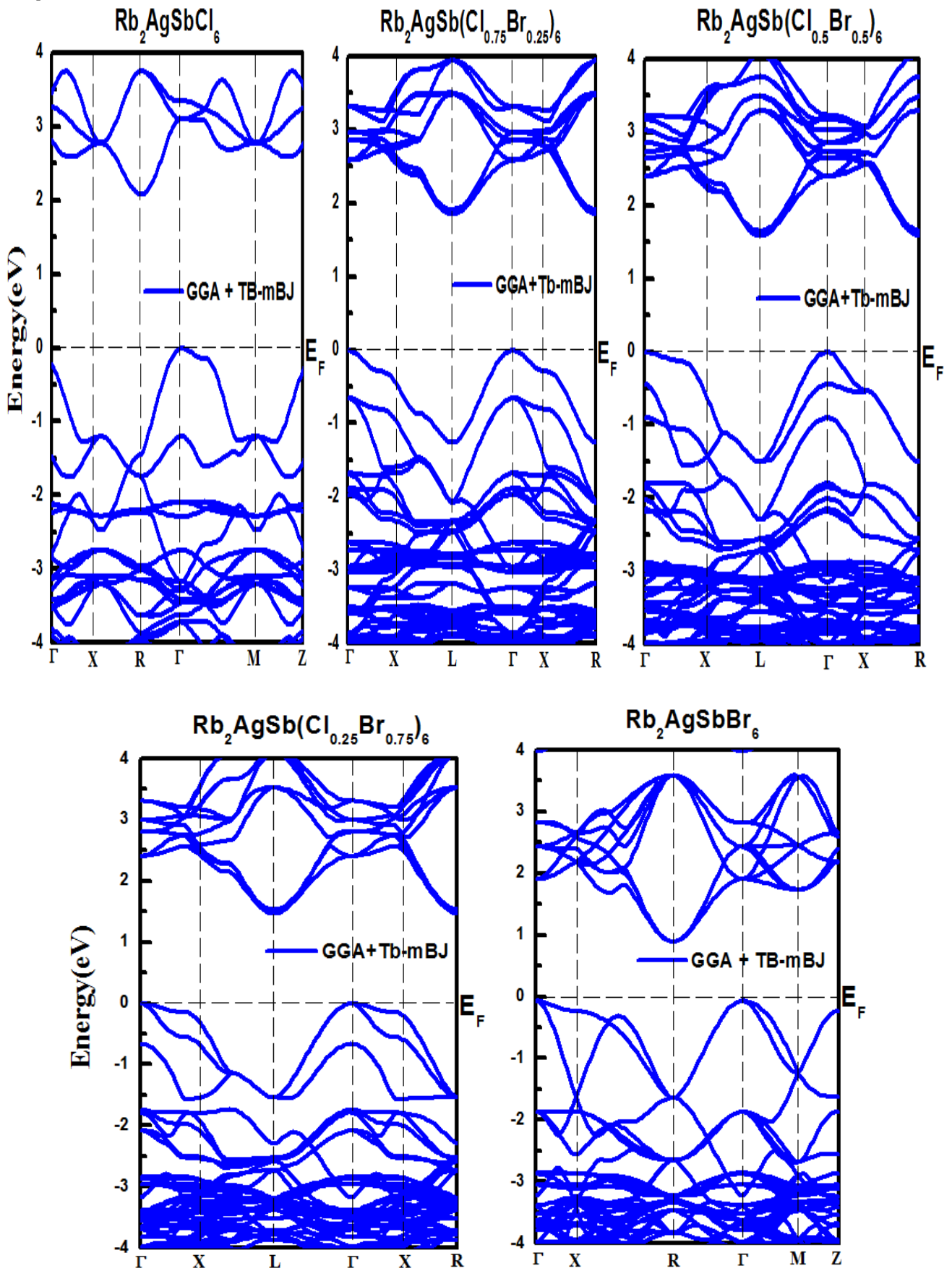


Figure III.3: The computed $\text{Rb}_2\text{AgSb}(\text{Cl}_{1-x}\text{Br}_x)_6$ alloy band structure.

III.4.2 Density of states

The density of electronic states (DOS) $N(E)$ refers to the measurement of the number of electronic states that possess a specific energy within a material. It can also be expressed as $N(E)dE$, which represents the number of electronic states with energies ranging between E and $E+dE$ per unit volume of the solid, or more commonly, per unit cell of the crystal under investigation. The density of states is determined by integrating the spectral function over the first Brillouin zone and is described by the following equation:

$$N(E) = \sum_n \int \frac{d^2K}{4\pi^2} \delta(E - \epsilon) \quad (\text{III.3})$$

To precisely determine the states contributing to each band, we have plotted the total density of states (TDOS) and the partial density of states (PDOS) for the $\text{Rb}_2\text{AgSb}(\text{Cl}_{1-x}\text{Br}_x)_6$ alloys at various concentrations x (ranging from 0 to 1) using the WC-GGA+TB-mBJ approximation.

Figure III.4 shows that the valence band of $\text{Rb}_2\text{AgSbCl}_6$ is separated into two sub-bands. The first, labeled VB1, extends from the top (zero energy) to -5 eV, and the second, labeled VB2, spans from -5 eV to -7 eV. VB1 is primarily composed of cation Ag 'd' states and Sb's' states, which are hybridized with Cl 'p' states, suggesting a covalent nature of the Ag-Cl bond. In contrast, VB2 is derived from a mix of Sb 'p' states and anion Cl 'p' states. Similarly, the conduction band of $\text{Rb}_2\text{AgSbCl}_6$ is divided into two sub-bands. The first, labeled CB1, ranges from zero energy to 4 eV, while the second, labeled CB2, extends from 4 eV to 7 eV. CB1 mainly originates from Sb 'p' states hybridized with Cl 'p' states, while CB2 is derived from Rb's, p, and d' states. The lower part of the conduction band is predominantly influenced by Sb's' and Rb's, p, and d' states. However, the valence band structure of $\text{Rb}_2\text{AgSb}(\text{Cl}_{1-x}\text{Br}_x)_6$ alloys with concentration ($x = 0.25, 0.5, \text{ and } 0.75$) does not change when Cl is substituted with Br, although the presence of the Br "p" state contribution is observed. It's worth noting that $\text{Rb}_2\text{AgSb}(\text{Cl}_{1-x}\text{Br}_x)_6$ alloys with varying concentrations exhibit a higher contribution in both total and partial densities of states compared to $\text{Rb}_2\text{AgSbCl}_6$. This attribute renders these compounds significantly more suitable for optoelectronic applications.

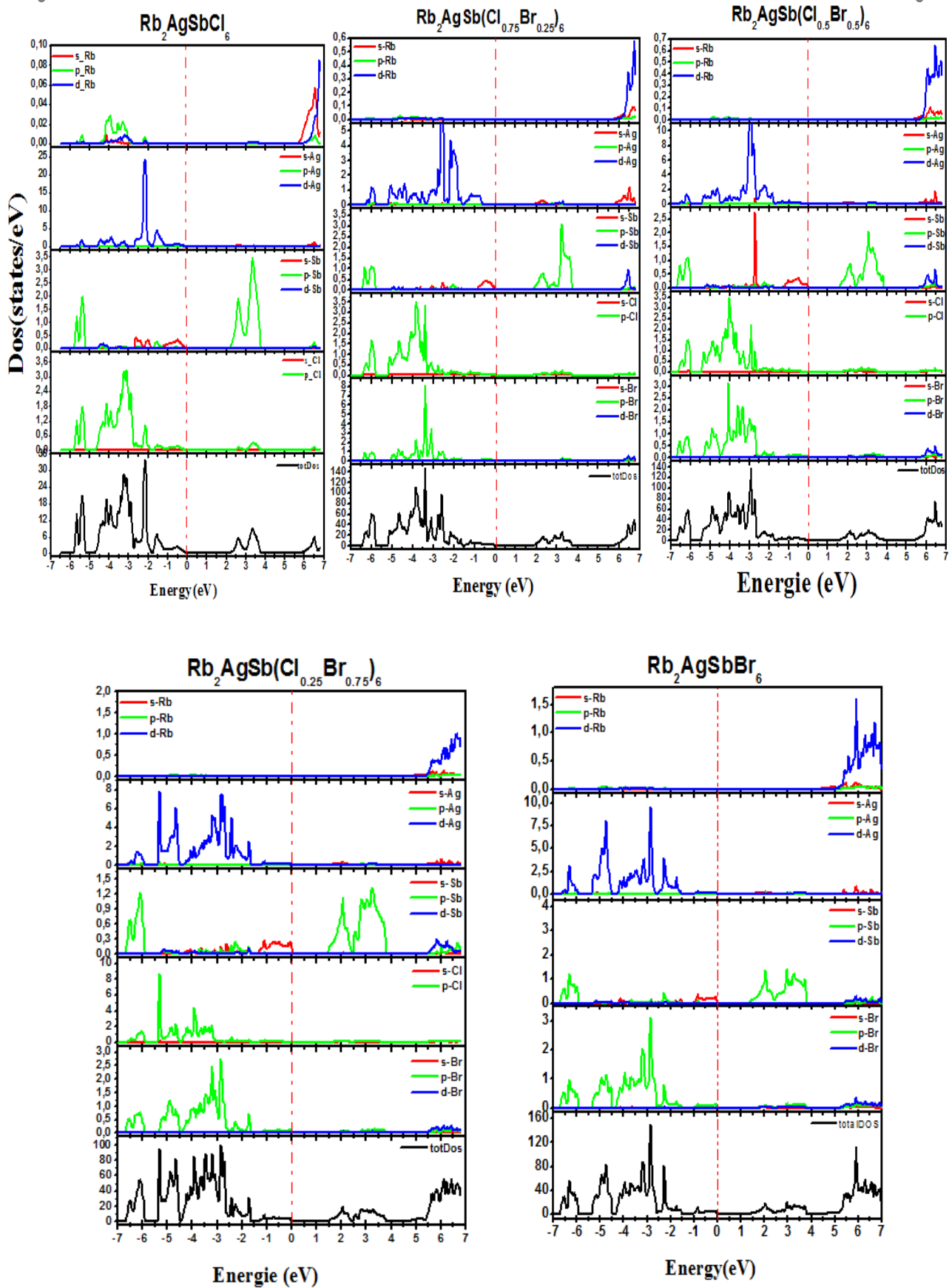


Figure III.4: Total and partial density of states (DOS) of $\text{Rb}_2\text{AgSb}(\text{Cl}_{1-x}\text{Br}_x)_6$ alloys

III.4.3 Carrier effective mass and mobility

Using the calculated band structure, we have calculated the effective mass of holes (m_h^*) from the maximum VB and the electrons effective mass (m_e^*) from the minimum CB for $\text{Rb}_2\text{AgSbCl}_6$ alloys using the following Equation:

$$m^* = \hbar^2 \left(\frac{\partial^2 E}{\partial^2 k} \right)^{-1} \quad (\text{III.4})$$

The k is the wave vector direction. The symbol \hbar and $3(k)$ represent the Planck constant and eigenvalues of the energy band, respectively.

Table 3 presents an overview of the results. It is noted that the electron effective mass is lower than the hole effective mass for pure $\text{Rb}_2\text{AgSbCl}_6$. Given that this mass is associated with the band gap, and considering the tuning of the band gap following Br substitution As a result, we have calculated the hole and electron effective masses for $\text{Rb}_2\text{AgSb}(\text{Cl}_{1-x}\text{Br}_x)_6$ alloys (see Table 3). It is evident that both hole and electron effective masses decrease with the substitution of Cl by the Br atom. Using the deformation potential theory [17], the carrier mobility for this compound can be calculated through the following relation:

$$\mu = \frac{(8\pi)^{1/2} \hbar^4 e C_{ii}}{3(m^*)^{5/2} (k_B T)^{3/2} E_\alpha^2} \quad (\text{III.5})$$

Where \hbar , C_{ii} , e , m^* , k_B , T , E_α are respectively, the reduced Planck constant, elastic modulus, the element charge, effective mass (of a hole (m_h^*) or electron (m_e^*)), Boltzmann constant, temperature, and deformation potential constant of the CB minimum for electron or VB maximum for the hole [18]. Table 3 lists the calculated electron and hole mobilities. It is clear that for pure $\text{Rb}_2\text{AgSbCl}_6$, electron mobility is significantly higher than hole mobility. After substituting Cl with Br, the mobilities of both holes and electrons increase as Br concentration rises, with electron mobility improving by about 70% and hole mobility by 66% after 75% Br substitution. This increase is mainly due to the higher elastic constant and reduced effective carrier masses after doping. However, when Cl is replaced by Br, the mobility decreases slightly for holes compared to other concentrations. High carrier mobility is a highly sought-after property for enhanced photovoltaic performance, as it helps efficiently separate photogenerated carriers and reduces recombination.

Table III.3: the Calculated Hole and electron effective masses m_h^* , m_e^* , deformation potential constants E_{CBM} (eV) and E_{VBM} (eV), carrier mobility μ ($\text{cm}^2 \text{V}^{-1} \text{s}^{-1}$) for $\text{Rb}_2\text{AgSb}(\text{Cl}_{1-x}\text{Br}_x)_6$ alloys

$\text{Rb}_2\text{AgSb}(\text{Cl}_{1-x}\text{Br}_x)_6$	m_h^*/m_0	m_e^*/m_0	E_{CBM}	E_{VBM}	μ_e	μ_h
X= 0	0,184	0,121	-4.71	-6.74	9,755	1,673
X= 0.25	0,159	0,135	-4.60	-6.41	5,200	1,778
X= 0.5	0,126	0,106	-4.81	-6.35	8,785	3,271
X= 0.75	0,084	0,095	-4.88	-6.26	10,899	9,013
X=1	0,080	0,091	-5.01	-6.30	12,394	10,799

III.5 Optical properties

The optical properties of solids play a significant role in both fundamental research and industrial applications. Studies show that light interacts with matter through discrete energy units, known as photons. Recently, it has been demonstrated that in solids, the distribution of electrons among their quantized energy states is temporarily altered under the influence of photons. Grasping these effects is crucial for both technological advancements and fundamental scientific understanding. The optical properties of perovskites can be harnessed for developing optoelectronic devices, including light detectors, LEDs, lasers, and solar cells. To explore this potential, we have calculated various optical parameters for the $\text{Rb}_2\text{AgSb}(\text{Cl}_{1-x}\text{Br}_x)_6$ alloys, such as the complex dielectric function, refractive index, reflectivity, and absorption coefficient.

III.5.1 Dielectric function

Many optical properties are connected to the band structure of a crystal. These properties can typically be derived from the dielectric function, which characterizes the material's linear response to an external electromagnetic field. This function, in turn, determines how radiation propagates through the medium. While the dielectric function is a real quantity when considering a static field, it becomes complex in the case of a dynamic field, denoted as $\epsilon(\omega)$, which varies with frequency [19].

$$\boldsymbol{\varepsilon}(\boldsymbol{\omega}) = \boldsymbol{\varepsilon}_1(\boldsymbol{\omega}) + i\boldsymbol{\varepsilon}_2(\boldsymbol{\omega}) \quad (\text{III.5})$$

Here, $\boldsymbol{\varepsilon}_1$ refers to the real part of the dielectric function, which is associated with the polarization of the surrounding medium, while $\boldsymbol{\varepsilon}_2$ represents the imaginary part, which describes the material's absorption characteristics.

The imaginary component of the dielectric function, $\boldsymbol{\varepsilon}_2$, can be determined using the matrix elements of the momentum between the occupied and unoccupied electronic states within the first Brillouin zone. It can be computed using the following equation [20].

$$\boldsymbol{\varepsilon}_2(\boldsymbol{\omega}) = \frac{e^2\hbar}{\pi m^2 \omega^2} \sum_{v,c} \int_{\text{BZ}} |\mathbf{M}_{ev}(\mathbf{k})|^2 \delta[\boldsymbol{\omega}_{ev}(\mathbf{k}) - \boldsymbol{\omega}] d^3\mathbf{k} \quad (\text{III.6})$$

Here, M refers to the dipole matrix, with v and c representing the initial and final states, respectively. $M_{ev}(\mathbf{k})$ denotes the momentum dipole of the elements, while e is the potential vector defined by the electric field. This represents the matrix elements for direct transitions between valence band states $u_{vk}(\mathbf{r})$ and conduction band states $u_{ck}(\mathbf{r})$. The real part, $\boldsymbol{\varepsilon}_1(\boldsymbol{\omega})$, can be derived from the imaginary part of the dielectric function using the Kramers-Kronig relation [21-22].

$$\boldsymbol{\varepsilon}_1(\boldsymbol{\omega}) = \mathbf{1} + \frac{2}{\pi} \mathbf{P} \int_0^\infty \frac{\boldsymbol{\omega}' \boldsymbol{\varepsilon}_2(\boldsymbol{\omega}')}{\boldsymbol{\omega}'^2 - \boldsymbol{\omega}^2} d\boldsymbol{\omega}' \quad (\text{III.7})$$

Where $\boldsymbol{\omega}$ is the frequency and P is the principal part of the Cauchy integral. The rest of the optical functions, such as the index of refraction, $n(\boldsymbol{\omega})$, the reflectivity $R(\boldsymbol{\omega})$, and the absorption coefficient, α , can be derived easily from the dielectric function.

Based on the calculated electronic structure of $\text{Rb}_2\text{AgSb}(\text{Cl}_{1-x}\text{Br}_x)_6$ alloys and using the GGA TB-mBJ approximation for ($x = 0, 0.25, 0.50, 0.75$, and 1), we determined the real and imaginary parts of the dielectric function for incident photons with energies ranging from 0 eV to 25 eV.

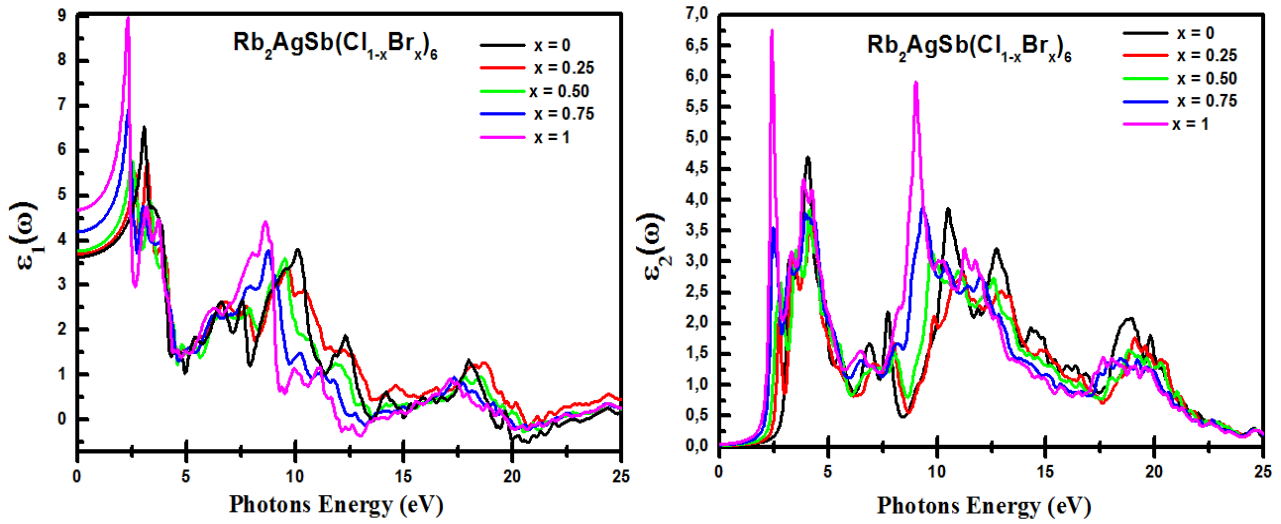


Figure III.5: The complex dielectric function's real (ϵ_1) imaginary (ϵ_2) and component spectra for $\text{Rb}_2\text{AgSb}(\text{Cl}_{1-x}\text{Br}_x)_6$ materials.

Figure III.5: presents the calculated real part, $\epsilon_1(\omega)$, and the imaginary part, $\epsilon_2(\omega)$, of the complex dielectric function for $\text{Rb}_2\text{AgSb}(\text{Cl}_{1-x}\text{Br}_x)_6$ alloys as a function of photon energy $h\nu$. It is observed that the $\epsilon_1(\omega)$ spectrum of pure $\text{Rb}_2\text{AgSbCl}_6$ shows a prominent peak around 4.6 eV, which shifts to lower energies in the other four alloys due to the substitution of Br atoms.

The static dielectric constant $\epsilon_1(\omega)$ for $\text{Rb}_2\text{AgSb}(\text{Cl}_{1-x}\text{Br}_x)_6$ alloys, representing the real part of the dielectric function at zero energy, is listed in **Table III.4**. This constant rises from 3.63 for pure $\text{Rb}_2\text{AgSbCl}_6$ to 4.19 for the $\text{Rb}_2\text{AgSb}(\text{Cl}_{0.25}\text{Br}_{0.75})_6$ alloy and reaches 4.68 for $\text{Rb}_2\text{AgSbBr}_6$, indicating a corresponding decrease in the band gap. This static dielectric constant can be expressed using the following relationship:

$$\epsilon(\omega) = 1 + \left(\frac{h\omega_p}{E_g} \right) \quad (\text{III.7})$$

Where ω_p is the plasma frequency.

Conversely, as shown in the $\epsilon_2(\omega)$ spectra in Fig. III.5, doping $\text{Rb}_2\text{AgSbCl}_6$ with 25% Br introduces new peaks in the visible region. These additional peaks arise from photon absorption due to indirect interband transitions. Notably, the position of these peaks shifts with increasing Br concentration, with the complex $\text{Rb}_2\text{AgSb}(\text{Cl}_{0.25}\text{Br}_{0.75})_6$ and $\text{Rb}_2\text{AgSbBr}_6$ compounds exhibiting shifts from 2.94 eV to 2.38 eV, with peak values at 3.53 eV and 6.74 eV. This shift is primarily caused by electron transitions from the valence

bands of p-Br, p-Cl, s-Sb, and d-Ag to the p-Sb conduction band, as evidenced by the density of states analysis for $\text{Rb}_2\text{AgSbBr}_6$.

The determination of the two parts of the dielectric function allows us to evaluate other optical properties such as absorption $\alpha(\omega)$, reflectivity $R(\omega)$ and refractive index $n(\omega)$.

III.5.2 Refractive index

The refractive index of a material is typically expressed in its real form, but it can also be represented in a complex form:

$$\mathbf{N}(\omega) = \mathbf{n}(\omega) + i\mathbf{k}(\omega) \quad (\text{III.8})$$

With N the complex refractive index, n the real refractive index, k the extinction coefficient.

The refractive index (n) of a material indicates how much electromagnetic radiation is slowed down when it passes from one medium into another [21]. Using the calculated imaginary and real parts of the dielectric function as a function of frequency, the refractive index $n(\omega)$ is calculated by the relation:

$$\mathbf{n}(\omega) = \left[\frac{\varepsilon_1(\omega)}{2} + \sqrt{\frac{\varepsilon_1^2(\omega) + \varepsilon_2^2(\omega)}{2}} \right]^{\frac{1}{2}} \quad (\text{III.9})$$

For low frequencies ($\varepsilon \approx 0$) the relation becomes:

$$\mathbf{n}(0) = \sqrt{\varepsilon(0)} \quad (\text{III.10})$$

The value of the static refractive index $n(0)$ of $\text{Rb}_2\text{AgSb}(\text{Cl}_{1-x}\text{Br}_x)_6$ alloys is listed in the table III.4

$\text{Rb}_2\text{AgSb}(\text{Cl}_{1-x}\text{Br}_x)_6$	E_g (eV)	$\epsilon_1(\omega)$	$n(\omega)$	$k(\omega)$
X= 0	2.55	3.63	1.89	4.13
Other calc	/	3.17 [8]	1.78 [8]	/
X= 0.25	2.50	3.68	1.92	2.76
X= 0.5	2.30	3.73	1.95	2.66
X= 0.75	2.18	4.19	2.06	2.49
X=1	2.09	4.68	2.16	2.42
Other calc	/	4.05 [8]	2.01 [8]	/

Table III.4: Calculated direct bandgap and optical parameters for $\text{Rb}_2\text{AgSb}(\text{Cl}_{1-x}\text{Br}_x)_6$ alloys.

The static refractive index calculation for pure $\text{Rb}_2\text{AgSbCl}_6$, a crucial parameter for optoelectronic applications, yields a value of 1.89. This number is similar to the 1.78 refractive index that was measured [8]. Also, the extinction coefficient $k(\omega)$ remains at zero up to 4.13 eV for pure $\text{Rb}_2\text{AgSbCl}_6$, indicating its peak in the UV region. But when Br atoms are added in place of Cl atoms with different concentrations, it yields new peaks, thereby improving the optical response.

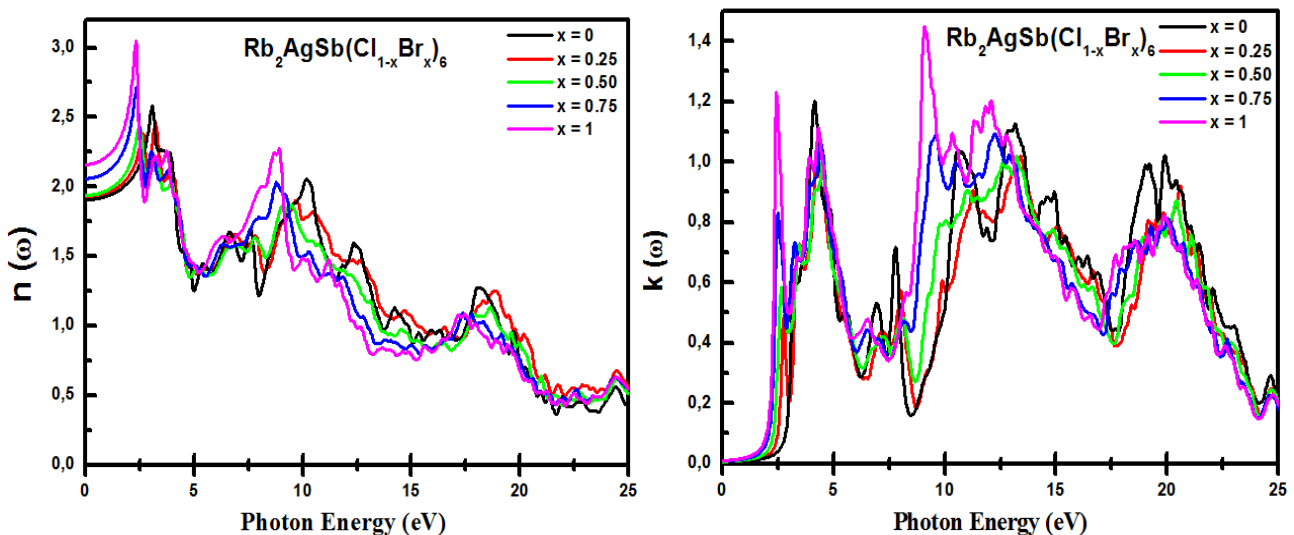


Figure III.6: The calculated refractive index $n(\omega)$, extinction coefficient $k(\omega)$ for $\text{Rb}_2\text{AgSb}(\text{Cl}_{1-x}\text{Br}_x)_6$ alloys.

III.5.3 Optical reflectivity

Reflectivity is defined as the ratio of the intensity of the reflected light to the intensity of the incident light when an electromagnetic wave strikes the surface perpendicularly. It depends on the refractive index and is described by the following equation:

$$R(\omega) = \left[\frac{\varepsilon(\omega)^{\frac{1}{2}} - 1}{\varepsilon(\omega)^{\frac{1}{2}} + 1} \right]^2 \quad (\text{III.11})$$

The average reflectance $R(\omega)$ at $E=0$ eV is approximately 15.5%, 23.8%, 24.2%, 25.6%, and 34.2% for Br concentrations of 0%, 25%, 50%, 75%, and 100%, respectively. The $R(\omega)$ spectra display a peak in the ultraviolet (UV) range, which becomes more pronounced as the Br concentration increases.

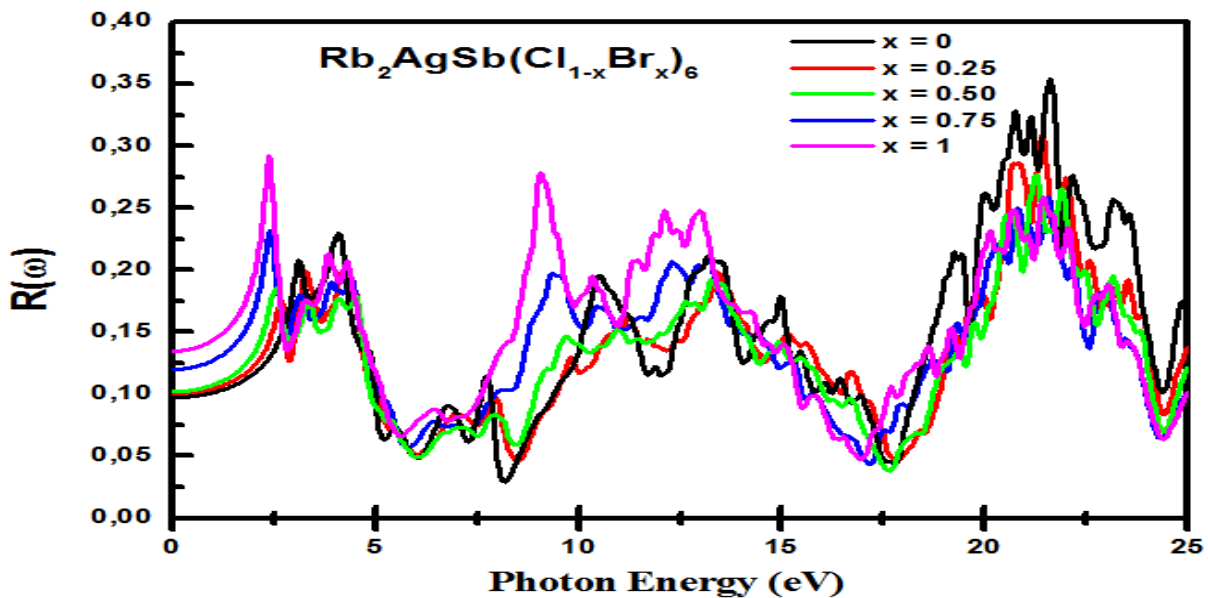


Figure III.7: The calculated reflectivity coefficient $R(\omega)$ of $\text{Rb}_2\text{AgSb}(\text{Cl}_{1-x}\text{Br}_x)_6$ alloys

III.5.4 Absorption

The absorption coefficient α , which depends on frequency, represents the fraction of light absorbed per unit length within a given medium. The following relation describes the change in the absorption coefficient with respect to photon energy $h\nu$ [24]:

$$\alpha = A(h\nu - E_g)^r \quad (\text{III.12})$$

Where A is a constant, E_g is the "optical" gap energy, and r is an index which can be equal to $\frac{1}{2}$ (for a direct gap) or 2 (for an indirect gap).

The absorption spectrum calculated for $\text{Rb}_2\text{AgSb}(\text{Cl}_{1-x}\text{Br}_x)_6$ is depicted in Fig. 8. The optical absorption data for the $\text{Rb}_2\text{AgSb}(\text{Cl}_{1-x}\text{Br}_x)_6$ alloys (refer to Table 04) clearly show the onset of direct transitions. This indicates that increasing the Br concentration significantly improves sunlight absorption in the visible range, In addition, the square of the absorption coefficient versus photon energy is plotted (i.e., $(\alpha h\nu)^2$ versus $h\nu$) for the alloys in Fig. III.9. Using linear fitting, the direct optical band gap is estimated and presented in Table 4. making these alloys excellent candidates for solar absorber applications.

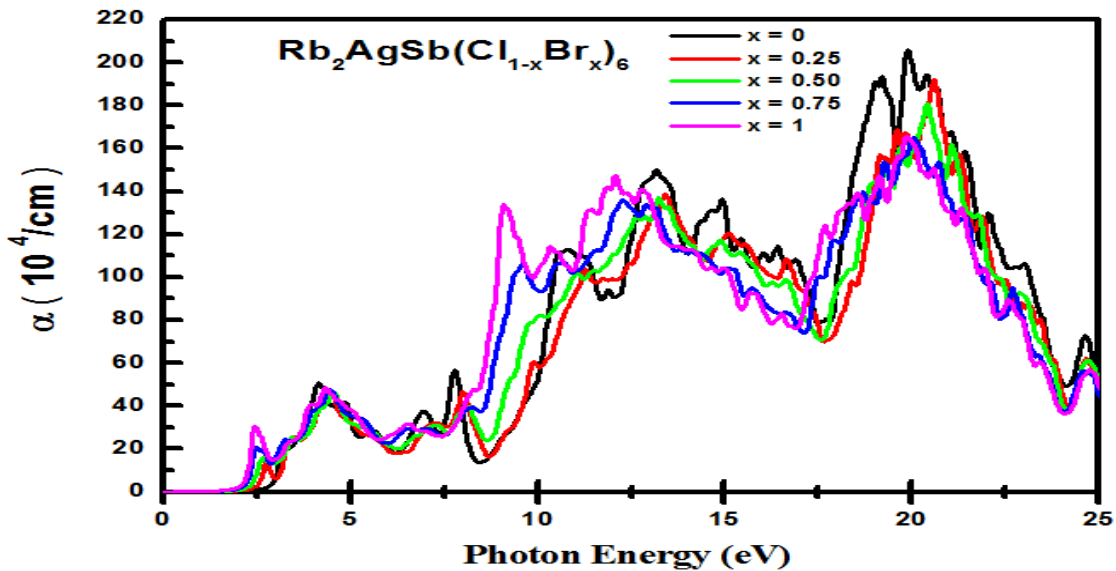


Figure III.8: The calculated absorption coefficient $\alpha(\omega)$ of $\text{Rb}_2\text{AgSb}(\text{Cl}_{1-x}\text{Br}_x)_6$ alloys

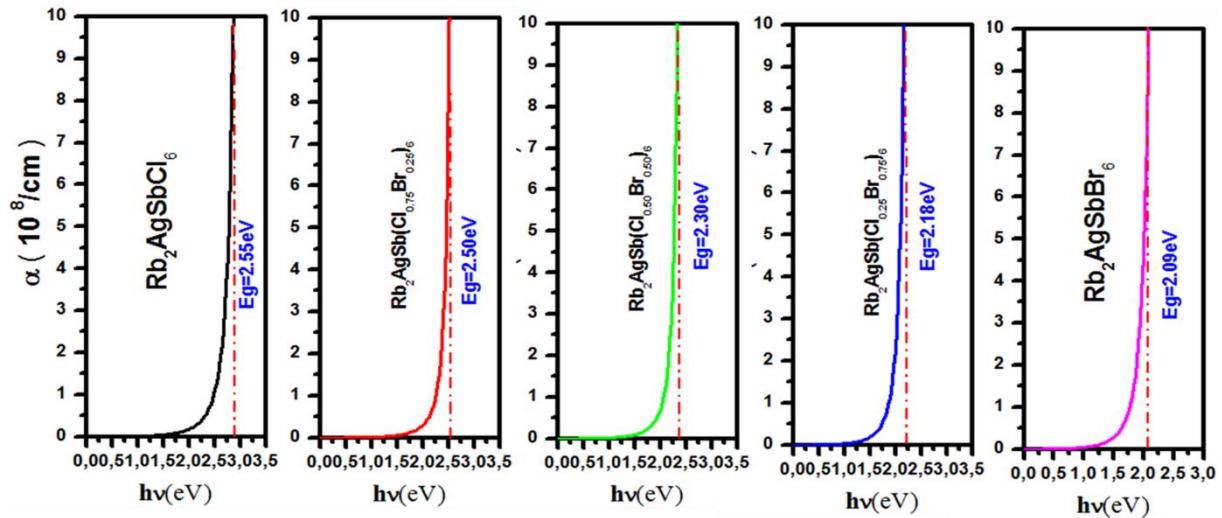


Figure.III.9: Optical band gap of $\text{Rb}_2\text{AgSb}(\text{Cl}_{1-x}\text{Br}_x)_6$ alloys.

III.6 Impact of Thickness and Temperature on Optoelectronic Performance (SLME)

Figure 9 illustrates the absorption spectrum of $\text{Rb}_2\text{AgSb}(\text{Cl}_{1-x}\text{Br}_x)_6$, while Table 5 summarizes the calculated SLMEs for these alloys, assuming an optimal layer thickness of 100 nm. The results are compared with other recently reported efficient lead-free halide perovskites, showing good alignment with materials from the same family [40]. It is worth noting that the large, indirect band gaps in this series have a significant impact on their SLME. Among them, $\text{Rb}_2\text{AgSb}(\text{Cl}_{50}\text{Br}_{50})_6$ stands out with a promising SLME of 9.51, making it a strong candidate for solar cell applications.

Additionally, Figure 9 depicts the SLME as a function of temperature, ranging from 200 K to 450 K. At room temperature (300 K), the same material with 50% Br content maintains high performance, achieving an SLME of 10.29. However, the SLME declines as the temperature increases.

$\text{Rb}_2\text{AgSb}(\text{Cl}_{1-x}\text{Br}_x)_6$	SLME%
X=0	2.06
X=25	8.41
X=50	9.51
X=75	8.71
X=100	7.83
Cs ₂ AgBiBr ₆ (Other calc)	7.92 [25]
Cs ₂ AgBiCl ₆ (Other calc)	3.90[25]

Table III.5: Calculated spectroscopic limited maximum efficiencies for $\text{Rb}_2\text{AgSb}(\text{Cl}_{1-x}\text{Br}_x)_6$ alloys

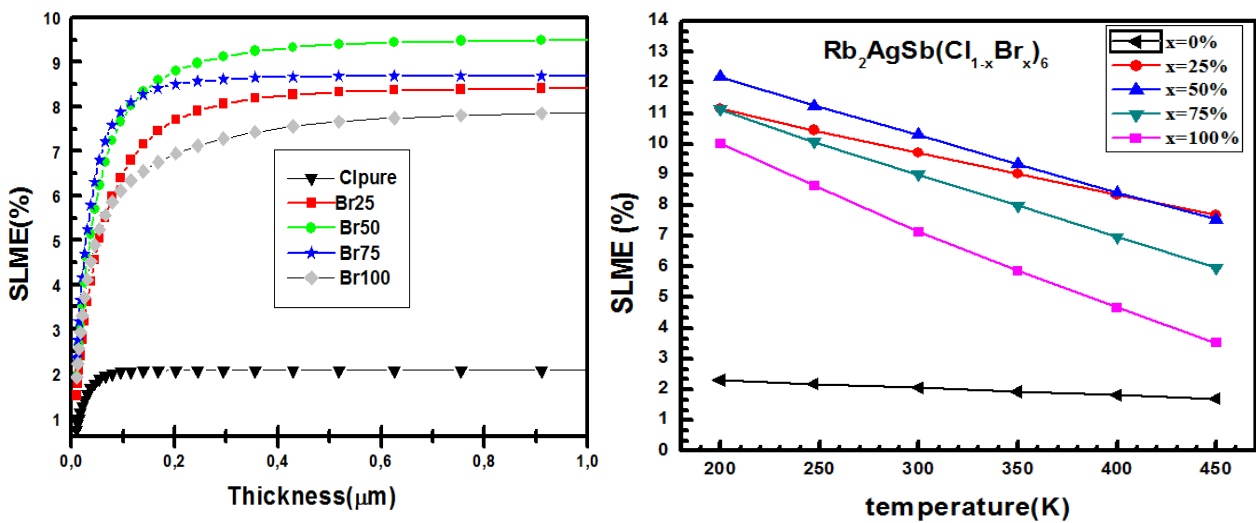


Figure III.10: The SLME for $\text{Rb}_2\text{AgSb}(\text{Cl}_{1-x}\text{Br}_x)_6$ alloys as a function of temperature and film thickness.

III.7 Thermoelectric characteristics of $\text{Rb}_2\text{AgSb}(\text{Cl}_{1-x}\text{Br}_x)_6$ alloys

III.7.1 Introduction

Discovering clean, non-polluting energy sources is a key challenge for modern societies. One promising solution is generating electricity from waste heat through

thermoelectric conversion devices utilizing the Seebeck effect, which we will explore later as a potential source of clean energy.

Thermoelectric devices enable direct conversion between heat and electricity [26-27]. Unlike traditional motors, thermoelectric generators operate without moving parts. Heat flow drives charge carriers directly, resulting in a compact, silent device that requires minimal maintenance, produces no vibrations, and can function reliably over long periods.

Additionally, unlike conventional generators that generate heat from combustion or radioactive decay, thermoelectric generators are eco-friendly, utilizing renewable heat from industrial or automotive waste [28]. The various manifestations of the thermoelectric effect, such as Seebeck, Peltier, and Thomson, which were discovered in 1821, 1834, and 1851, respectively, link a flow of heat to a flow of electric charges circulating simultaneously in a material [29-30].

III.7.2 Thermoelectric effects

The various manifestations of the thermoelectric effect, such as Seebeck, Peltier, and Thomson, which were discovered in 1821, 1834, and 1851, respectively, link a flow of heat to a flow of electric charges circulating simultaneously in a material [29-30].

III.7.2.1 Seebeck effect

Involves generating a voltage (ΔV) when a temperature difference (ΔT) is applied across the junctions of two different materials, A and B.

$$\Delta V = S_{AB}\Delta T \quad (\text{III.13})$$

The thermoelectric coefficient S_{AB} , also called thermoelectric power, is defined as the difference between the absolute Seebeck coefficients of materials A and B:

$$S_{AB} = S_A - S_B \quad (\text{III.14})$$

The dominant charge carriers determine the sign of the Seebeck coefficient: $S_{AB} < 0$ for electrons (n-type material) and $S_{AB} > 0$ for holes (p-type material).

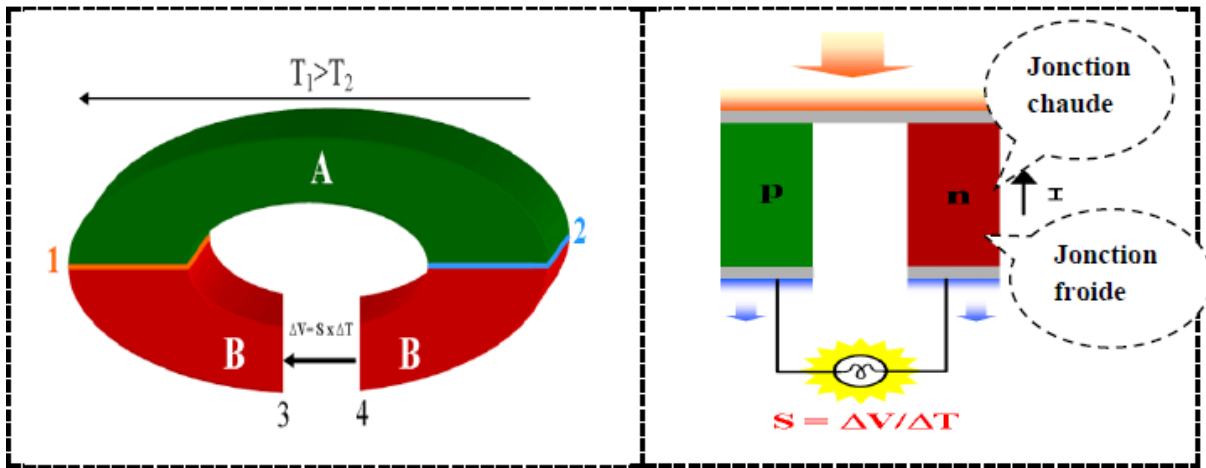


Figure III.11: Schematic diagram of the Seebeck effect [29].

III.7.2.2 Peltier effect

When a current I flows through a circuit of two materials, it drives heat transfer Q between the junctions: the cold junction absorbs heat, while the hot junction releases it. This heat transport caused by electric current is known as the Peltier effect [30].

$$Q = \Pi_{AB} \quad (III.15)$$

Where Π_{AB} represents the relative Peltier coefficient of materials A and B.

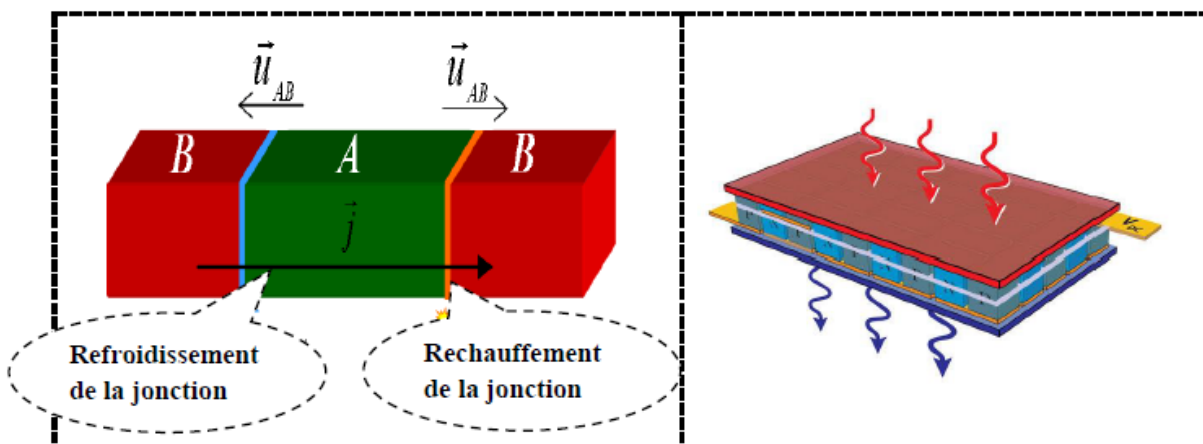


Figure III.12: Diagram explaining the Peltier effect [29].

III.7.2.3 Thomson effect

Consider a rod of a single material with a current I flowing through it and a temperature gradient ΔT . In this scenario, the material absorbs or releases heat dQ , and the Thomson effect links this heat to the electric current and thermal gradient as follows:

$$dQ = \tau I \Delta T \quad (\text{III.16})$$

Where τ is the Thomson coefficient, which, by convention, is positive if the material, absorbs heat when a current flows through it from the hot end to the cold end.

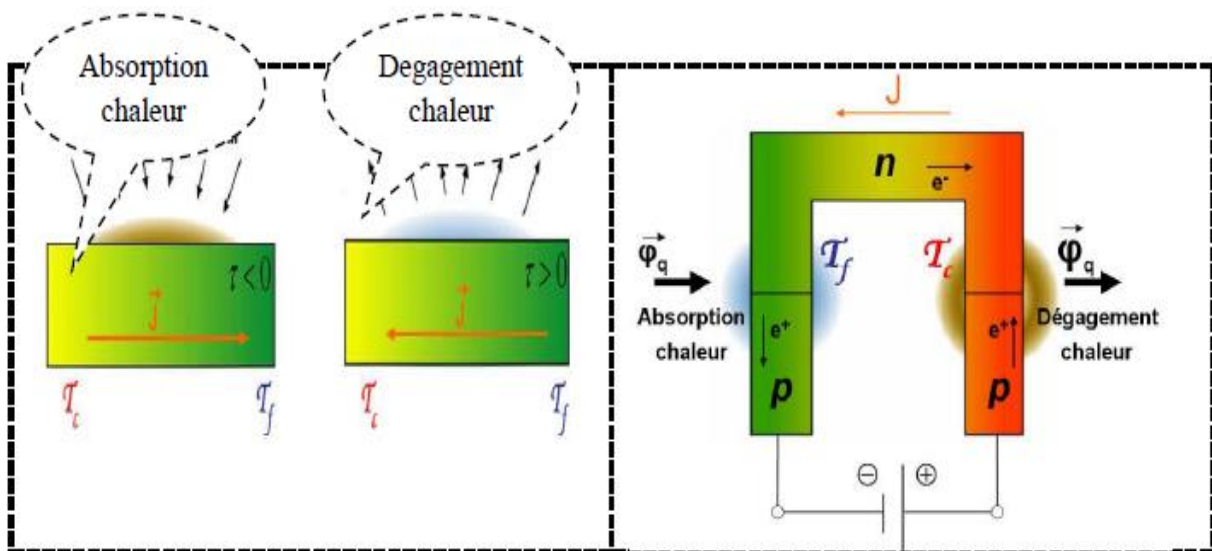


Figure III.13: Schematic diagram of the Thomson effect [29].

III.8 Thermoelectric energy conversion

The Seebeck and Peltier effects demonstrate the bidirectional conversion between thermal and electrical energy. The Seebeck effect generates voltage and electric current from a temperature gradient, while the Peltier effect creates a temperature gradient using an electric current. These principles enable thermoelectric devices to function as power generators or refrigeration systems, depending on the conversion direction.

III.8.1 Power generation

An electric potential can therefore be created by applying a temperature gradient to two ends of a material (Seebeck effect) and, by connecting a charge between these two ends to close the circuit, an electric current is established (Fig.

I.4a). As the sign of the electrical potential is a function of the type of material (p or n) and the sign of ΔT , it is possible to increase the electrical potential by connecting two materials, one of type n and the other of type p, electrically in series and thermally in parallel (Fig. III.13.b). This two-leg configuration (of n and p types) forms a thermocouple, which is the basic building block of thermoelectric devices. In fact, a thermoelectric module is obtained by connecting several thermocouples, always electrically in series and thermally in parallel, thereby further increasing the potential and hence the electric current. These modules are therefore used to produce TEG (Thermo Electric Generator) thermoelectric generators.

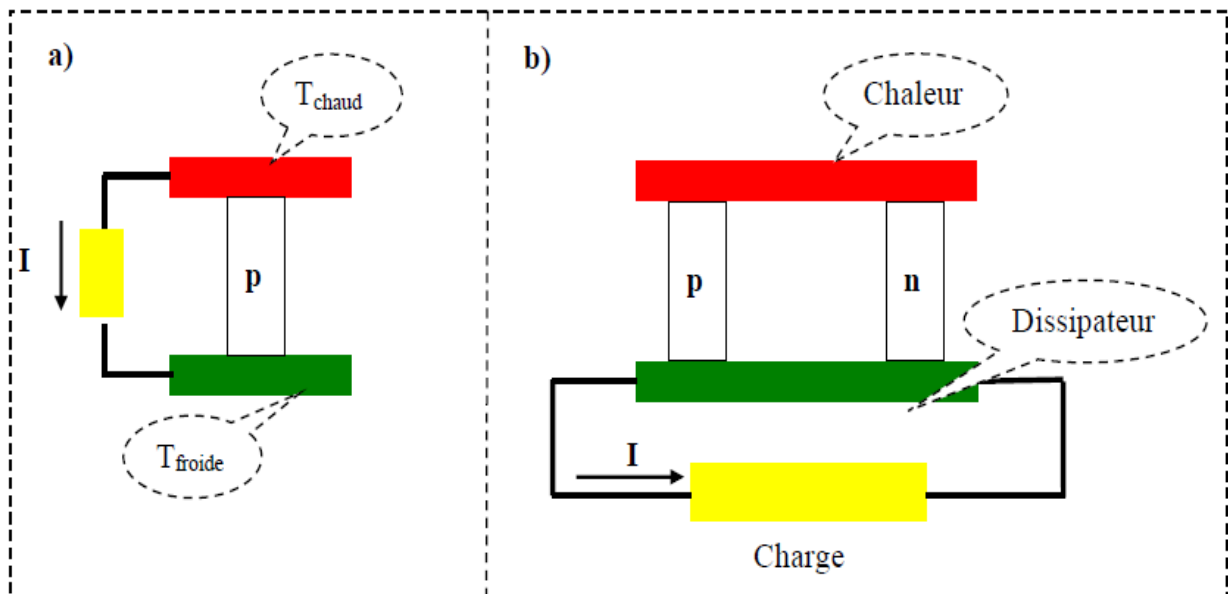


Figure III.14: Schematic diagram of a thermoelectric branch (a), a thermocouple (b) and a thermoelectric module (c) [31].

Applications:

Thermoelectric generators (TEGs), based on the aforementioned principle, have long been used to generate electrical power, with a wide range of outputs from a few microwatts to several kilowatts, by exploiting various available heat sources [32]. Notable examples include wood-fired ovens equipped with integrated thermoelectric modules, capable of generating a few tens of watts of electricity [33]. With regard to

low-power sources, an illustrative example is watches marketed by Seiko (1998, Japan), which take advantage of the small temperature difference between the environment and the human body to produce around $22 \mu\text{W}$, enough power to drive the watch mechanism [34, 35].

III.8.2 Effect of Cooling on Crystal Structure

Thermoelectric cooling provides similar benefits to generators, particularly the absence of refrigerant liquids or gases, making it an environmentally friendly solution [36,37]. Due to their compact design, these cooling systems enable localized cooling by placing the cooler directly near the component that needs to be cooled, enhancing the system's dynamic performance [38]. Various thermoelectric module-based devices are currently available on the market for a range of applications, including domestic use (portable refrigerators, Fig. III.13.a), automotive (locally cooled seats, Fig. III.13.b), electronics (active and targeted cooling of microprocessors), and optoelectronics (cooling of laser diodes, Fig. I.6c) [39, 40].

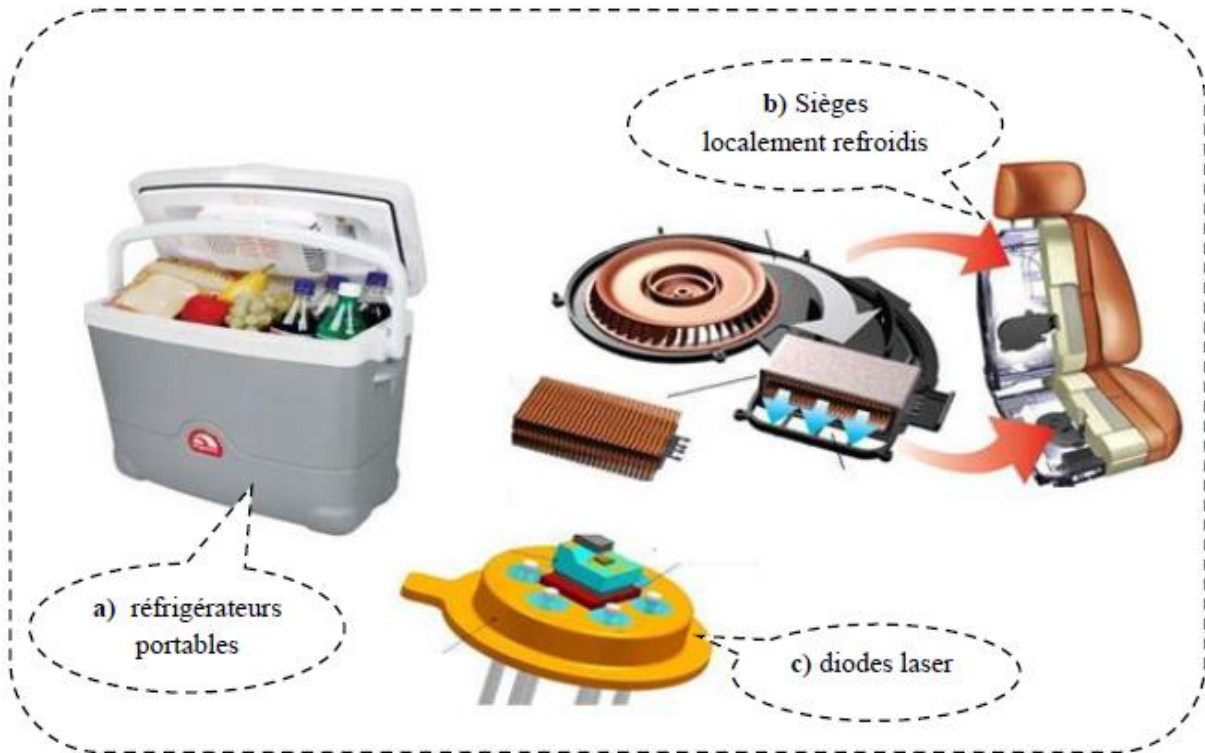


Figure III.15: Cooling applications based on thermoelectric modules.

III.9 Thermoelectric properties

IV.9.1 Calcul details

To simulate the $\text{Rb}_2\text{AgSb}(\text{Cl}_{1-x}\text{Br}_x)_6$ alloy with x ranging from 0 to 1, we utilized a $1 \times 1 \times 1$ supercell consisting of 40 atoms in the primitive unit cell. For thermoelectric property calculations, we employed a k-point grid with 100,000 points.

III.9.2 Seebeck coefficient

The Seebeck coefficient calculated for the two compounds as a function of temperature is shown in Figure III.10. As the Seebeck coefficient is proportional to the effective mass:

$$S = \frac{8\pi k_B T}{3eh} m^* \left(\frac{\pi}{3n}\right)^{2/3} \quad (\text{III.17})$$

Where m represents the carrier mass and e denotes the carrier charge, allowing the determination of the charge carrier density n . It is acknowledged that the equation is valid for systems lacking significant electronic correlations. Mott's formula demonstrates that the Seebeck coefficient is influenced by carrier concentration, effective mass, and temperature. It describes the process of electron hopping between localized states near the conduction band minima and provides an accurate explanation of the interactions between independent electrons and static impurities. **Figure III.16** illustrates how the Seebeck coefficient (S) varies with temperature. The graph reveals that S remains positive across all temperatures, indicating that holes are the primary charge carriers and the conduction is of p-type. It is well known that an increase in effective mass and the narrowing of the gap between the two conduction bands lead to higher Seebeck coefficient values. For $\text{Rb}_2\text{AgSbCl}_6$, these values reach approximately $210 \mu\text{V/K}$ at 200 K. However, the Seebeck coefficient decreases as the temperature rises.

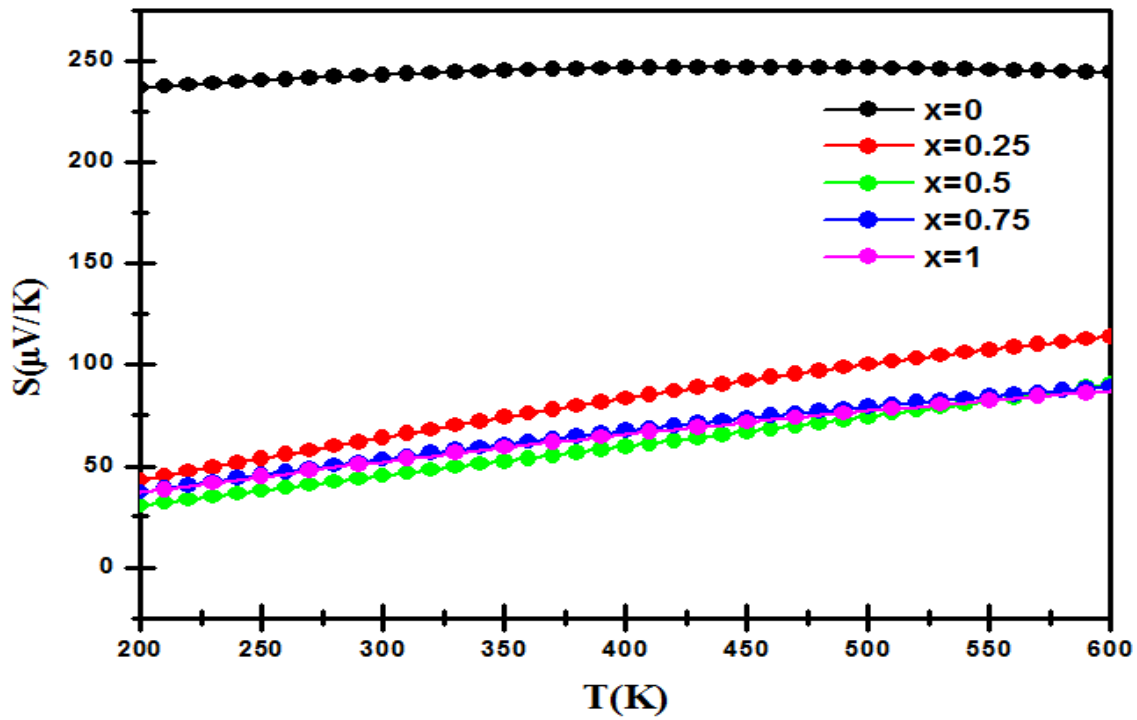


Figure III.16: Seebeck coefficient of $\text{Rb}_2\text{AgSb}(\text{Cl}_{1-x}\text{Br}_x)_6$ alloys as a function of temperature

III.9.3 Relaxation time

The BoltzTraP code represents the electrical conductivity and electronic thermal conductivity as the ratios σ/τ and κ_e/τ , where τ is the relaxation time dependent on temperature. In this study, the relaxation time was determined using the Drude model, which showed a proportional relationship with both the Seebeck coefficient and temperature, as described by the equations:

$$\tau = A \frac{qsh}{k_B^2 T} \quad (\text{III.18})$$

Where A are dimensionless coefficients ($A = 1$ for metals and $A = 0.1$ for semiconductors), q are the carriers (electrons or holes), the Seebeck coefficient S , the white constant h , the Boltzmann constant k_B and the absolute temperature T . **Figure III.17** illustrates that the relaxation times for $\text{Rb}_2\text{AgSb}(\text{Cl}_{1-x}\text{Br}_x)_6$ decrease as the temperature rises across all compounds.

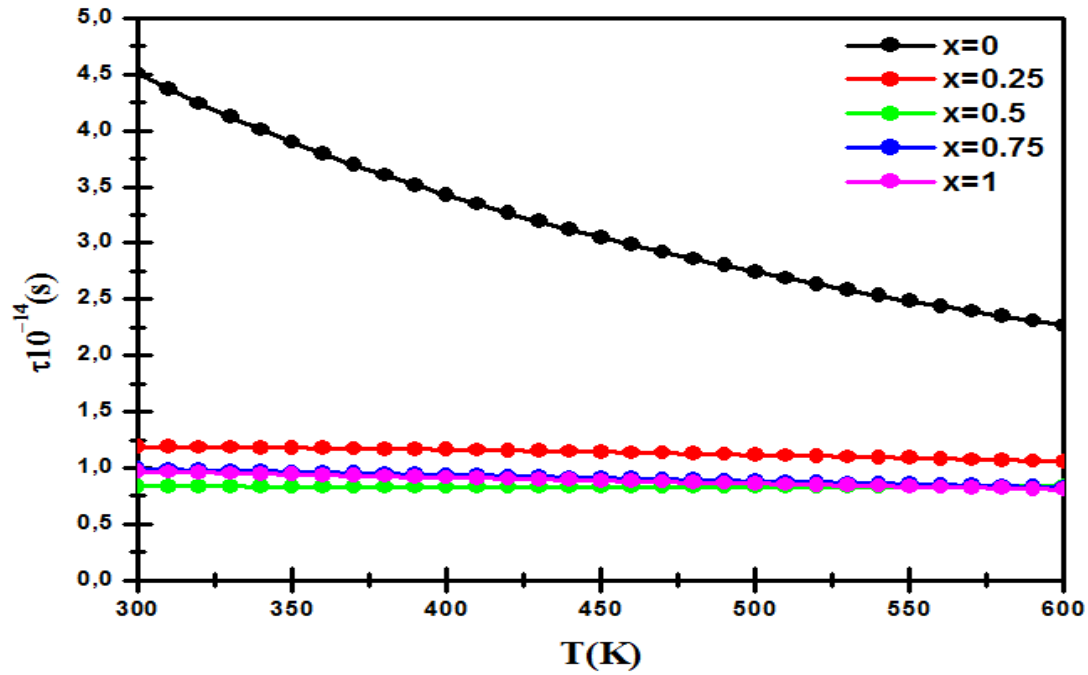


Figure III.17: The relaxation time calculated for $\text{Rb}_2\text{AgSb}(\text{Cl}_{1-x}\text{Br}_x)_6$ alloys.

III.9.4 Electrical conductivity and electronic thermal conductivity

Electrical conductivity is influenced by both the number of charge carriers and their mobility. **Figure III.18** presents the electrical conductivity (σ/τ), expressed in units of $(\Omega \cdot \text{ms})^{-1}$, for a double perovskite as a function of temperature in the range of 200–600 K. The conductivity depends on both the carrier concentration and their mobility. A nearly linear increase in σ/τ is observed with rising temperature, indicating enhanced carrier transport at higher thermal energy. At 200 K, the electrical conductivities (σ/τ) for $\text{Rb}_2\text{AgSbCl}_6$ and $\text{Rb}_2\text{AgSbBr}_6$ are $0.122 \times 10^{19} (\Omega \cdot \text{ms})^{-1}$ and $3.81 \times 10^{19} (\Omega \cdot \text{ms})^{-1}$, respectively. The higher σ value for $\text{Rb}_2\text{AgSbBr}_6$ compared to $\text{Rb}_2\text{AgSbCl}_6$ is likely due to a reduction in the band gap.

Moreover, the electronic component of thermal conductivity (κ_e/τ) is calculated using the BoltzTraP code. **Figure III.19** shows the variation of κ_e/τ with temperature. This quantity increases with temperature because more charge carriers become thermally activated. At 300 K, the conductivity values are $0.136 \times 10^{14} \text{ W/m} \cdot \text{K} \cdot \text{s}$ for $\text{Rb}_2\text{AgSbCl}_6$ and $1.77 \times 10^{14} \text{ W/m} \cdot \text{K} \cdot \text{s}$ for $\text{Rb}_2\text{AgSbBr}_6$. For thermoelectric applications, $\text{Rb}_2\text{AgSbCl}_6$ —with its lower electronic thermal conductivity—is more suitable compared to $\text{Rb}_2\text{AgSbBr}_6$.

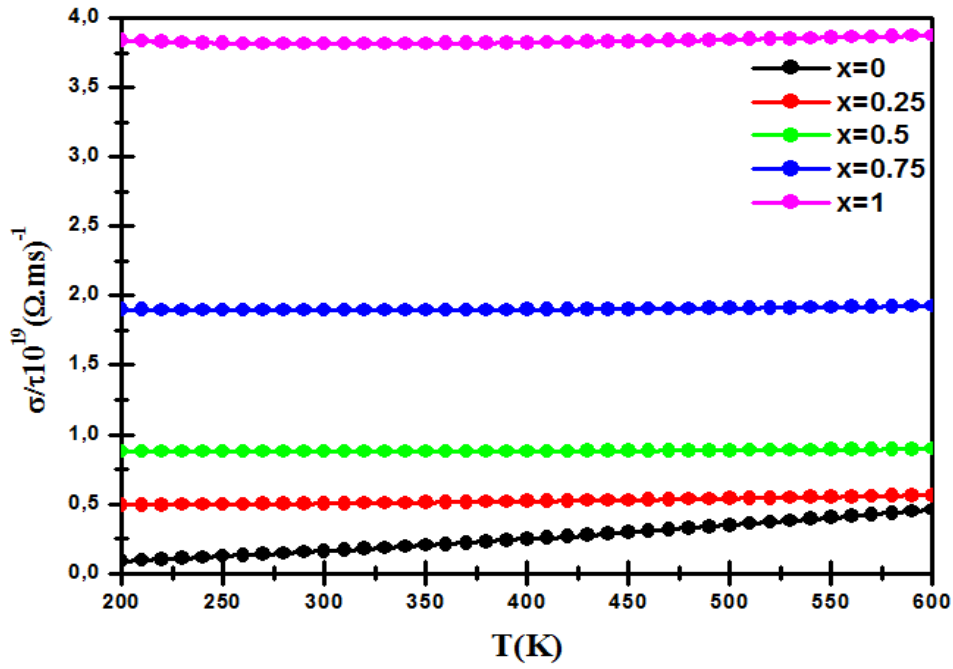


Figure III.18: Electrical conductivity as a function of temperature for $\text{Rb}_2\text{AgSb}(\text{Cl}_{1-x}\text{Br}_x)_6$ alloys.

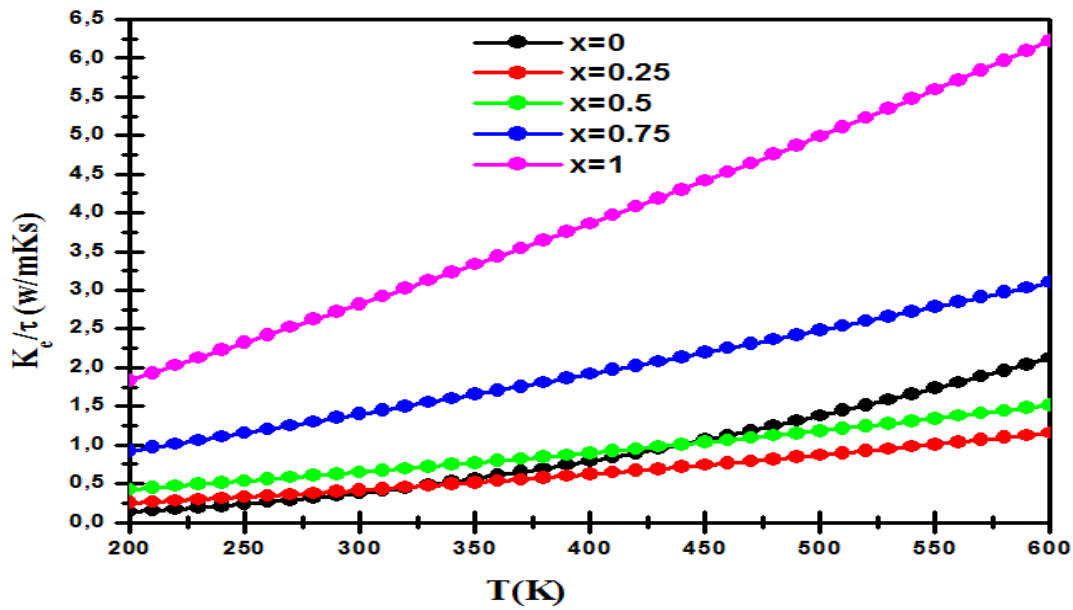


Figure III.19: Electronic thermal conductivity as a function of temperature for $\text{Rb}_2\text{AgSb}(\text{Cl}_{1-x}\text{Br}_x)_6$ alloys.

The calculated power factor ($\text{PF} = S^2\sigma$) as a function of temperature (T) for $\text{Rb}_2\text{AgSb}(\text{Cl}_{1-x}\text{Br}_x)_6$ is presented in **Figure III.20**. The power factor increases with temperature for all values of x , indicating that the material becomes more efficient at converting heat into electricity as the temperature rises. This trend suggests that the material may be well-suited for high-temperature thermoelectric applications. At $x = 1$ and $T = 600$ K, the power factor reaches $2.93 \text{ mW/m}\cdot\text{K}^2$, while at $x = 0.5$, the power factor is the lowest among all compositions.

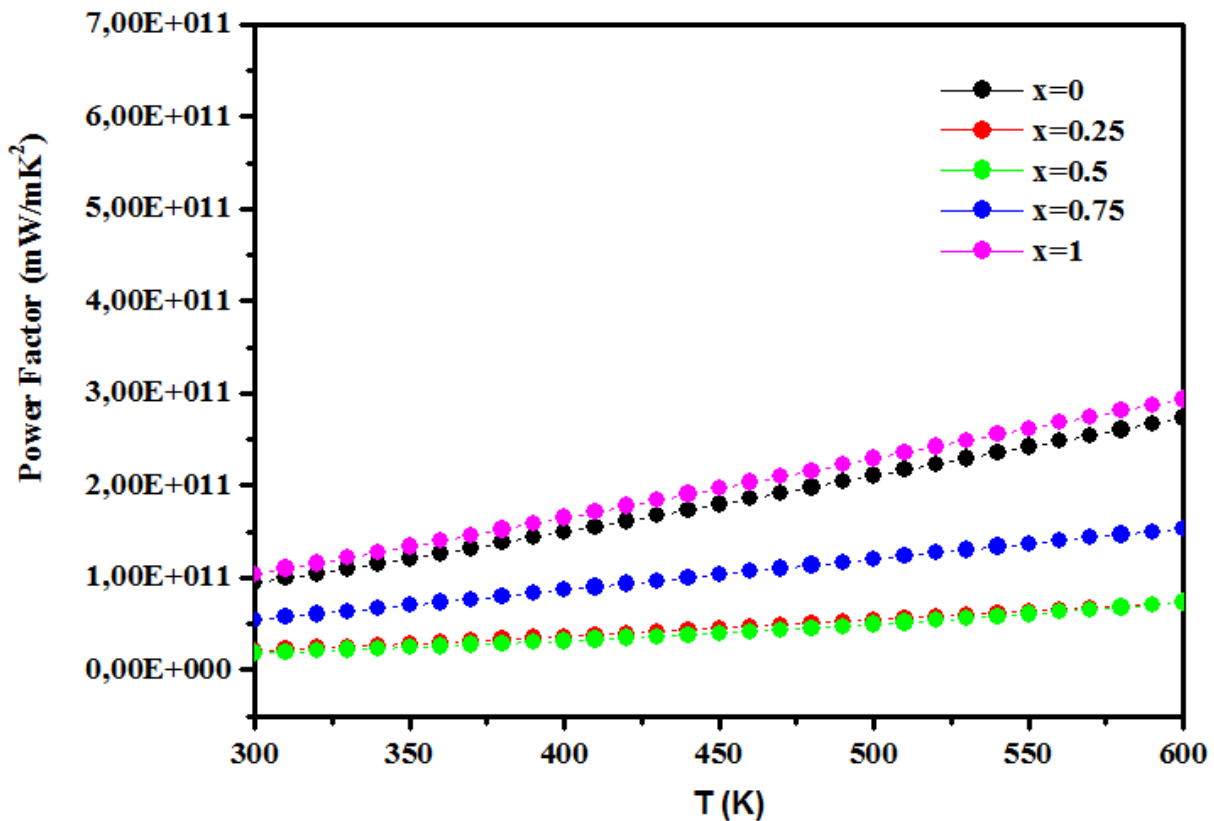


Figure III.20: Variation of power factor as a function of temperature for $\text{Rb}_2\text{AgSb}(\text{Cl}_{1-x}\text{Br}_x)_6$ alloys.

III.9.5 Optimization of merit factor ZT

The performance of thermoelectric materials is quantified by a dimensionless quantity called the figure of merit, ZT , given by:

$$ZT = \sigma S^2 T / \kappa. \tag{III.19}$$

Where: T : absolute temperature [K]

S : Seebeck coefficient or thermoelectric power [V/K]

σ : electrical conductivity [$\Omega^{-1}\cdot\text{m}^{-1}$]

κ : thermal conductivity ($\kappa = \kappa_e + \kappa_l$) [$\text{W}\cdot\text{m}^{-1}\cdot\text{K}^{-1}$]

Where: κ_e is the electronic thermal conductivity due to the movement of charge carriers, and

κ_l is the lattice thermal conductivity due to phonons.

Optimizing materials for thermoelectric energy conversion requires optimizing their electrical and thermal transport properties to maximize ZT . According to this formula, a good thermoelectric material exhibits a high Seebeck coefficient, good electrical conductivity, and low thermal conductivity. However, increasing σ by raising the carrier concentration generally leads to a decrease in the magnitude of S and an increase in κ . Therefore, a compromise must be found between these conflicting parameters.

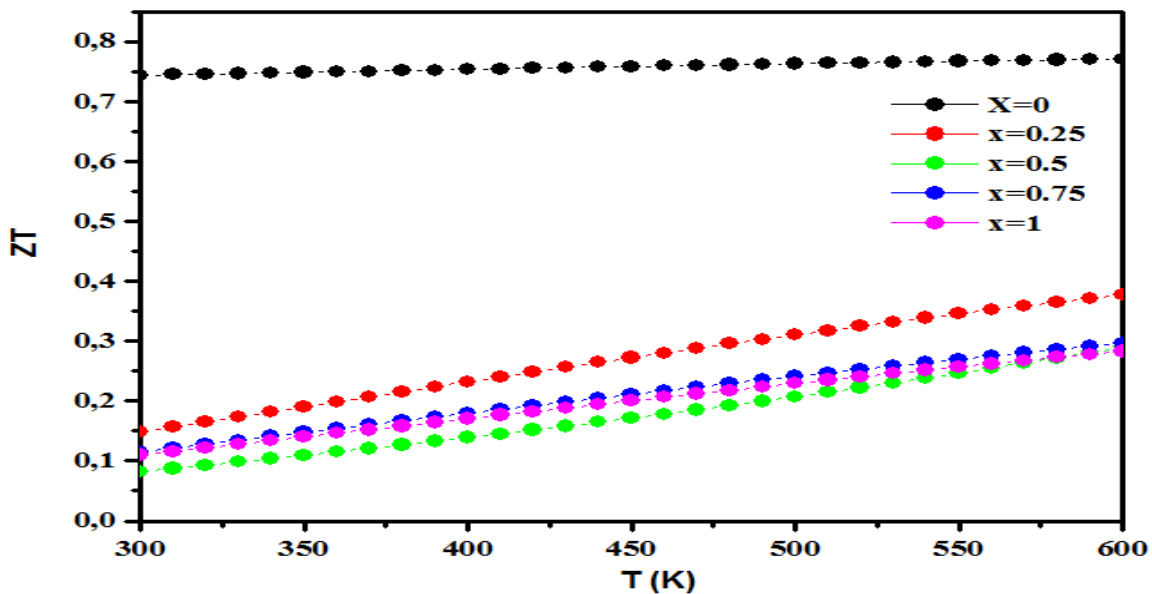


Figure III.21: Variation of ZT merit factor with temperature for $\text{Rb}_2\text{AgSb}(\text{Cl}_{1-x}\text{Br}_x)_6$ alloys.

In **Figure III.21**, the calculated ZT values for solid solutions of $\text{Rb}_2\text{AgSb}(\text{Cl}_{1-x}\text{Br}_x)_6$ are presented as a function of temperature, ranging from 300 K to 600 K. As previously reported, two key conditions must be met for good thermoelectric performance: a high power factor (PF) and low thermal conductivity (κ). As shown, for the pure compound, ZT increases with temperature, reaching a value of 0.77, which suggests a stable and efficient performance across the temperature range. With increasing Br content, ZT values decrease, though they still demonstrate thermoelectric potential, particularly at elevated temperatures. Therefore, $\text{Rb}_2\text{AgSbCl}_6$ emerges as the most promising composition among those studied. However, substituting Br for Cl generally reduces ZT, although the material retains its thermoelectric behavior.

III.10 Conclusion

In this section, we investigated how the substitution of bromine affects the band gap energy and optical properties of the lead-free halide perovskite $\text{Rb}_2\text{AgSbCl}_6$. Density functional theory (DFT) calculations based on first principles demonstrate that replacing chloride with bromine shifts the conduction band (CB) minimum towards the Fermi level, leading to a reduction in the band gap. The band gap decreases from 2.08 eV in pure $\text{Rb}_2\text{AgSbCl}_6$ to 1.86 eV, 1.59 eV, and 1.43 eV for $\text{Rb}_2\text{AgSb}(\text{Cl}_{0.75}\text{Br}_{0.25})_6$, $\text{Rb}_2\text{AgSb}(\text{Cl}_{0.5}\text{Br}_{0.5})_6$, and $\text{Rb}_2\text{AgSb}(\text{Cl}_{0.25}\text{Br}_{0.75})_6$, respectively.

Additionally, we observed that both the hole and electron effective masses decrease with increasing Br concentration, resulting in enhanced hole and electron carrier mobility. Optical property calculations further reveal that substituting Br in $\text{Rb}_2\text{AgSbCl}_6$ improves its optical performance by narrowing the transparent region while increasing the refractive index and absorption within the visible light spectrum. The specific luminescent minority electron (SLME) of $\text{Rb}_2\text{AgSb}(\text{Cl}_{0.5}\text{Br}_{0.5})_6$ is 9.51%. Although this percentage is modest, it can be attributed to the material's indirect band gap. However, the similarity of these results to others within the same family suggests that lead-free halide perovskites remain a promising option for achieving high-efficiency solar energy conversion.

The thermoelectric (TE) properties of $\text{Rb}_2\text{AgSb}(\text{Cl}_{1-x}\text{Br}_x)_6$ alloys are investigated in detail by combining Boltzmann transport theory with first-principles band structure calculations. The maximum ZT value of 0.77 is observed for the pure compound ($x = 0$) at

T = 700 K, primarily due to the combination of reduced thermal conductivity and a high power factor. This composition exhibits the best thermoelectric performance, with the highest and most stable ZT. However, substituting Br for Cl generally leads to a reduction in ZT, although the material retains its thermoelectric behavior.

Reference

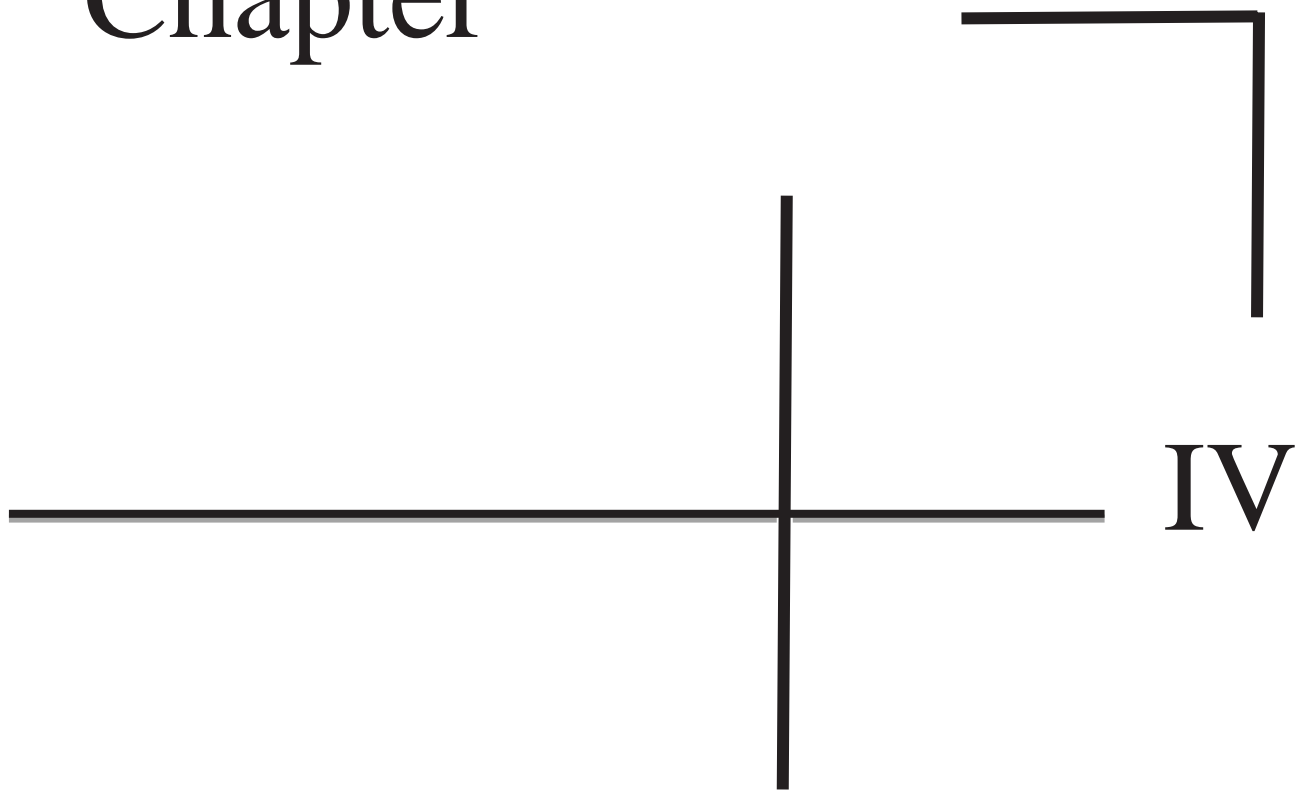
- [1] Kojima, A., Teshima, K., Shirai, Y., & Miyasaka, T. (2009). Organometal halide perovskites as visible-light sensitizers for photovoltaic cells. *Journal of the American Chemical Society*, 131(17), 6050–6051.
- [2] Deschler, F., Price, M., Pathak, S., Klintberg, L. E., Jarausch, D. D., Higler, R., ... & Friend, R. H. (2014). High photoluminescence efficiency and optically pumped lasing in solution-processed mixed halide perovskite semiconductors. *The Journal of Physical Chemistry Letters*, 5(8), 1421–1426.
- [3] Grätzel, M. (2014). The light and shade of perovskite solar cells. *Nature Materials*, 13(9), 838–842.
- [4] Yantara, N., Bhaumik, S., Yan, F., Sabba, D., Kadro, J. M., Xing, G., ... & Mathews, N. (2015). Inorganic halide perovskites for efficient light-emitting diodes. *The Journal of Physical Chemistry Letters*, 6(21), 4360–4364.
- [5] Tan, Z.-K., Moghaddam, R. S., Lai, M. L., Docampo, P., Higler, R., Deschler, F., ... & Friend, R. H. (2014). Bright light-emitting diodes based on organometal halide perovskite. *Nature Nanotechnology*, 9(9), 687–692.
- [6] Dou, L., Yang, Y. M., You, J., Hong, Z., Chang, W. H., Li, G., & Yang, Y. (2014). Solution-processed hybrid perovskite photodetectors with high detectivity. *Nature Communications*, 5, 5404.
- [7] Bao, C., Yang, J., Bai, S., Xu, W., Yan, Z., Xu, Q., ... & Zhang, W. (2018). High performance and stable all-inorganic metal halide perovskite-based photodetectors for optical communication applications. *Advanced Materials*, 30(38), 1803422.
- [8] Asghar, M., Asif, M., Rasheed, A., & Shaukat, A. (2022). A computational insight of the lead-free double perovskites $\text{Rb}_2\text{AgSbCl}_6$ and $\text{Rb}_2\text{AgSbBr}_6$ for optoelectronic and

- thermoelectric applications. *International Journal of Energy Research*, 46(15), 24273–24285.
- [9] Madsen, G. K. H., Blaha, P., Schwarz, K., Sjöstedt, E., & Nordström, L. (2001). Efficient linearization of the augmented plane-wave method. *Physical Review B*, 64, 195134.
- [10] Schwarz, K., Blaha, P., & Madsen, G. K. H. (2002). Electronic structure calculations of solids using the WIEN2k package for material sciences. *Computer Physics Communications*, 147(1–2), 71–76.
- [11] Blaha, P., Schwarz, K., Tran, F., Laskowski, R., Madsen, G. K. H., & Marks, L. D. (2020). WIEN2k: An APW+lo program for calculating the properties of solids. *The Journal of Chemical Physics*, 152(7), 074101.
- [12] Wu, Z., & Cohen, R. E. (2006). More accurate generalized gradient approximation for solids. *Physical Review B*, 73(23), 235116.
- [13] Koller, D., Tran, F., & Blaha, P. (2011). Merits and limits of the modified Becke–Johnson exchange potential. *Physical Review B*, 83(19), 195134.
- [14] Tran, F., & Blaha, P. (2009). Accurate band gaps of semiconductors and insulators with a semilocal exchange–correlation potential. *Physical Review Letters*, 102(22), 226401.
- [15] Xiao, Z., Meng, W., Wang, J., Mitzi, D. B., & Yan, Y. (2017). Intrinsic instability of $\text{Cs}_2\text{In}(\text{I})\text{M}(\text{III})\text{X}_6$ ($\text{M} = \text{Bi}, \text{Sb}$; $\text{X} = \text{Halogen}$) double perovskites: A combined density functional theory and experimental study. [Journal not specified—please provide full source for proper APA formatting].
- [16] Murnaghan, F. D. (1944). The compressibility of media under extreme pressures. *Proceedings of the National Academy of Sciences*, 30(9), 244–247.
- [17] Chung, I., Song, J.-H., Im, J., Androulakis, J., Malliakas, C. D., Li, H., ... & Kanatzidis, M. G. (2012). CsSnI_3 : Semiconductor or metal? High electrical conductivity and strong near-infrared photoluminescence from a single material. High hole mobility and phase transitions. *Journal of the American Chemical Society*, 134(20), 8579–8587.

- [18] Wei, S. H., & Zunger, A. (1998). Predicted band-gap pressure coefficients of all diamond and zinc-blende semiconductors: Chemical trends. *Physical Review B*, 60, 5404–5411.
- [19] Smith, N. V. (1971). Photoelectron energy spectra and the band structures of the noble metals. *Physical Review B*, 3(6), 1862.
- [20] Ehrenreich, H. R. P. H., & Philipp, H. R. (1962). Optical properties of Ag and Cu. *Physical Review*, 128(4), 1622.
- [21] Dressel, M., & Grüner, G. (2002). *Electrodynamics of solids: Optical properties of electrons in matter*. Cambridge University Press.
- [22] Ehrenreich, H., & Cohen, M. H. (1959). Self-consistent field approach to the many-electron problem. *Physical Review*, 115(4), 786.
- [23] Keunings, R. (2000). A survey of computational rheology. In *Proceedings of the XIIIth International Congress on Rheology (Vol. 1)*. British Society of Rheology.
- [24] Seddiki, N., Bouarissa, N., & Daoudi, S. (2013). Electronic structure, optical and dielectric constant of compounds Indium-based: InAlP_2 , and InGaP_2 in its chalcopyrite, CuPt and CuAu-I structures. *Materials Science in Semiconductor Processing*, 16(6), 1454–1465.
- [25] Savory, C. N., Walsh, A., & Scanlon, D. O. (2016). Can Pb-free halide double perovskites support high-efficiency solar cells? *ACS Energy Letters*, 1(5), 949–955.
- [26] DiSalvo, F. J. (1999). Thermoelectric cooling and power generation. *Science*, 285(5428), 703–706.
- [27] Vandaele, K., Lecoeur, P., Cagnon, L., & Boulanger, C. (2017). Thermal spin transport and energy conversion. *Materials Today Physics*, 1, 39–49.
- [28] Bell, L. E. (2008). Cooling, heating, generating power, and recovering waste heat with thermoelectric systems. *Science*, 321(5895), 1457–1461.
- [29] Nolas, G. S., Sharp, J., & Goldsmid, J. (2013). *Thermoelectrics: Basic principles and new materials developments (Vol. 45)*. Springer Science & Business Media.

- [30] Mahanti, S. D., & Hogan, T. P. (2003). Chemistry, physics, and materials science of thermoelectric materials: Beyond bismuth telluride. Springer.
- [31] Kohn, W., & Sham, L. J. (1965). Self-consistent equations including exchange and correlation effects. *Physical Review*, 140(4A), A1133.
- [32] Slater, J. C. (1964). Energy band calculations by the augmented plane wave method. In *Advances in Quantum Chemistry* (Vol. 1, pp. 35–58). Academic Press.
- [33] Blaha, P., Schwarz, K., Madsen, G. K. H., Kvasnicka, D., & Luitz, J. (2001). WIEN2k: An augmented plane wave + local orbitals program for calculating crystal properties, 60(1).
- [34] Perdew, J. P., Burke, K., & Ernzerhof, M. (1996). Generalized gradient approximation made simple. *Physical Review Letters*, 77(18), 3865–3868.
- [35] Tran, F., & Blaha, P. (2009). Accurate band gaps of semiconductors and insulators with a semilocal exchange-correlation potential. *Physical Review Letters*, 102(22), 226401.
- [36] Zhou, D., Zeng, X., Wang, X., & Liu, G. (2012). Thermal stability and elastic properties of Mg_2X (X = Si, Ge, Sn, Pb) phases from first-principles calculations. *Computational Materials Science*, 51(1), 409–414.
- [37] Liu, N.-N., Ren-Bo, S., & Da-Wei, D. (2009). Elastic constants and thermodynamic properties of $\text{Mg}_2\text{Si}_x\text{Sn}_{1-x}$ from first-principles calculations. *Chinese Physics B*, 18(5), 1979.
- [38] Zhang, J., Xu, C., Xia, L., Li, J., & Xu, Z. (2000). Microstructural development of Al-15wt.% Mg_2Si in situ composite with mischmetal addition. *Materials Science and Engineering: A*, 281(1–2), 104–112.
- [39] Zhang, Q., Huang, X. Y., Ma, C. L., & Tang, G. H. (2007). Preparation and thermoelectric properties of $\text{Mg}_2\text{Si}_{1-x}\text{Sn}_x$. *Physica Scripta*, 2007(T129), 123.
- [40] Mili, I., Miloua, F., Bouarissa, N., & Ferhat, M. (2022). A simple formula for calculating the carrier relaxation time. *Computational Materials Science*, 213, 111678.

Chapter



**Theoretical Study of a new
Double Perovskite Alloys
 $\text{Rb}_2\text{AgSb}_{1-x}\text{Bi}_x\text{X}'$ ($\text{X}' = \text{Cl},$
 Br, I) Using VASP Analysis**

IV.1 Introduction

The generation of photovoltaic energy has become essential in meeting the growing demand for clean energy and addressing the depletion of fossil fuel resources, as solar cells produce no harmful emissions. As a result, the significance of renewable, sustainable, and environmentally friendly energy sources in the global economy underscores the need to prioritize their development. This urgency has led to increased focus on various research fields, including physics, chemistry, and materials science, where both theoretical and experimental approaches are being explored [1-2].

Furthermore, the widespread adoption of solar energy necessitates the production of cost-effective solar cells. Therefore, designing and developing novel solar cell materials with optimal electronic, optical, and photovoltaic properties is a key step. This study aims to explore potential optical applications by employing Density Functional Theory (DFT) to analyze the structural and optoelectronic properties of Rb₂AgSb_{1-x}Bi_xX'₆ alloys, where (x = 0, 0.25, 0.50, 0.75, 1) and (X' = Cl, Br, and I). These compounds exhibit highly adjustable crystal structures and electrical properties, making them promising candidates for diverse applications. By incorporating different halogens (Cl, Br, and I), this research examines structural and optoelectronic variations to assess the influence of each halogen on material performance. Ultimately, the study of Rb₂AgSb_{1-x}Bi_xX'₆ (with X' = Cl, Br, and I) aims to advance the development of high-performance, environmentally friendly materials by providing deeper insights into the relationship between structure and properties in lead-free halide double perovskites.

IV.2 calculation method

The calculations of crystal structures, electronic and optical properties were performed

using density functional theory (DFT) as implemented in the Vienna Ab initio Simulation Package (VASP) [3]. The generalized gradient approximation was employed using the exchange and correlation function of Perdew, Burke, and Ernzerhof (GGA-PBE) [4]. The atomic structures were optimized using the PBE functional with 3 × 3 × 3 k-point grid for the cubic and other structured perovskites, respectively. The electronic and optical

properties were calculated using PBE and the hybrid exchange-correlation functional (HSE)[5].

IV.3 RESULTS AND DISCUSSION

IV.3.1 Electronic properties

IV.3.1.a Band structures

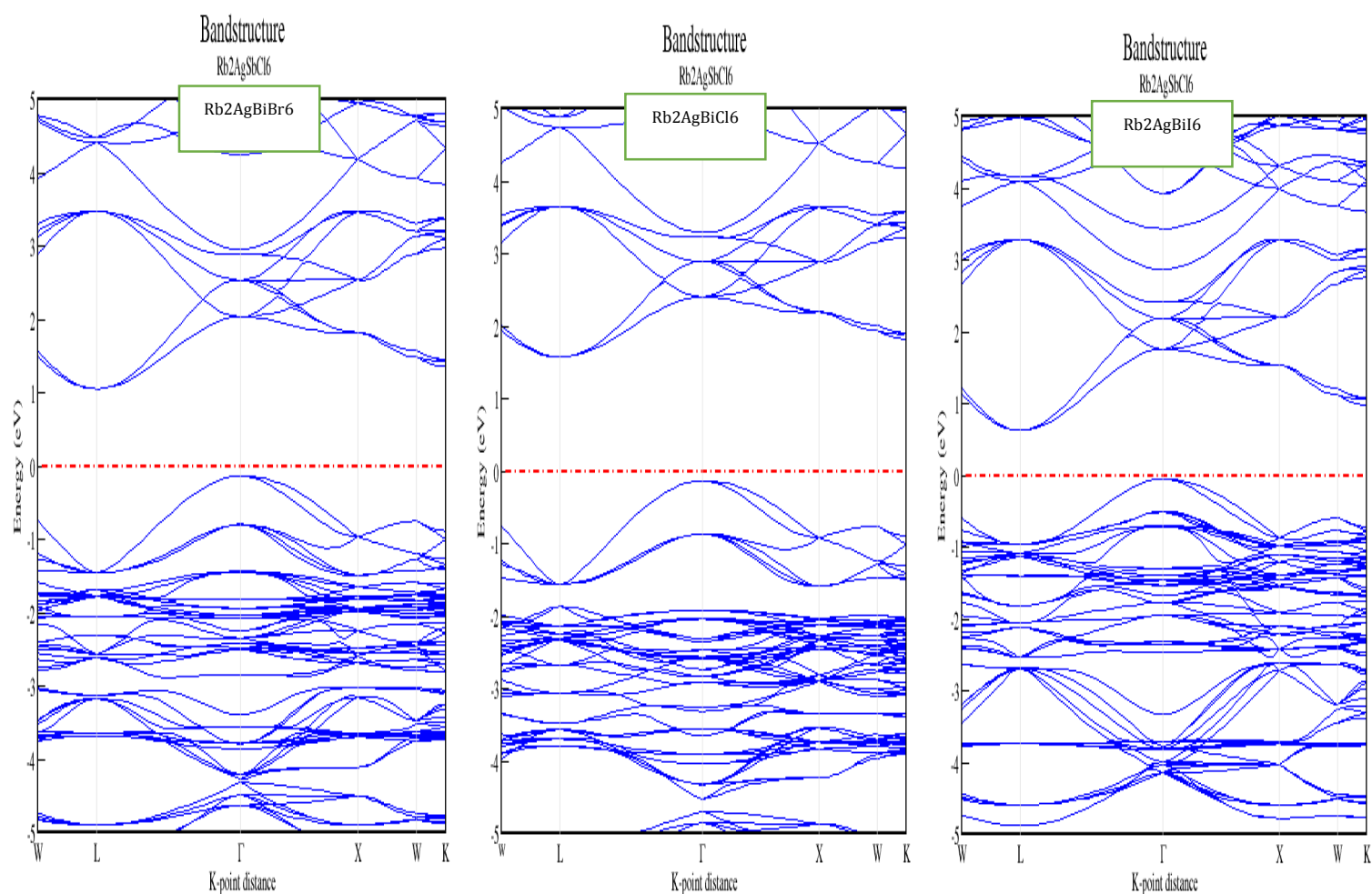
To gain a comprehensive understanding of the electronic structure of Rb₂AgSb_{1-x}Bi_xX'₆ (where X' = Cl, Br, and I), both band structures and densities of states were calculated using the PBE and HSE methods for the optimized lattice parameters. The valence band maximum (VBM) was set at 0 eV as a reference point to align energy values accordingly. Figure IV.10 presents the computed band structures of Rb₂AgSb_{1-x}Bi_xX'₆ alloys along selected high-symmetry directions in the Brillouin zone (BZ). The conduction band minimum (CBM) and the VBM are not located at the same symmetry point (L-Γ), confirming the material's nature as an indirect band gap semiconductor.

To obtain more accurate band gap values, the HSE approach was applied, yielding results (Table IV.1) that align with existing theoretical studies [6]. It was observed that substituting Sb with Bi alters both the band gap characteristics and the semiconductor behavior. Additionally, modifying the halogen component significantly affects the band gap values, with Br yielding favorable results. The CBM shifts downward towards the Fermi level, reducing the band gap of Rb₂AgSb_{1-x}Bi_xBr₆ alloys to 1.32 eV, 1.39 eV, 1.61 eV, 1.59 eV, and 1.04 eV for x = 0.25, 0.5, 0.75, and 1, respectively. Furthermore, the introduction of I influences the band structure, further decreasing the energy band gap of Rb₂AgSb_{1-x}Bi_xI alloys, as shown in Table IV.1.

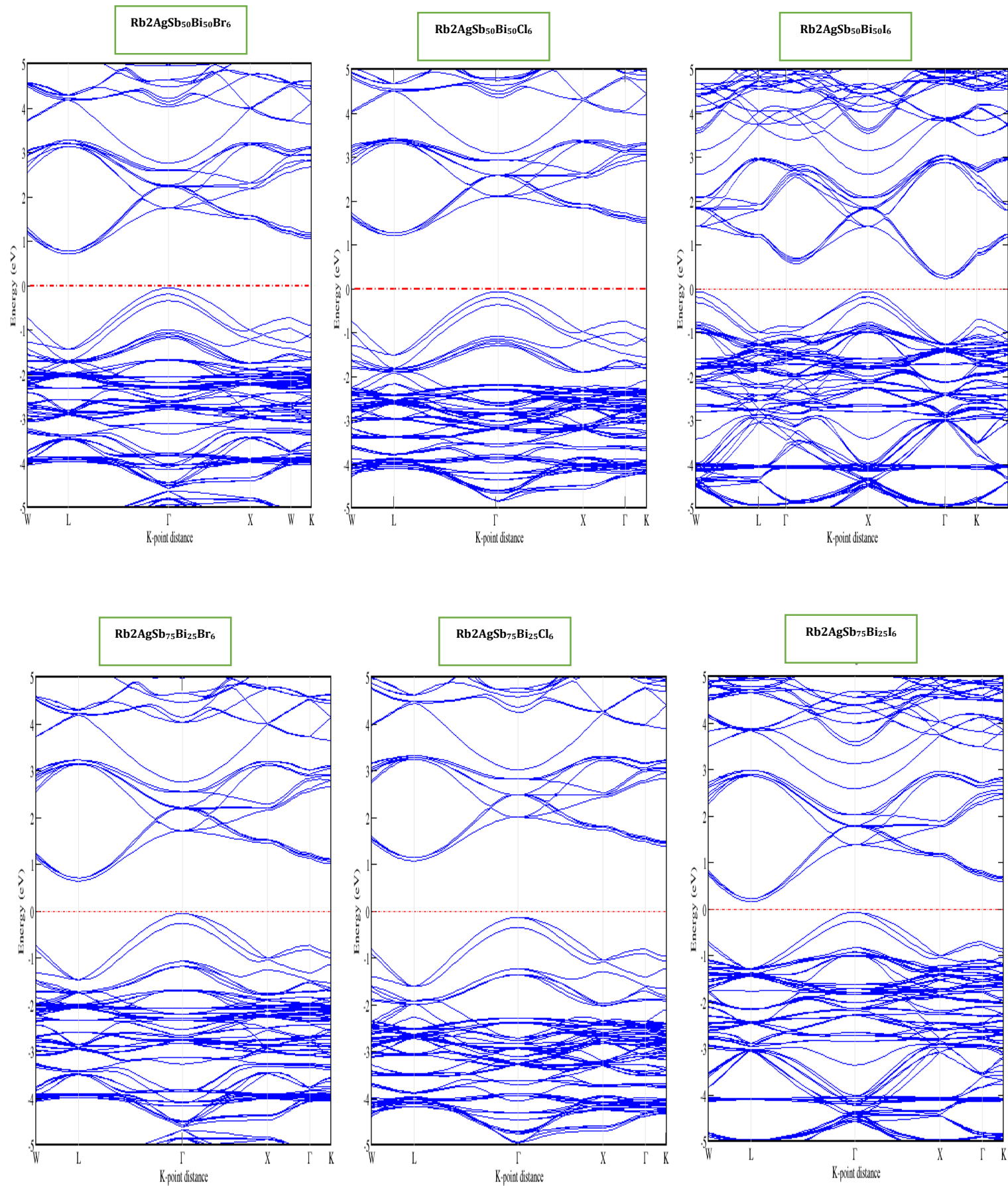
**Chapter VI Theoretical Study of a new Double Perovskite Alloys
Rb₂AgSb_{1-x}Bi_xX' (X' = Cl, Br, I) Using VASP Analysis**

<i>Rb₂AgSb_{1-x}Bi_xX'₆</i>	<i>Br</i>	<i>Cl</i>	<i>I</i>
<i>X = 0</i>	1.32	2.31	1.04
<i>X=0.25</i>	1.39	2.032	0.94
<i>X= 0.5</i>	1.61	2.25	0.82
<i>X= 0.75</i>	1.59	2.27	0.92
<i>X= 1</i>	1.04	2.74	0.76

Table IV.1: Calculated indirect bandgap using HSE (Ev) for Rb₂AgSb_{1-x}Bi_xX'₆ allos



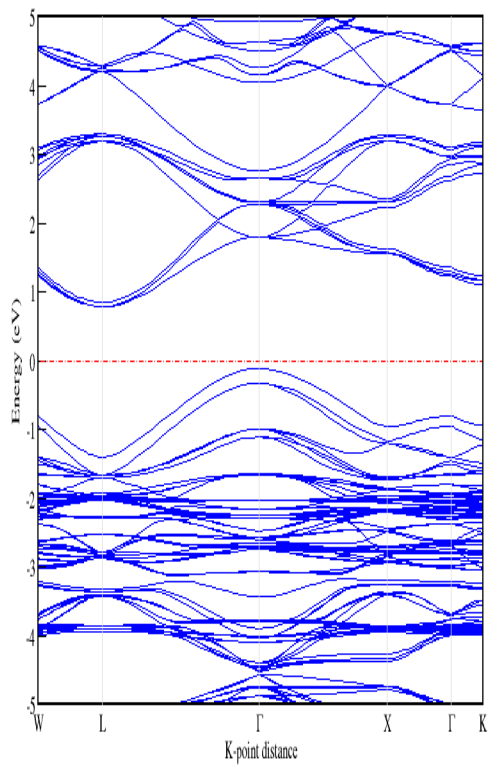
Chapter VI Theoretical Study of a new Double Perovskite Alloys $\text{Rb}_2\text{AgSb}_{1-x}\text{Bi}_x\text{X}'$ ($\text{X}' = \text{Cl}, \text{Br}, \text{I}$) Using VASP Analysis



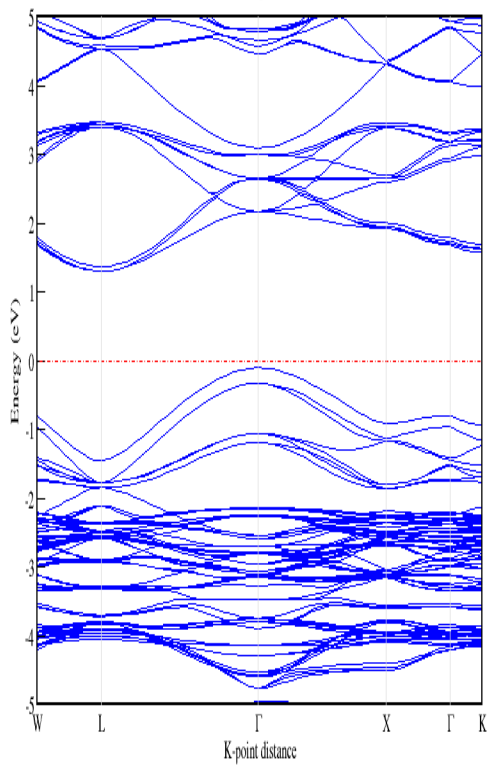
Chapter VI Theoretical Study of a new Double Perovskite Alloys $\text{Rb}_2\text{AgSb}_{1-x}\text{Bi}_x\text{X}'$ ($\text{X}' = \text{Cl}, \text{Br}, \text{I}$) Using VASP Analysis



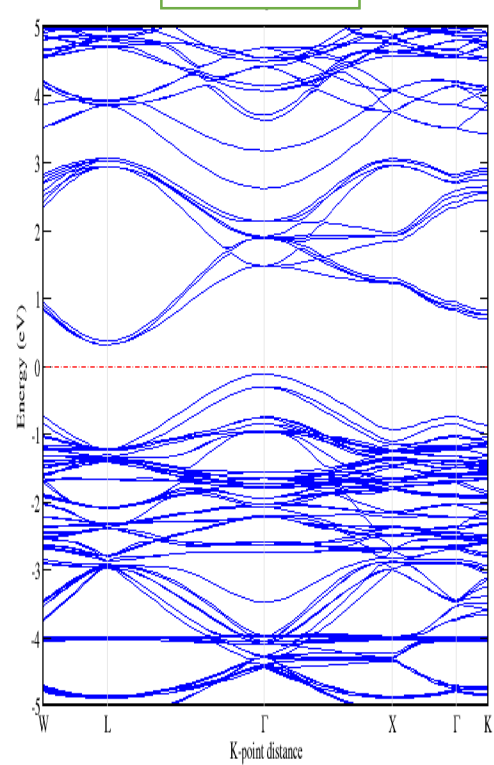
$\text{Rb}_2\text{AgSb}_{25}\text{Bi}_{75}\text{Br}_6$



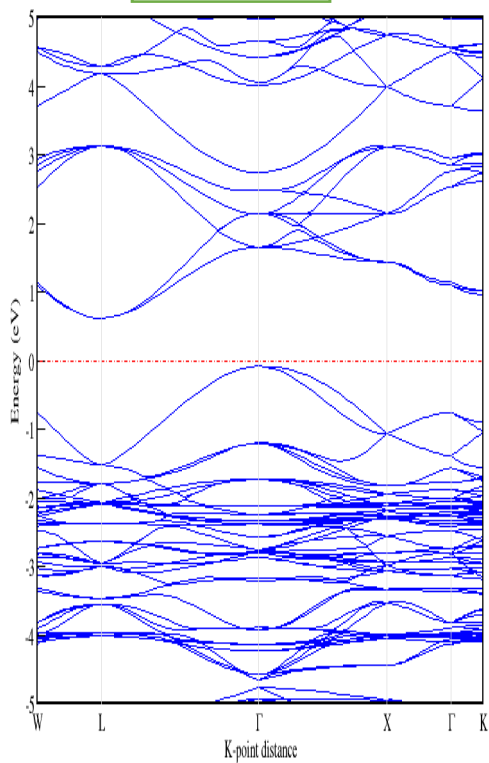
$\text{Rb}_2\text{AgSb}_{25}\text{Bi}_{75}\text{Cl}_6$



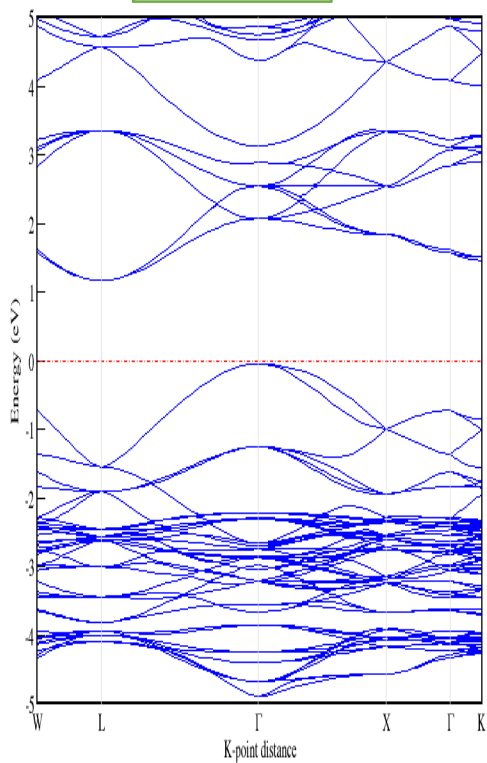
$\text{Rb}_2\text{AgSb}_{25}\text{Bi}_{75}\text{I}_6$



$\text{Rb}_2\text{AgSbBr}_6$



$\text{Rb}_2\text{AgSbCl}_6$



$\text{Rb}_2\text{AgSbI}_6$

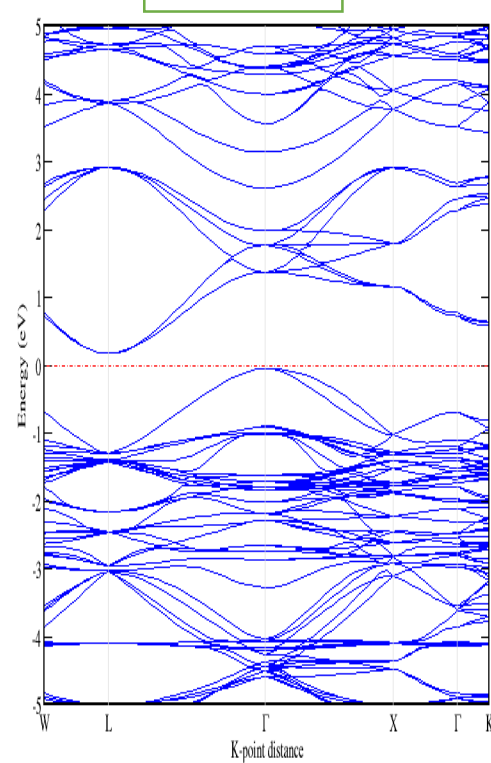


Figure IV.1: The calculated band structure of Rb₂AgSb_{1-x}Bi_xX'₆ alloys.

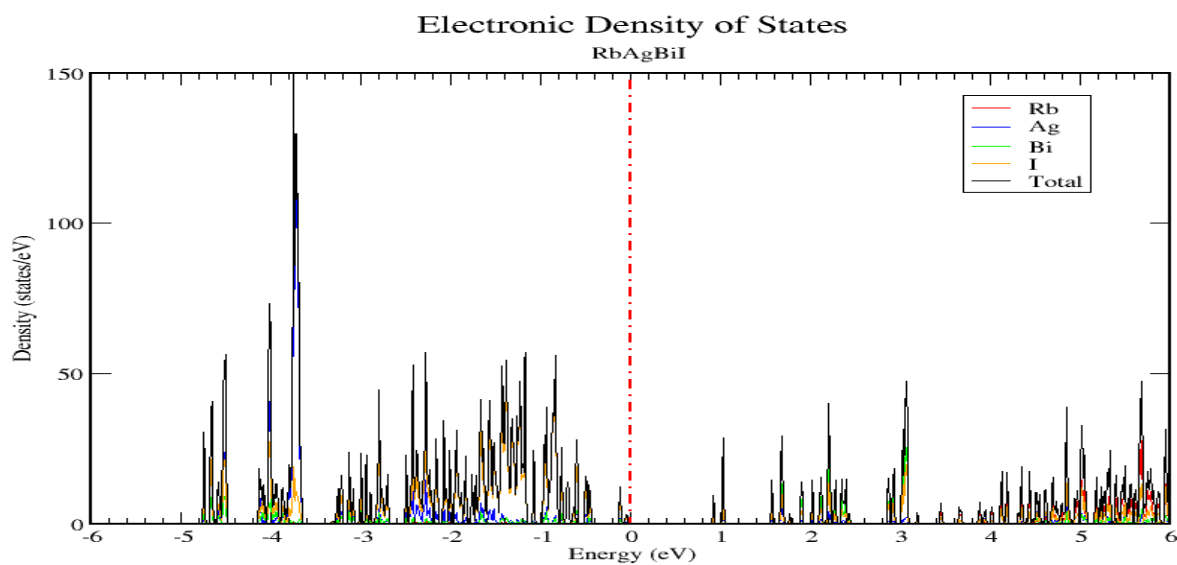
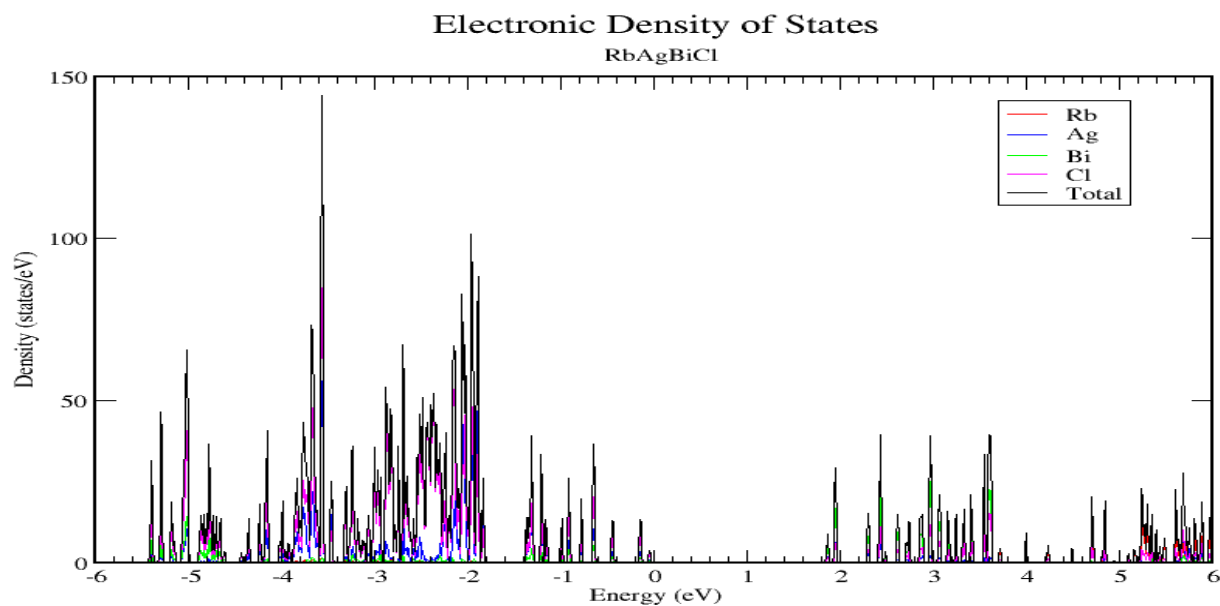
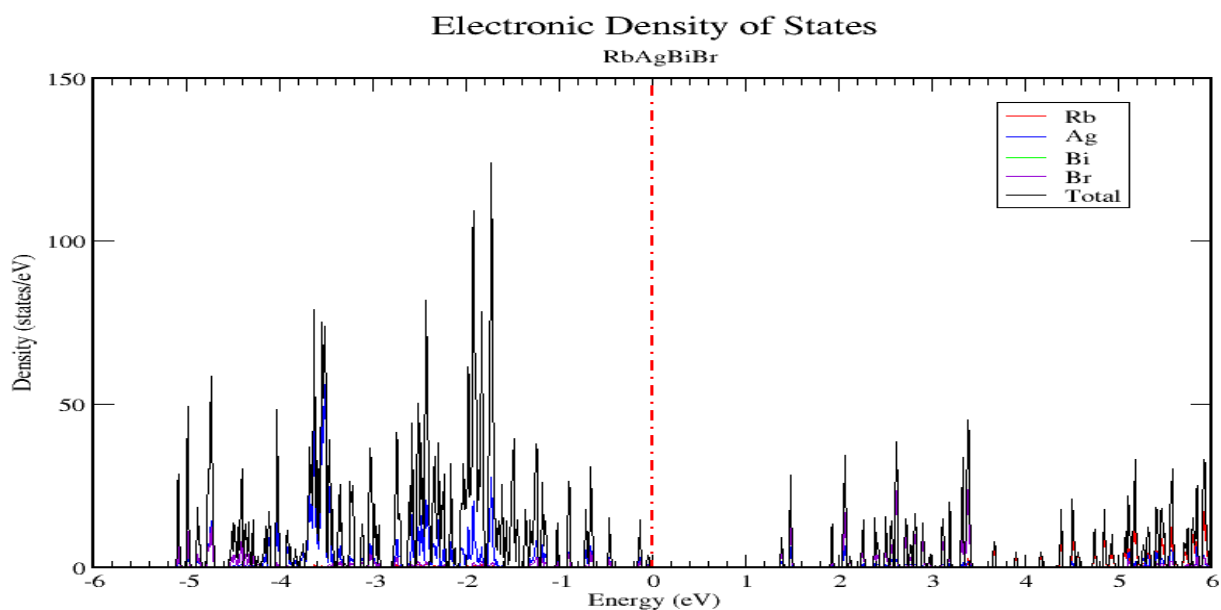
IV.3.1.b Density of states

To gain a deeper understanding of the electronic structure, we analyzed the contribution of each atomic species to a series of bands within the total density of states decomposition. The total and partial atomic densities of states (TDOS and PDOS) for Rb₂AgSb_{1-x}Bi_xX'₆ (where X' = Cl, Br, and I) alloys at various concentrations (x) were computed. The TDOS and PDOS graphs, presented in Fig. IV.11, were plotted using the HSE method.

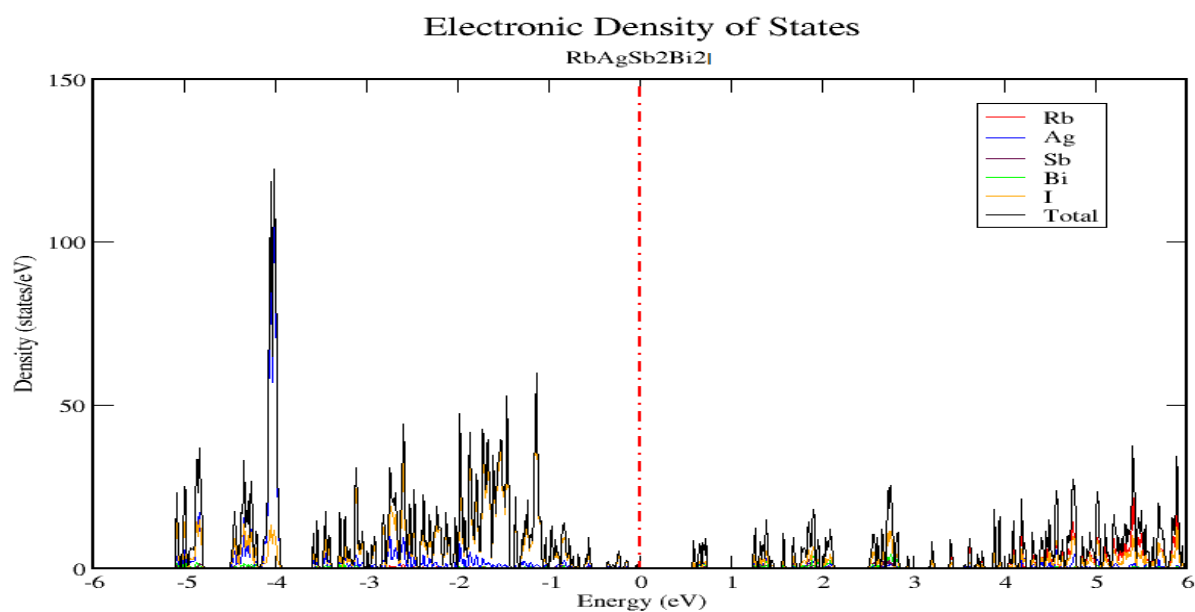
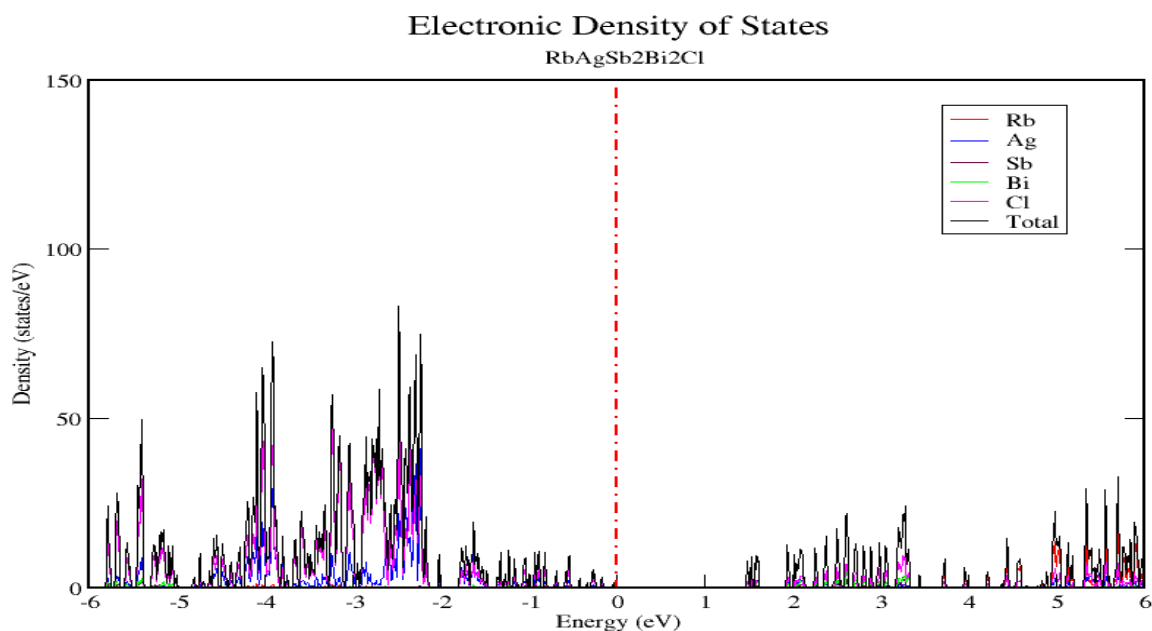
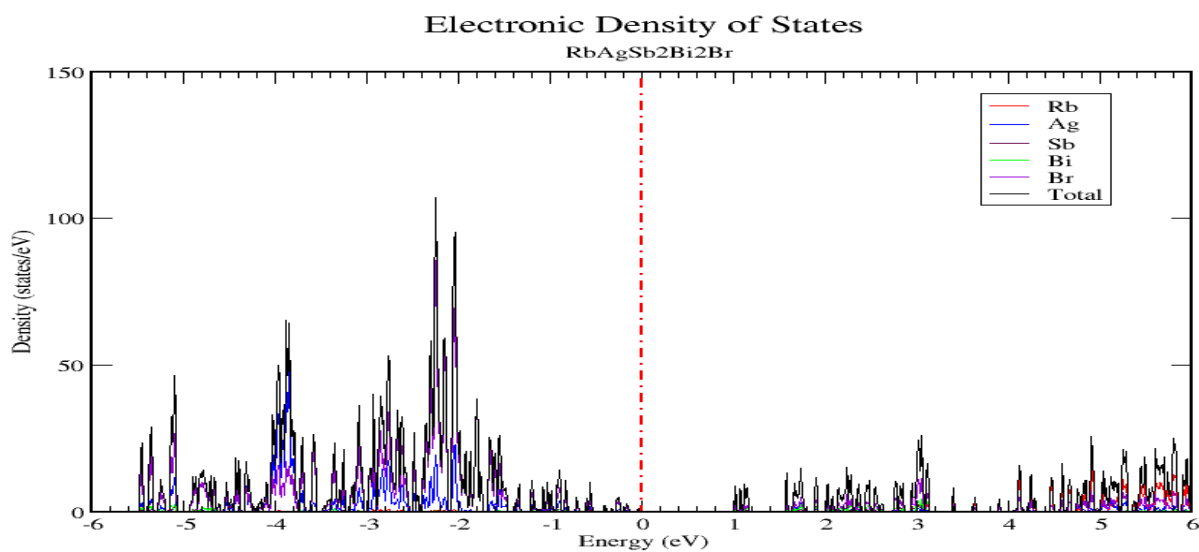
As observed, the low-energy region of the valence band, ranging from -6 eV to -3 eV, primarily arises from a mixture of Sb and Bi states, along with contributions from the Br anion states. The second region, spanning from -3 eV to the Fermi level ($E_x = 0$), is mainly dominated by Ag cationic states hybridized with Cl, Br, and I states, indicating variations in material properties.

The conduction band of Rb₂AgSb_{1-x}Bi_xX'₆ is predominantly composed of Bi states hybridized with different halide anion states. As we move deeper into the conduction band, a significant contribution from Bi states hybridized with other elements becomes evident. Notably, the substitution of Bi atoms at Sb sites has a substantial impact on the conduction band structure. This Bi incorporation leads to the formation of new states in the conduction band minimum, primarily originating from Bi states hybridized with Sb and halide (Br, Cl, and I) states for Rb₂AgSb_{1-x}Bi_xX'₆ alloys (x = 0.25, 0.5, 0.75, and 1), ultimately reducing the band gap value. Consequently, the band gap reduction in Rb₂AgSb_{1-x}Bi_xBr can be attributed to the increase in atomic size from Sb to Bi.

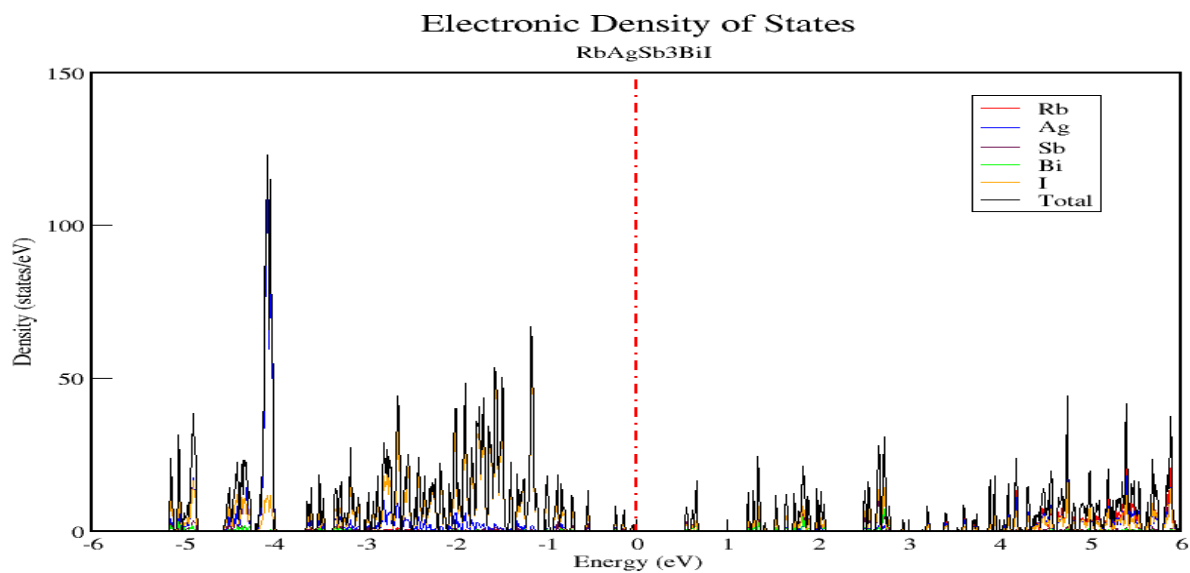
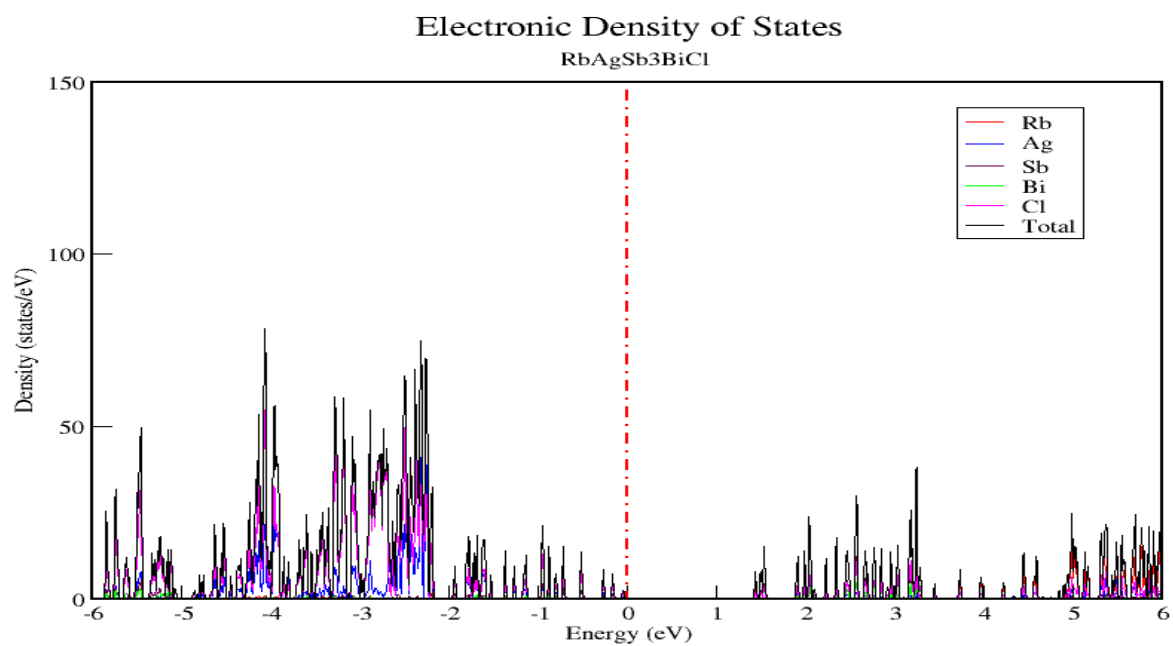
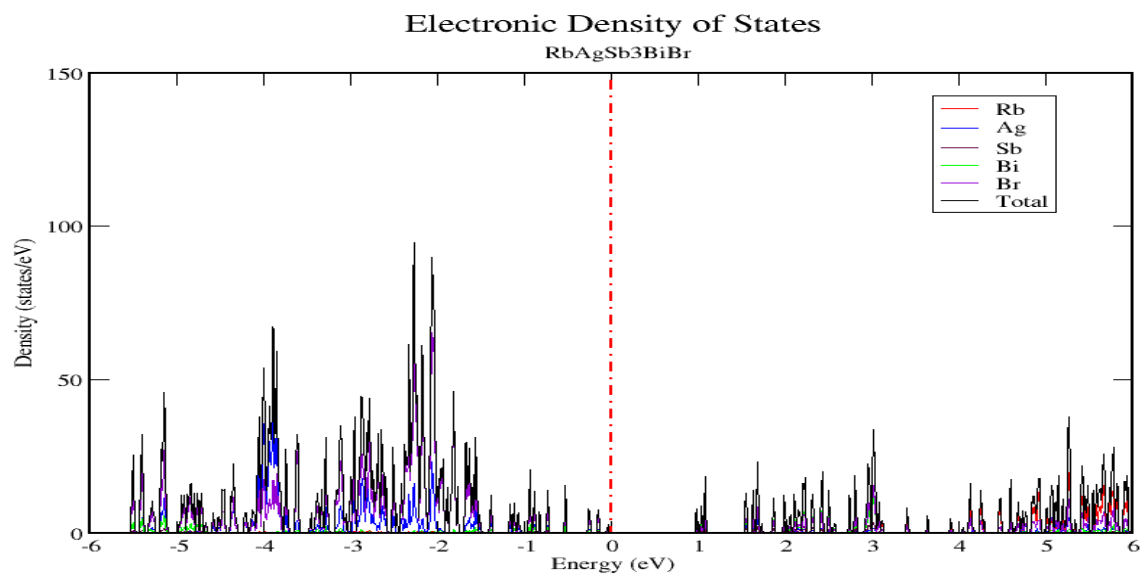
Chapter VI Theoretical Study of a new Double Perovskite Alloys Rb₂AgSb_{1-x}Bi_xX' (X' = Cl, Br, I) Using VASP Analysis



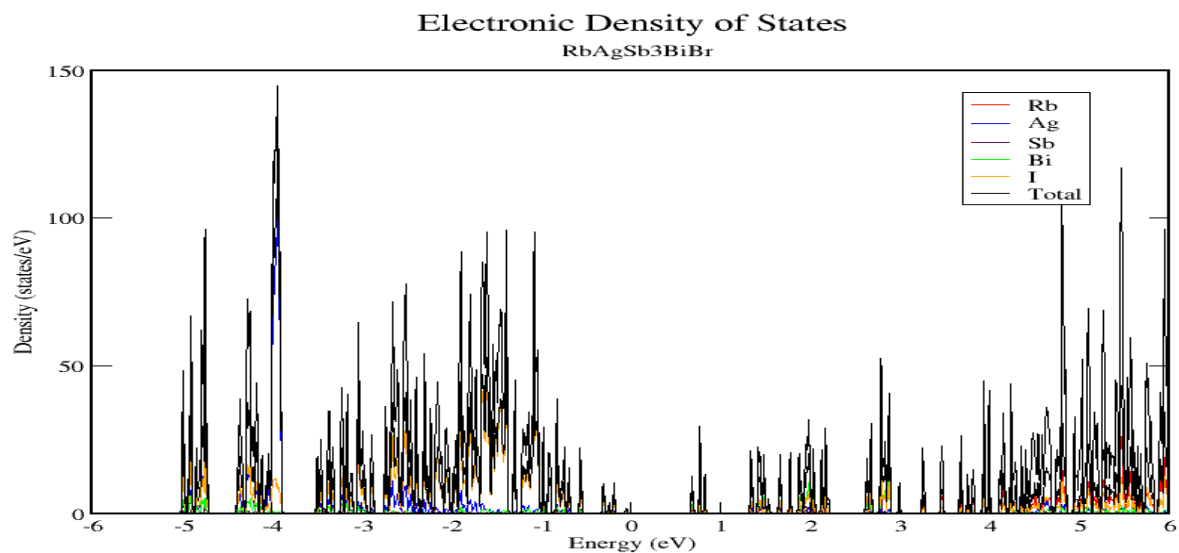
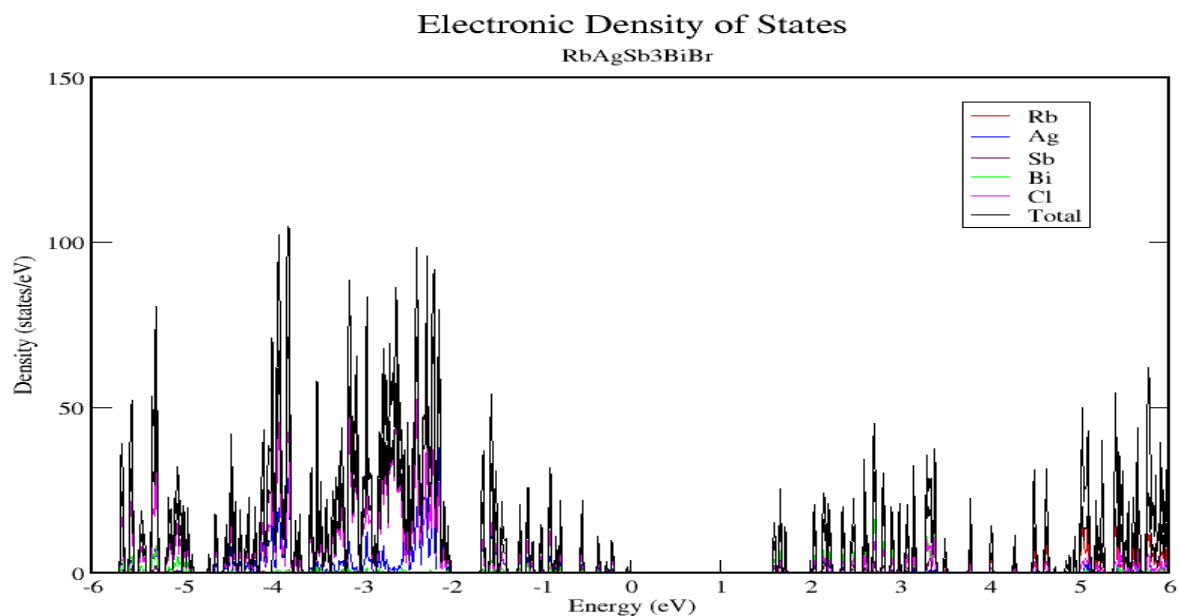
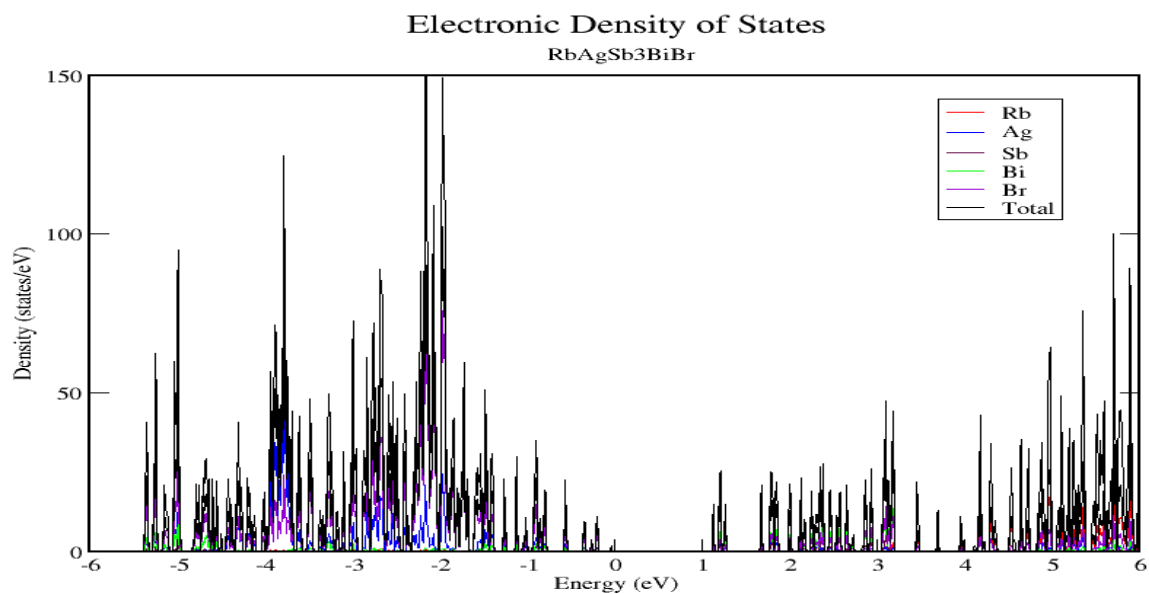
Chapter VI Theoretical Study of a new Double Perovskite Alloys $\text{Rb}_2\text{AgSb}_{1-x}\text{Bi}_x\text{X}'$ ($\text{X}' = \text{Cl}, \text{Br}, \text{I}$) Using VASP Analysis



Chapter VI Theoretical Study of a new Double Perovskite Alloys $\text{Rb}_2\text{AgSb}_{1-x}\text{Bi}_x\text{X}'$ ($\text{X}' = \text{Cl, Br, I}$) Using VASP Analysis



Chapter VI Theoretical Study of a new Double Perovskite Alloys $\text{Rb}_2\text{AgSb}_{1-x}\text{Bi}_x\text{X}'$ ($\text{X}' = \text{Cl, Br, I}$) Using VASP Analysis



Chapter VI Theoretical Study of a new Double Perovskite Alloys
 $\text{Rb}_2\text{AgSb}_{1-x}\text{Bi}_x\text{X}'$ ($\text{X}' = \text{Cl, Br, I}$) Using VASP Analysis

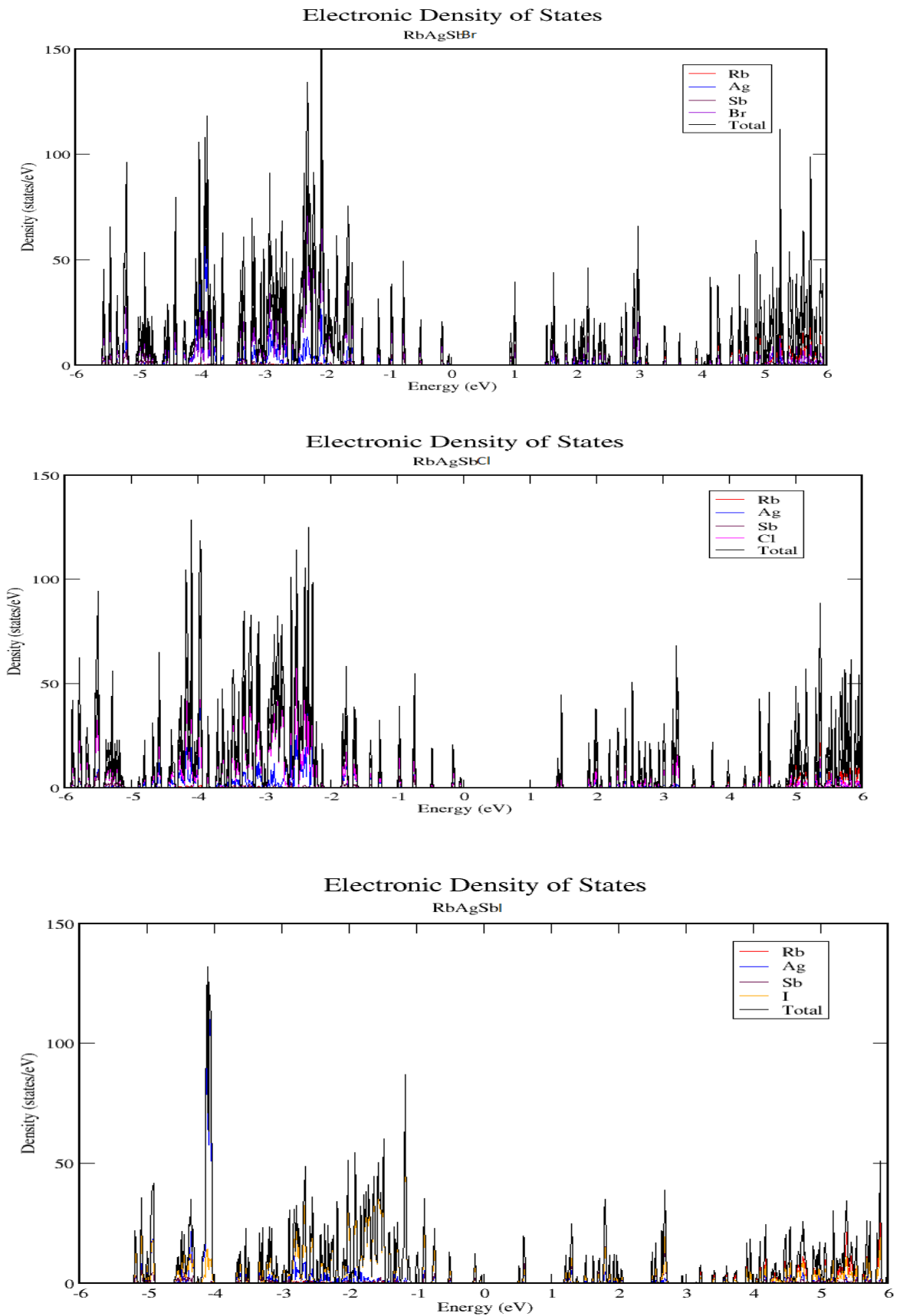


Figure IV.2: Total and partial density of states (DOS) of $\text{Rb}_2\text{AgSb}_{1-x}\text{Bi}_x(\text{X}')_6$ alloys

VI.3.2 Mechanical properties

VI.3.2.1 Elastic coefficients

The elastic properties of a material are crucial as they offer valuable insights into its mechanical and dynamic behavior, crystal anisotropy, and overall rigidity.

The primary goal of our study is to assess the mechanical stability of the compounds examined, primarily relying on the C_{ij} elastic constants. Since all the studied compounds have a cubic structure, they are characterized by three elastic constants: C₁₁, C₁₂, and C₄₄.

The various elastic constants are obtained by applying three deformation matrices (distortions) D_i in response to applied stresses δ along specific spatial directions, allowing for the determination of C₁₁+2C₁₂, C₁₁-C₁₂, and C₄₄, respectively.

All the results are presented in Table (IV.2). It is evident that the studied materials exhibit a significantly higher C₁₁ value compared to C₁₂ and C₄₄, indicating greater resistance to volume change (compression) than to shape change (shear). Born and Huang [7] initially introduced the mechanical stability of the crystalline lattice. In a cubic system, mechanical stability is ensured when the three independent elastic constants satisfy the following Born conditions:

$$C_{11} - C_{12} > 0, C_{11} + 2C_{12} > 0, C_{44} > 0$$

In addition, the compression modulus B must satisfy the criterion:

$$C_{12} < B < C_{11}$$

Table (IV.1) shows that the obtained elastic constant values meet the previously described mechanical stability criteria, confirming that all the compounds examined in this study are mechanically stable.

From the elastic constants C₁₁, C₁₂, and C₄₄ for a cubic system, various mechanical quantities can be evaluated according to the following expressions [7]:

$$G_v = \frac{1}{5}(C_{11} - C_{12} + 3C_{44}) \quad \text{IV.1}$$

$$G_R = \frac{5C_{44}(C_{11}-C_{12})}{4C_{44}+3(C_{11}-C_{12})} \quad \text{IV.2}$$

**Chapter VI Theoretical Study of a new Double Perovskite Alloys
Rb₂AgSb_{1-x}Bi_xX' (X' = Cl, Br, I) Using VASP Analysis**

$$G = \frac{G_V + G_R}{2} \quad \text{IV.3}$$

$$E = \frac{9BG}{3B + G} \quad \text{IV.4}$$

$$\nu = \frac{(3B - 2G)}{2(3B + G)} \quad \text{IV.5}$$

Where G_V is Voigt's shear modulus, G_R is Reuss' shear modulus, E is Young's modulus and ν is Poisson's ratio.

Rb ₂ AgSb _{1-x} Bi _x Br ₆	C ₁₁	C ₁₂	C ₄₄	B	E	a ₀	G	ν	B/G
X= 0	51.780	16.83	7.487	28.35	30.44	11.035	11.53	0.32	2.67
X= 0.25	51.292	16.439	7.025	28.06	29.62	11.063	11.19	0.32	2.51
X= 0.5	50.889	16.227	6.713	27.82	29.20	11.09	11.02	0.33	2.52
X= 0.75	50.596	16.262	6.572	27.72	28.70	11.116	10.81	0.33	2.56
X=1	49.654	16.346	6.24	27.45	27.74	5.571	10.42	0.33	2.63

Rb ₂ AgSb _{1-x} Bi _x Cl ₆	C ₁₁	C ₁₂	C ₄₄	B	E	a ₀	G	ν	B/G
X= 0	52.871	20.129	6.865	31.04	29.71	5.264	10.67	0.35	2.91
X= 0.25	54.485	19.012	6.941	30.84	30.11	10.55	11.26	0.34	2.74
X= 0.5	54.169	18.627	6.935	30.55	30	10.583	11.22	0.34	2.72
X= 0.75	53.598	18.761	6.520	30.37	29.16	10.60	10.88	0.34	2.79
X=1	53.713	18.490	6.821	30.23	29.76	10.634	11.14	0.34	2.71

$\text{Rb}_2\text{AgSb}_{1-x}\text{Bi}_x\text{I}_6$	C_{11}	C_{12}	C_{44}	B	E	a_0	G	ν	B/G
X= 0	44.539	14.505	7.731	24.523	27.90	11.767	10.64	0.31	2.42
X= 0.25	44.016	23.554	7.381	26.28	21.56	11.79	7.91	0.36	3.23
X= 0.5	43.486	14.325	7.215	24.03	26.80	11.828	10.20	0.31	2.36
X= 0.75	43.295	14.117	6.906	23.84	26.27	11.855	9.98	0.32	2.55
X=1	42.809	14.126	6.606	23.69	25.60	11.883	9.70	0.32	2.44

Table IV.2: The calculated compressibility modulus (B) and elastic constants (C_{ij}) in GPa, along with the lattice parameter (a_0) in Å, Young's modulus (E) in GPa, shear modulus (G) in GPa, Poisson's ratio (ν), and the B/G ratio.

To predict the brittle or ductile behavior of materials, S. F. Pugh [8] introduced the ratio between the bulk modulus (B) and the shear modulus (G), denoted as B/G . Here, G represents resistance to plastic deformation, while B indicates resistance to fracture. The critical threshold distinguishing ductile from brittle materials is approximately 1.75, with materials being brittle for $B/G < 1.75$ and ductile for $B/G > 1.75$. According to Table (IV.2), the calculated B/G values classify all the studied materials as ductile.

Another criterion for distinguishing between ductile and brittle materials is Poisson's ratio (ν), where the critical value is approximately 0.33. A material is considered brittle if ν is less than 0.33, whereas it behaves ductilely when ν is greater than 0.33. Based on the values in Table (IV.2), Poisson's ratio (ν) is equal to or greater than 0.33 for all the materials, confirming their ductile nature.

Young's modulus (E) serves as a reliable indicator of a material's hardness. A higher E value corresponds to greater stiffness. Based on the obtained E results, we can conclude that the materials are hard.

Reference

- [1] Zhao, C., Cheung, C. F., & Xu, P. (2020). High-efficiency sub-microscale uncertainty measurement method using pattern recognition. *ISA Transactions*, 101, 503–514. <https://doi.org/10.1016/j.isatra.2020.02.005>
- [2] Zhu, X., Liu, Z., Chen, H., Wang, X., Wang, W., & Lu, Y. (2021). Templateless, plating-free fabrication of flexible transparent electrodes with embedded silver mesh by electric-field-driven microscale 3D printing and hybrid hot embossing. *Advanced Materials*, 33(21), 2007772. <https://doi.org/10.1002/adma.202007772>
- [3] Kresse, G., & Furthmüller, J. (1996). Efficiency of ab-initio total energy calculations for metals and semiconductors using a plane-wave basis set. *Computational Materials Science*, 6(1), 15–50. [https://doi.org/10.1016/0927-0256\(96\)00008-0](https://doi.org/10.1016/0927-0256(96)00008-0)
- [4] Perdew, J. P., Burke, K., & Ernzerhof, M. (1996). Generalized gradient approximation made simple. *Physical Review Letters*, 77(18), 3865–3868. <https://doi.org/10.1103/PhysRevLett.77.3865>
- [5] Heyd, J., Scuseria, G. E., & Ernzerhof, M. (2003). Hybrid functionals based on a screened Coulomb potential. *The Journal of Chemical Physics*, 118(18), 8207–8215. <https://doi.org/10.1063/1.1564060>
- [6] Chen, X., Jiang, Z., Deng, W., Gu, Y., & Chen, W. (2020). Bayesian optimization based on a unified figure of merit for accelerated materials screening: A case study of halide perovskites. *Science China Materials*, 63, 1024–1035. <https://doi.org/10.1007/s40843-020-1311-4>
- [7] Reuss, A. (1929). Berechnung der Fließgrenze von Mischkristallen auf Grund der Plastizitätsbedingung für Einkristalle. *Zeitschrift für Angewandte Mathematik und Mechanik*, 9(1), 49–58. <https://doi.org/10.1002/zamm.19290090104>
- [8] Pugh, S. F. (1954). XCII. Relations between the elastic moduli and the plastic properties of polycrystalline pure metals. *The London, Edinburgh, and Dublin Philosophical Magazine and Journal of Science*, 45(367), 823–843. <https://doi.org/10.1080/14786440808520496>

General conclusion

In this thesis, we looked at structural properties such as stability, lattice constant, interatomic distance, and total equilibrium energy; electronic properties such as band structure and density of states of $\text{Rb}_2\text{AgSbCl}_6$ materials in their pure state as well as after substituting Bromine for chloride. First, optical properties including absorption, refraction, extinction, reflectivity coefficients, and the dielectric function were calculated and analyzed. Additionally, the carrier effective mass, mobility, and SLME were investigated to assess the potential of these materials for use in solar cells. We performed all calculations using Density Functional Theory (DFT). The study utilized plane waves combined with a full potential (FP-APW) approach, while exchange and correlation effects were addressed using two approximations: the Wu-Cohen Generalized Gradient Approximation (WC-GGA) and the GGA-TB-mBJ method of Tran and Blaha, modified by Becke and Johnson. This framework was applied to investigate the $\text{Rb}_2\text{AgSb}(\text{Cl}_{1-x}\text{Br}_x)_6$ alloys.

From the total energy versus volume calculations, we determined that the optimized mesh parameters align well with the theoretical data for the pure material. The investigation of electronic properties revealed that $\text{Rb}_2\text{AgSbCl}_6$ is a semiconductor with an indirect band gap of approximately 2.08 eV, consistent with theoretical predictions. On the other hand, we sought to address the question: how will Br substitution affect these properties?

By reviewing the obtained results, one can observe that mesh parameters increase when Br atoms are gradually substituted into Cl atoms in the $\text{Rb}_2\text{AgSbCl}_6$ unit cell. We also remarked that when the Cl atom is substituted by the Br atom, the nature of the band gap and the semiconducting character is retained; however, the energy band gap value is linearly reduced from $x=0$ to $x=1$ for $\text{Rb}_2\text{AgSb}(\text{Cl}_{1-x}\text{Br}_x)_6$ alloys. The calculation of the density of states allowed us to give a detailed explanation of the contribution of the different orbitals.

Regarding the optical properties, our findings indicate that both the real and imaginary spectra exhibit significant anisotropy across all alloys. Analysis of the

absorption coefficient spectra for $\text{Rb}_2\text{AgSb}(\text{Cl}_{1-x}\text{Br}_x)_6$ alloys reveals that Br substitution notably reduces the transparent region while enhancing absorption in the visible spectrum. Additionally, we calculated the Spectroscopic Limited Maximum Efficiency (SLME). The luminescent minority carrier efficiency (SLME) of $\text{Rb}_2\text{AgSb}(\text{Cl}_{0.5}\text{Br}_{0.5})_6$ was found to be 9.51%. While this value is relatively modest, it can be attributed to the material's indirect band gap. This suggests that these alloys possess high sunlight absorption in the visible range, making them promising candidates for use as efficient solar absorbers.

The thermoelectric (TE) properties of $\text{Rb}_2\text{AgSb}(\text{Cl}_{1-x}\text{Br}_x)_6$ alloys are investigated in detail by combining Boltzmann transport theory with first-principles band structure calculations. The maximum ZT value of 0.77 is observed for the pure compound ($x = 0$) at $T = 700$ K, primarily due to the combination of reduced thermal conductivity and a high power factor. This composition exhibits the best thermoelectric performance, with the highest and most stable ZT. However, substituting Br for Cl generally leads to a reduction in ZT, although the material retains its thermoelectric behavior.

In this study, we focus on the electronic properties of $\text{Rb}_2\text{AgSb}_{1-x}\text{Bi}_x\text{X}'_6$ alloys, where x takes values of zero, 0.25, 0.50, 0.75, and 1, with X' representing Cl, Br, or I. These compounds demonstrate highly adjustable features in both their crystal structure and electrical properties, making them attractive for diverse applications.

We also examined the differences between VASP and WIEN2k calculations, particularly in the context of $\text{Rb}_2\text{AgSbCl}_6$.

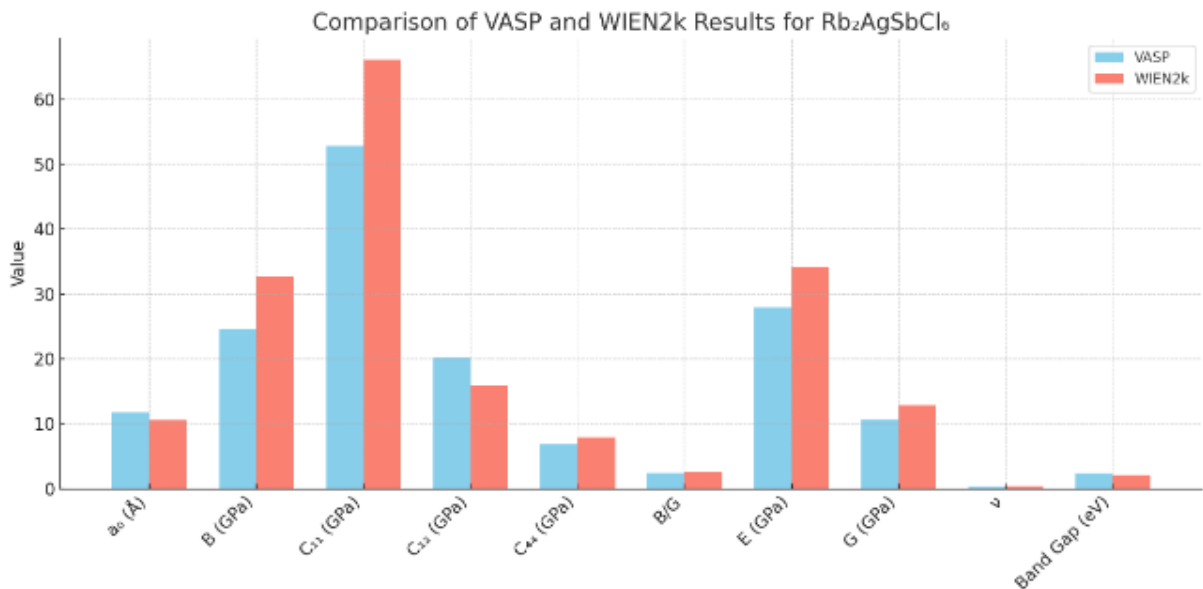
Annex

1. Difference between VASP and WIEN2k calculations

$Rb_2AgSbCl_6$	VASP	WIEN2k
a_0	11.76	10.56
B	24.52	32.74
C_{11}	52.87	66.13
C_{12}	20.129	15.91
C_{44}	6.865	7.92
B/G	2.42	2.55
E	27.90	34.11
G	10.64	12.86
ν	0.31	0.33
Gap	2.31 eV	2.08 eV

Table 1: comparing vasp and wien2k calculated compressibility modulus (B) and elastic constants (C_{ij}) in GPa, along with the lattice parameter (a_0) in Å, Young's modulus (E) in GPa, shear modulus (G) in GPa, Poisson's ratio (ν), and the B/G ratio and gap for $Rb_2AgSbCl_6$.

- ✚ VASP tends to predict a more relaxed (larger volume) structure, and slightly softer mechanical properties.
- ✚ WIEN2k predicts a denser, stiffer material with slightly lower band gap
- ✚ These differences arise from:
 - All-electron treatment in WIEN2k (more accurate near nuclei).
 - Pseudopotential approximations in VASP (efficient but sometimes slightly less precise).



Annex

Here is the comparison focused on mechanical properties of $\text{Rb}_2\text{AgSbCl}_6$ using VASP and WIEN2k. You can see that WIEN2k generally predicts higher stiffness (bulk, Young's, and shear moduli) than VASP, while both methods agree on ductile behavior ($B/G > 1.75$) and similar Poisson's ratio.

2- Conclusion

Both VASP and WIEN2k give physically consistent results.

- Use VASP if you're aiming for larger systems, high-throughput studies, or integration with phonon/optical tools.
- Use WIEN2k if you need precise electronic structure or are working with **core-** level or strongly correlated effects.